

INTERMEDIATE-RANGE ORDERING  
AND TOPOCHEMICAL HETEROGENEITY IN  
BINARY AND TERNARY SILICATE GLASSES



**FRIEDRICH-SCHILLER-  
UNIVERSITÄT  
JENA**

**Dissertation**

Zur Erlangung des akademischen Grades doctor rerum naturalium  
(Dr. rer. nat)

vorgelegt dem Rat der Chemisch-Geowissenschaftlichen Fakultät der  
Friedrich-Schiller-Universität Jena

von M. Sc. Mariana Fatobene Ando

geboren am 09.08.1984 in Santo André, Brasilien

Gutachter:

1. Prof. Dr. Lothar Wondraczek, Friedrich-Schiller Universität Jena
2. Prof. Dr. Falko Langenhorst, Friedrich-Schiller Universität Jena

Tag der Verteidigung: 13.05.2020

# Abstract

The fact that glasses can be synthetically produced and engineered allows plenty of opportunity to control their structure. Even though it may sound simple, the glass formation is controlled by physical-chemical principles and any change in the composition, temperature, cooling rate, processing type, etc. impacts the final material - and consequently its properties.

While glasses are considered non-crystalline solids due to the absence of long-range periodicity, they show a regular construction, defined by the short-range and intermediate-range order. Their characteristics are described by the topology, which denotes the basic geometrical arrangement of the structural units and allocation of the atoms. At macroscale, for a glass of the same composition, the structure and properties reveal to be homogeneous, independently of the processing, temperature or precursor material. However, at microscale, the same glass may show a different picture, revealing a topological heterogeneity of a few nanometers.

Due to technological limitations, the main difficulty is to directly access this region. There is a consensus that the topological heterogeneity, however, manifests as a significant peak at very low temperatures (about 5 K) or low-frequencies (about 1 THz or  $33\text{ cm}^{-1}$ ) by collective vibrational modes. Since the main model for estimating the phonon contribution to the specific heat in a crystal, the Debye model, does not predict any peak at low temperature and there are no models to describe these manifestations in vitreous materials, usually it is considered an anomaly. This anomalous peak has been called *Boson peak*. Even though it remains as one of the major debated and unsolved problems of condensed-matter physics, intense investigations in these almost 50 years brought an enormous knowledge about most of its characteristics.

In order to access the intermediate-range order and the topochemical heterogeneity of selected binary and ternary glass network formers made by reactive powder sintering process, investigations of the vibrational density of states in the region of the Boson peak has been conducted. Foremost, this study describes that the feature of the Boson peak is governed by topological heterogeneity as well as topochemical heterogeneity. Together with other characterization methods, this has been shown

as a powerful descriptive route to understand glass functionality and glass structure in a more extended perspective. Even though it is important for the wide relevance of fundamental knowledge of glasses, this is notably important for high-technological glasses and in which bottom-up strategies are necessary to design new glass compositions with straightforward applications.

# Kurzzusammenfassung

Die Tatsache, dass Gläser synthetisch hergestellt und angepasst werden können erlaubt enorme Möglichkeiten ihre Struktur zu beeinflussen. Wenngleich dies einfach klingen mag, so ist die Glasformung doch durch physikalisch-chemische Prinzipien bestimmt und jedwede Änderung hinsichtlich Zusammensetzung, Temperatur, Abkühlrate, Prozessierung etc. wirkt sich auf das endgültige Material und auf dessen Eigenschaften aus.

Obwohl Gläser aufgrund der fehlenden großreichweitigen Periodizität als nicht-kristalline Festkörper betrachtet werden, zeigen sie einen regelmäßigen Aufbau, welcher durch Nah- und mittelreichweitige Ordnung. Ihre Eigenschaften werden durch ihre Topologie beschrieben, welche die grundlegende geometrische Anordnung der strukturellen Einheiten und die Zuordnung der Atome kennzeichnet. Auf einer makroskopischen Skala können Struktur und Eigenschaften eines Glases als homogen erscheinen. Ein Glas derselben Zusammensetzung kann auf einer mikroskopischen Skala ein unterschiedliches Bild mit einer topologischen Heterogenität von einigen Nanometern zeigen.

Aufgrund technologischer Grenzen besteht die größte Herausforderung in der direkten Zugänglichkeit dieser Region. Es besteht jedoch ein Konsens, dass sich die topologische Heterogenität in Form eines signifikanten Peaks bei sehr niedrigen Temperaturen (ungefähr 5 K) beziehungsweise bei niedrigen Frequenzen (circa 1 THz) aufgrund kollektiver Vibrationsmoden manifestiert. Da das übliche Modell zur Abschätzung des Phononenbeitrags zur spezifischen Wärmekapazität in einem Kristall, das Debye-Modell, keinerlei Peak bei niedrigen Temperaturen vorhersagt und keine weiteren Modelle existieren welche einen solchen Effekt in Glasmaterialien vorherzusagen, wird er als Anomalie bezeichnet. Diese Anomalie wird als Boson-Peak bezeichnet. Wenngleich er noch immer zu den am meist diskutierten und ungelösten Problemen der Physik der kondensierten Materie zählt, so haben intensive Untersuchungen in den vergangenen 50 Jahren ein enormes Wissen über die meisten seine Eigenschaften errungen.

Um die einen Zugang zur mittelreichweitigen Ordnung und die topochemische Heterogenität ausgewählter binärer und tertiärer Glas-Netzwerkbildner, welche mittels

des reaktivem Pulversinterprozesses hergestellt wurden, zu erhalten, wurden Untersuchungen der Vibrations-Zustandsdichten im Bereich des Boson-Peaks durchgeführt. In erster Linie beschreibt diese Arbeit, dass der Effekt des Boson-Peaks im Wesentlichen durch topologische und topochemische Heterogenität bestimmt wird. Zusammen mit anderen Charakterisierungsmethoden hat sich dies als ein sehr mächtiger Weg zu einem erweiterten Verständnis der Glasfunktionalität und Glasstruktur herausgestellt. Wenngleich es wichtig für das grundlegende Wissen über Gläser ist, so ist es von besonderer Bedeutung für hochtechnologische Gläser bei denen bottom-up Strategien für das anwendungsorientierte Design neuer Glaszusammensetzungen notwendig sind.

# Acknowledgments

I would like to thank Prof. Wondraczek for providing such interesting and challenging topic and for his supporting during this work and opportunities regarding collaborations, equipment and research.

For all the friendship, help and scientific discussions provided by the colleges at the Otto-Schott-Institute, my many thanks to Bruno, Guilherme, Benjamin, Aaron, Dominik, Kristin, Ali, Lenka, Theresia, Huyen, Courtney, Garth, Caio, Doris, Vivi, Yuko, Felix, Byoungjin, Lingqi, Pauline, Annika, Rocío, Yang, Xu, Ru, Jan, Gohar, Elham, Atef, Ding, Pigter, Roman, Omar, Jelena, Vahid, Ayda, Aziz, Gabriel, René, Thien, Robert, Tom, Chia-En, Arnulf, Karsten and Michal. I particularly would like to thank Sindy and Peter for all support, kindness and time for discussions, Shigeki for sharing a sample with me and Ferdinand for german translations. It has been a pleasure working with a multicultural group, surely it made the daily work much more interesting. My sincerely thanks to the kindest secretary Ute Böttger, and technicians Christian Zeidler, Gabriele Möller, Nadja Büchert, Thomas Kittel and Claudia Siedler, for their patience and stunning work.

I would also like to state my appreciation to the external collaborators at the Leibniz-Institute of Photonic Technology (IPHT), Prof. Hartmut Bartelt, Katrin Wondraczek, Kay Schuster and all involved in the optical fiber technology group for providing the samples, access to the laboratories and discussions. I am also thankful to Jan Dellith and Andy Scheffel for WD-EPMA measurements. To my friends that have been for a short time at IPHT, Romain and Ricardo my most honest thanks.

Still from external collaboration, I would like to thank Jean-Luc Garden and Pierre Lachkar for low-temperature heat capacity measurements and hospitality at Institute Neél in Grenoble, Prof. Stefan Ebbinghaus from Martin Luther University Halle-Wittenberg for low-temperature heat capacity measurements, Prof. Dominique de Ligny and Alexander Veber from Institute of glass and ceramics in Erlangen for Brillouin scattering measurements, Prof. Falko Langenhorst from Institute of earth sciences in Jena for transmission electron microscopy, Tatsuya Mori from University of Tsukuba for THz-time domain spectroscopy measurements and Maximilian Heck and Prof. Stefan Nolte from Institute of Applied physics (IAP) for providing the fs-laser glass modifications.

Finally, my enormous thank you to my family and friends. I am specially grateful to Ron Fatobene Ando for helping me with computational skills by treating the fluorescence background in Chap. 4.3, by help with some figures and by german translations.

# Contents

<b>Abstract</b>	<b>i</b>
<b>Kurzzusammenfassung</b>	<b>iii</b>
<b>Acknowledgments</b>	<b>v</b>
<b>List of abbreviations and symbols</b>	<b>viii</b>
<b>List of figures and tables</b>	<b>xv</b>
<b>1 Introduction</b>	<b>1</b>
<b>2 Theoretical background</b>	<b>4</b>
2.1 The nature of glass formation process . . . . .	4
2.2 Cooperative relaxations and the entropy . . . . .	5
2.3 Potential energy landscape . . . . .	6
2.4 The physics of vibrations . . . . .	8
2.4.1 Debye model . . . . .	11
2.4.2 Debye anomalies in glasses . . . . .	13
2.5 Structure of silica, vitreous boric oxide and silicate glasses . . . . .	14
2.5.1 Silica glass . . . . .	14
2.5.2 Vitreous boric oxide . . . . .	20
2.5.3 Binary aluminosilicate glasses . . . . .	22
2.5.4 Binary borosilicate glasses . . . . .	25
<b>3 Experimental</b>	<b>27</b>
3.1 Powder sintering technology . . . . .	27
3.2 Low-temperature heat capacity . . . . .	28
3.3 Vibrational spectroscopy . . . . .	30
3.4 Terahertz time-domain spectroscopy . . . . .	32
3.5 UV-Vis spectroscopy . . . . .	33
3.6 Photoluminescence spectroscopy . . . . .	34
3.7 Impedance spectroscopy . . . . .	35



3.8	Polarization microscopy . . . . .	36
3.9	Refractive index . . . . .	37
3.10	Femtosecond-induced structural modification in glass . . . . .	38
3.11	Brillouin scattering . . . . .	39
3.12	Mechanical properties . . . . .	40
<b>4</b>	<b>Results and discussion</b>	<b>42</b>
4.1	Binary aluminosilicate glasses . . . . .	42
4.2	Ternary aluminoborosilicate glasses . . . . .	53
4.3	Topological modifications of silica glass by femtosecond laser exposure	75
<b>5</b>	<b>Summary</b>	<b>93</b>
<b>6</b>	<b>Zusammenfassung</b>	<b>98</b>
<b>7</b>	<b>Bibliography</b>	<b>103</b>
	<b>Selbstständigkeitserklärung</b>	<b>132</b>
	<b>Curriculum Vitae</b>	<b>133</b>

# List of abbreviations and symbols

## Abbreviations

NMR	Nuclear Magnetic Resonance
Bp	Boson peak
UV	Ultra-Violet
VDOS	Vibrational Density of States
MCT	Mode Coupling Theory
CRN	Continuous Random Network
SRO	Short-Range Order
IRO	Intermediate-Range Order
REPUSIL	Reactive Powder Sintering Process
CPA	Coherent-Potential Approximation
IR	Infra-Red
THz -TDS	THz - Time Domain Spectroscopy
FIR	Far-Infrared
AC	Alternating Current
fs	Femto-second
EXAFS	Extended X-ray absorption fine structure
TEM	Transmission Electron Microscopy
FTIR	Fourier-Transform Infra-Red
CT	Charge Transfer
RE	Rare Earth
WD-EPMA	Wavelength Dispersive - Electron Probe Micro-analysis
OHC	Oxygen Hole Center
FWHM	Full-Width at Half-Maximum
EMSC	Extended Multiplicative Signal Correction
DAC	Diamond Anvil Cell
NBOHC	Nonbridging Oxygen Hole Center
HT-HP	High-Temperature - High-Pressure

## Symbols

$\lambda$	Wavelength
$C_P$	Heat capacity
$g(\omega)$	Density of states
$T_g$	Transition glass temperature
$\tau$	Relaxation time
$\eta$	Viscosity
$G$	Shear modulus
$k_B$	Boltzmann constant
$T$	Temperature
$\vec{k}$	wave-vector
$\omega$	Frequency
$\hbar$	Reduced Planck
$n(\omega)$	Bose-Einstein distribution function
$\nu_p$	Phase velocity
$\nu_L$	Longitudinal sound velocity
$\nu_T$	Transversal sound velocity
$\nu_D$	Debye sound velocity
$V$	Volume
$N_{st}$	Number of states inside a given volume
$\omega_D$	Debye cutoff frequency
$\vec{k}_D$	Debye cutoff wave-vector
$C_V$	Heat capacity at constant volume
$\theta_D$	Debye temperature
$D1$	Defect 1
$D2$	Defect 2
$E$	Elastic modulus
$N_A$	Avogadro constant
$C(\omega)$	Coupling coefficient
$\alpha(\nu)$	Absorption coefficient
$Z(\omega)$	Impedance

$Z'$	Real part of $Z(\omega)$
$Z''$	Imaginary part of $Z(\omega)$
$\rho_r$	Resistivity
$\sigma$	Conductivity
$E_A$	Activation energy
$n$	refractive index
NA	Numerical aperture
$K$	Bulk modulus
$E$	Elastic modulus
$\nu$	Poisson's ratio
$L$	Longitudinal modulus
$\rho$	Mass density
$V_f$	Free volume
$r_a$	radii of the cation
$r_b$	radii of the ion
$H_V$	Vickers hardness
$\xi$	Size of the heterogeneity
$\omega_{Bp}$	Boson peak frequency
S	Shape factor
$g_D(\omega)$	Debye density of states
$\Lambda_{th}$	Optical basicity
$\alpha_m$	Material polarizability
$\alpha_O^{2-}$	Oxide ion polarizability
$A$	Interaction parameter
$E_b$	Binding energy
$E_s$	Strain energy
$T_f$	Fictive temperature
MB	Main band
$\omega_{MB}$	Main band frequency
R	Constant of gases

## List of Figures

2.1	Diagram of the potential energy in them multidimensional configuration space for a many particle system. . . . .	7
2.2	Representative illustration of acoustic mode (top) and optic mode (bottom). . . . .	10
2.3	Graphical representation of fundamental building block of silica glasses and crystals. The white sphere represents the silicon, whereas the red spheres represent the oxygen atoms. . . . .	15
2.4	Comparison of experimental x-ray RDF for fused silica and crn model.	16
2.5	Clusters composed of (a) 3-, (b) 4-, (c) 5- and (d) 6-membered rings. The black spheres are related to the silicon atoms and the white spheres to oxygen atoms. . . . .	17
2.6	Average distribution of ring sizes of vitreous silica by computer simulations . . . . .	18
2.7	Schematic illustration of topological bond switch from 6-membered rings (a) to 5- and 7-membered rings (b). The dark path denotes the least distorted configuration in (a) and the "low-pressure" and "high-pressure" in (b). . . . .	19
2.8	Illustrative representation of boroxol rings (a) and trigonal boron (b). In (a), $\alpha$ denotes the internal bond angle and $\beta$ the external bond angle. In (b), $\gamma$ denotes the non-constrained bond between inter-structural units.	21
2.9	The superposition of orbitals in $B_2O_3$ . (1) denotes the $\sigma$ -electrons, (2) $\pi$ -electrons and (3) lone pair electrons. . . . .	21
2.10	Graphic representation of the oxygen tricluster (indicated by the arrows) in front view (a) and in side view (b), emphasizing the staggered configuration of the two silica tetrahedra. The white spheres represent the silicon, the red spheres the oxygen and blue spheres the aluminum atoms. . . . .	24

3.1	(a) Relative residual $\chi_b$ and oscillating parameter $\gamma$ over regularization parameter $\alpha$ . For further fitting, a value of $\alpha$ is chosen so that $\gamma$ is minimum while $\chi_b$ is acceptably small, indicated by the red marker in (a). (b) Corresponding data fit for a vitreous silica and comparison to experimental data. . . . .	29
3.2	Example of Nyquist diagram. Real part ( $Z'$ ) over imaginary part ( $Z''$ ) represents the complex plane. . . . .	36
3.3	Graphical representation of the total internal reflection. . . . .	38
4.1	Raman scattering spectra (a) and FTIR absorbance (b) of silica and binary aluminosilicate glasses. The inset in (b) is a zoom-in at the IR absorbance in the spectral region of 700 - 900 $\text{cm}^{-1}$ . . . . .	44
4.2	Graphical representation of the network topology in a binary aluminosilicate glass based on the assumption that all cations are in fourfold coordination and a certain fraction of oxygen triclusters is present. The ( $\text{SiO}_4$ ) and ( $\text{AlO}_4$ ) were kept in 2-dimensions to facilitate the view. . . . .	45
4.3	(a) The specific heat capacity of silica and aluminosilicate glasses. The inset in (a) is a magnification of the $C_P$ in the range of 4 - 18 K. (b) The specific heat capacity divided by the cubic temperature, revealing the Boson peak. . . . .	47
4.4	(a) Reduced low-frequency Raman spectra of silica and binary aluminosilicate glasses. (b) The VDOS extracted from low-temperature heat capacity for silica and binary aluminosilicate glasses. . . . .	48
4.5	Boson peak frequency of low-frequency Raman scattering and VDOS as a function of $\text{Al}_2\text{O}_3$ concentration in binary aluminosilicate glasses. . . . .	49
4.6	Variation of the dynamic correlation length $\xi$ in silica and binary aluminosilicate glasses as a function of alumina content. . . . .	50
4.7	Reduced density of states $g(\omega)/g_D(\omega)$ vs. the rescaled frequency $\omega/\omega_D$ . Maximum normalized intensity and maximum rescaled frequency is plotted in the inset (top right). . . . .	51
4.8	UV-Vis spectra of silica and binary aluminosilicate glasses from 175 up to 1350 nm. The inset is a magnification in the range of 175 - 220 nm. . . . .	52

4.9	(a) General overview of UV-Vis-NIR spectra of ternary aluminoborosilicate glasses. The UV absorption region related to $[\text{Yb}^{2+}]$ is shown in (b) and (c) is related to the absorption peak of $[\text{Yb}^{3+}]$ . . . . .	54
4.10	Photoluminescence spectra of ternary samples. (a) Excitation spectra of $\text{Yb}^{2+}$ ions by emission at 515 nm. (b) Emission spectra of $\text{Yb}^{2+}$ and $[\text{AlO}_4]^\circ$ centers by excitation at 240 nm. (c) Emission spectra of $\text{Yb}^{3+}$ by excitation at 920 nm. . . . .	55
4.11	Hardness and scratch hardness (a) and strain-rate sensitivity (b) of aluminoborosilicate glasses. . . . .	58
4.12	Optical basicity of $[(\text{SiO}_2) \cdot (\text{Al}_2\text{O}_3) \cdot (\text{B}_2\text{O}_3) \cdot (\text{Yb}_2\text{O}_3)]$ glass system. Green circles are the optical basicity calculated for the glass systems studied in this work. Pink triangles are the aluminoborosilicate glasses without $\text{Yb}_2\text{O}_3$ and, the red squares are the optical basicity of borosilicate glasses doped with $\text{Yb}_2\text{O}_3$ . The black dashed line located at $0.48 \text{ \AA}^3$ and the blue dashed-dot line at $0.4824 \text{ \AA}^3$ is a reference of the optical basicity of pure $\text{SiO}_2$ glass and $\text{Al}_2\text{O}_3$ in silica matrix $[\text{98.4} (\text{SiO}_2) \cdot 1.5 (\text{Al}_2\text{O}_3) \cdot 0.1 (\text{Yb}_2\text{O}_3)]$ , respectively. . . . .	59
4.13	The oxide ion electronic polarizability (left side, green squares) and the electronic polarizability (right side, red circles). . . . .	61
4.14	Raman scattering spectra (a) and normalized absorption coefficient scattering spectra (FTIR) (b) of aluminoborosilicate glasses. The inset in (b) is a zoom-in of the spectra in the region between $660$ and $780 \text{ cm}^{-1}$ and shows an appearance of B-O-B bond bending for $\text{B}_2\text{O}_3$ concentration higher than $6.85 \text{ mol } \%$ . The silica glass is shown only for reference. . . . .	62
4.15	Graphical representation of aluminum sites in aluminoborate glasses. (a) shows the aluminum site configuration for a B/Al ratio $< 1.67$ , (b) for B/Al ratio $= 2.87$ and (c) for B/Al ratio $> 2.87$ . . . . .	65
4.16	Boson peak of (a) Raman low-frequency spectra, (b) specific heat at low-temperature, (c) VDOS normalized over the frequency square as obtained by extraction from specific heat data and, (d) THz-TDS of aluminoborosilicate glasses. . . . .	67

4.17	The $\omega_{\text{Bp}}$ from low-frequency Raman (red diamonds), THz-TDS (blue triangles) and VDOS $g(\omega)/\omega^2$ extracted from low-temperature $C_P$ (green squares) for aluminoborosilicate glasses. . . . .	68
4.18	Average correlation length of aluminoborosilicate glasses. . . . .	69
4.19	Reduced density of states $g(\omega)/g_D(\omega)$ vs. the rescaled frequency $\omega/\omega_D$ . The inset shows the maximum normalized intensity $[g(\omega)/g_D(\omega)]_{\text{max}}$ and maximum rescaled frequency $[\omega/\omega_D]_{\text{max}}$ . . . . .	70
4.20	Ionic conductivity (green squares, left side) and activation energy (red circles, right side) of aluminoborosilicate glasses. . . . .	71
4.21	(a) Interferometer microscopy image of two structured lines. The line on the top is after exposure of 10 $\mu\text{J}$ and on the bottom of 9.5 $\mu\text{J}$ pulse energy. The red arrow refers to measurements focused on the “center”, while the black arrow refers to the point focused on the “edge” of the structured lines. Optical microscopy images of the structured lines of a group of higher pulse energies (b) and a group of lower pulse energies (c). . . . .	76
4.22	Photoluminescence emission spectra of silica glass after fs-laser exposure. . . . .	77
4.23	Raman spectra of pristine and two structured lines at excitation length of 514 nm. The structured lines show a very high fluorescence background. . . . .	78
4.24	The Raman spectra after EMSC model, normalization by integrated area from 750 up to 970 nm and temperature corrected for pristine, selected structured lines and compressed sample. The inset emphasize the spectra of pristine and compressed sample. . . . .	80
4.25	Fictive temperature of compressed sample and structured lines measured on the center and edge of the lines. The dashed line located at 1261 K is a reference for pristine. . . . .	81
4.26	Mass density estimated from Eq. (4.11) for structured lines and compressed sample. The dashed line located at 2.203 $\text{g cm}^{-3}$ is a reference for pristine. . . . .	82
4.27	Stresses extracted from birefringence measurements. The pulse energy increases from left to right. . . . .	84



4.28	Linewidth (FWHM) of visible Brillouin peaks at room temperature versus pulse energies (range 1.5 – 11 $\mu\text{J}$ ) for the center of lines. . . . .	87
4.29	(a) Boson peak of VDOS of the center of the lines and compressed sample. (b) the maximum Boson peak frequency ( $\omega_{Bp}$ ) for the edge and center of the structured lines. The dashed line in (b) indicate the $\omega_{Bp}$ position for pristine. . . . .	89
4.30	$\omega_{Bp}$ comparison between permanently densified silica and fs-laser structured lines. The dashed line is a reference for pristine. . . . .	90
4.31	Average correlation length of compressed silica and center of structured lines. . . . .	91
4.32	Evolution in the distribution of rings in vitreous silica before and after fs-laser irradiation. . . . .	92

## List of Tables

4.1	Mass density $\rho$ , refractive index $n$ at 633 nm, bulk modulus $K$ , Young's modulus $E$ , Poisson ratio $\nu$ , longitudinal sound velocity $\nu_L$ , transversal sound velocity $\nu_T$ , Debye temperature $\theta_D$ and, Debye frequency $\omega_D$ of silica and binary aluminosilicate glasses investigated in this study. . .	46
4.2	Mass density $\rho$ , refractive index at 633 nm $n$ , Young's modulus $E$ , longitudinal modulus $L$ , shear modulus $G$ , bulk modulus $K$ , Poisson ratio $\nu$ and, molar free volume $V_f$ of ternary aluminoborosilicate glasses investigated in this study. . . . .	57
4.3	Normalized FTIR integrated area at 932 and 1385 $\text{cm}^{-1}$ , Debye contribution $C_{Debye}$ , longitudinal sound velocity $\nu_L$ , transversal sound velocity $\nu_T$ , B/Al ratio and interaction parameter $A$ of ternary aluminoborosilicate glasses investigated in this study. . . . .	66
4.4	Densification $\Delta\rho/\rho$ , relative pressure, refractive index $n$ at 633 nm, Brillouin frequency $f_B$ , longitudinal sound velocity $\nu_L$ , transversal sound velocity $\nu_T$ , shear modulus $G$ , bulk modulus $K$ and longitudinal modulus $L$ of structured lines investigated in this study. . . . .	86



# 1 Introduction

Glasses are one of the most versatile material produced and used by the humanity. Since the oldest art objects found by investigations dated to 4000 B.C in Mesopotamia, in western Asia, until many technological applications nowadays [1]. They are present in the history of humanity for so long mainly due to their distinct optical properties. Most importantly, they are capable to guide, transmit, reflect, absorb or emit light and, thus, information [2]. Compared to other optical materials, such as crystals, glasses are cheaper, easier to shape, and thousands of different chemical compositions can be made into glass. The latter impacts on the mechanical, chemical, electrical, optical and thermal properties of the glass.

Glasses only became an engineered material at the end of the 19th century, after Otto Schott, Ernst Abbe and Carl Zeiss associated work in Jena, Germany. Schott started to develop new optical glasses compositions specifically to meet Abbe's requirements for microscope lenses and other optical instruments, whereas Zeiss was responsible for translating the scientific developments into commercial products. This new scientific approach to glass development as well as new production processes, allowed optics to become what is known nowadays as modern optical glass technology [2, 3].

Optics, more than any other field of application in technology and science, has taken advantage of the fact that glass is an engineered material [2]. Through a selection and variation of glass composition, proper manufacturing technique and post treatments, the material can be conformed in many different shapes. Due to such characteristics, it is not for nothing that optical communication networks, the backbone of the modern information society [4], are mainly based on optical glass fibers. The three largest market sectors relying on light-based products are those associated with telecommunications, transportation and biotechnologies [5]. In the context of optical fiber communication developments, further research fields have emerged. This includes especially fiber amplifiers, fiber light sources (fiber lasers, fiber supercontinuum light sources) and fiber sensor elements [4]. Not enough, transistors and processors are approaching the limits of electronic technology and a promising future is seen for light waveguides and lasers: while the 20<sup>th</sup> century was known as

the age of the electron, the 21<sup>st</sup> century is expected to be the age of the photon [6]. Computers nowadays are still based on binary signal processing. However, it has been suggested that optical computers may allow an escape from the rules of binary logic and a multivalued logical is instead permitted [7]. This would improve “deep learning” algorithms on artificial neural networks that exhibit improved computational accuracy and speed [8].

To design any optical waveguide with desirable properties, two important factors must be considered, the bulk material attenuation and geometrical limitations in the waveguide structure [9]. While the geometry is already quite well established for optical fibers by the development of the photonic crystal fibers (PCFs) [10, 11], where the microstructure dominantly controls the propagation characteristics of the light [12], typical strategies for compositional design remain empirical due to the lack of understanding regarding the topological heterogeneity.

The importance of controlling the optical losses by avoiding impurities and doping a material to achieve desirable properties is already well known since the 70’s. The first low-loss optical fiber made in 1970 [13] presented losses of silica fibers below 20 dB/km at 632.8 nm. In 1974, by introducing chemical vapor deposition technique and doping fused quartz tubes with GeO<sub>2</sub> in the core, these losses decreased to 2 dB/km [14] at 1.06 μm. They believed that the losses were due to OH impurities in siloxane present in the SiCl<sub>4</sub> starting material. In 1979, the first optical fiber was produced achieving the lower loss limit restricted by Rayleigh scattering, 0.2 dB/km at 1.6 μm [9]. Besides the method of fabrication was the same as made in 1974, they used, instead, high pure precursor materials (99.9999%). The concentration of trichlorosilane, which contains hydrogen atoms was less than 0.02%. Even nowadays, modern fibers exhibit loss values very similar to those reported in 1979.

In all these 50 years of optical fibers, so much improvement has been made in this field that not only low-loss is desired anymore. For example, several functional properties are needed concerning low attenuation in specific wavelength ranges, variation of refractive index, highly nonlinear coefficient and specific structural properties are often well beyond the characteristics of the fibers that are currently available [4]. The history of low-loss optical fibers just clearly shows that the glass has become more and more technological applied and a high-tech product. The present challenge is to

understand its structure in a more extended way, taking advantage of fundamental understanding of glass structure-properties relationships in order to design new glass compositions to develop products with straightforward applications [15].

The main difficulty in this field is the high-costs related to specific methods of fabrication, control of impurities, use of quartz-fused cylinders with low hydroxyl groups and extremely pure metal halide vapours (for example,  $[\text{SiCl}_4]$ ,  $[\text{GeCl}_4]$  or  $[\text{POCl}_3]$ ), high purity of precursors materials, high temperatures are needed because usually modifiers are avoided, and specialized people are required to operate the equipment. Due to these reasons, the literature available regarding such special glasses is limited. Furthermore, glasses made by such rigorous procedure are unique and any property is hard to be compared with a similar glass system made by other process, such as melting or sol-gel, for example.

In glasses, the structure needs to be understood in all different levels, short- and intermediate-range order [1]. However, currently methods of structural characterization (e.g., nuclear magnetic resonance spectroscopy (NMR), X-ray diffraction, Raman spectroscopy and infrared spectroscopy) usually are not effective in determining the topology and higher length-scale features.

This thesis reports a detailed analysis of the topochemical heterogeneity of binary  $[(\text{SiO}_2) \cdot (\text{Al}_2\text{O}_3)]$ , ternary  $[(\text{SiO}_2) \cdot (\text{B}_2\text{O}_3) \cdot (\text{Al}_2\text{O}_3)]$  and topological heterogeneity of fused silica after exposure to focused femtosecond laser pulses. In order to provide a complete view, combined analysis of specific heat capacity at low temperature, low-frequency Raman spectroscopy and THz-time domain spectroscopy (THz - TDS) has been fundamental to assess structural features on intermediate-range order and length scale of elastic heterogeneity. Topological heterogeneity has been investigated mainly throughout an anomaly present in the vibrational density of states (VDOS),  $g(\omega)$ , in the low-frequency range (about 1 THz), without, however, searching for any explanation of its origin. Additionally, other characterization methods, such as activation energy of ionic conductivity, UV-Vis spectroscopy, Fourier-transform infrared spectroscopy (FTIR) and photoluminescence spectroscopy has been conducted as complementary structural characterization.

## 2 Theoretical background

### 2.1 The nature of glass formation process

Glass, by a simplest definition, is a liquid that has lost its ability to flow [17]. In order to obtain a glass, such liquid has to be cooled fast enough to avoid crystallization and, at some point, the liquid freezes into a non-crystalline condensed state of matter [18–20]. Even though glasses are not necessarily formed by the cooling of an initially liquid state, indeed, the glassy state can be obtained by many different routes and appear to be fundamentally the same substance [17]. Vitreous silica, for example, can be obtained by the cooling of liquid silica, by vapor condensation, by heavy particle bombardment of a crystalline form, by chemical reaction of organosilicon compounds followed by drying, by vapor-phase reaction of gaseous molecules followed by condensation and others methods [17].

The most conventional and thoroughly studied route of the phenomenology of glasses is the cooling of a liquid with concomitant diffusive slowdown [17]. This is the “simpler” way to envisage thermodynamically their formation process. If crystals do not form during cooling, then the glassy state is entered when the cooling liquid passes through the glass transition range,  $T_g$ . At such range, the vitrifying material exhibits a growth of viscosity (or relaxation time) upon cooling or compression, but at the same time undergoes only minute structural changes. At molecular level, the structure of a glass is almost indistinguishable from that of a normal liquid, yet their viscosities differ by at least fifteen orders of magnitude [21]. The system, which undergo a metastable state, “falls out of thermodynamic equilibrium” [18]. At this situation, some kind of “amorphous order” emerges during vitrification, similarly to crystallization - but in a far less understandable way [21]. When approaching the  $T_g$  from above, the dynamic of some process, such as molecular motions or rotations, slow down so rapidly that a thermodynamic equilibrium cannot be reached due to motional and rotational degrees of freedom [22].

The glass transition temperature can be seen by thermoanalytical analysis as an anomaly in the specific heat  $C_P(T)$ . It is manifested most directly by a fast decrease of heat capacity  $C_P$  from liquid-like to crystal-like values as the liquid degrees of freedom

become kinetically inaccessible [17]. It is valid to note that not all materials vitrify in the same manner, i.e., the viscosity growth as a function of inverse temperature can differ from one material to another. These differences are exposed in the slope of the viscosity with temperature as a material approaches the glass transition, which is known as an empirical property called “fragility” [23]. Materials such silica fall in the class of “strong” glass formers, exhibiting an Arrhenius-type viscosity growth upon cooling, while “fragile” have a viscosity that increases faster than Arrhenius law [21].

The cooling rate is also intrinsically related, as higher is the cooling rate, higher is the fictive temperature,  $T_f$  [22]. Thus, the viscosity of the liquid increases dramatically at the  $T_g$  range and can be seen as a genuine “bulk” relaxation time  $\tau$  of a liquid, through Maxwell relation  $\eta = G_\infty \tau$ , which  $G$  is the infinite-frequency shear modulus. Maxwell has demonstrated that on a sufficiently short time scale the medium behaves like an elastic solid and the fluidity is therefore due to the mutual actions of the molecules, causing them to be deflected from their paths [24].

The fact of existing various and diverse phenomenological approaches makes a development of such general theory very challenging, even being studied intensively by experimental investigation and numerical simulation. The theory of the glass transitions currently represents one of the most significant unsolved topics in theoretical physics [25].

## 2.2 Cooperative relaxations and the entropy

When a liquid is supercooled isobarically, its entropy decreases considerably. The loss of entropy limits the accessible configurations and affects both the equilibrium and the transport properties of the supercooled liquid [26]. In the entropy theory, transport is conceived to be consequence of a local arrangement of particles into different configurations, which is the origin of configurational entropy [27]. Gibbs and DiMarzio separated the entropy of a deeply supercooled liquid into configurational and vibrational contributions. During the cooling of the melt, the configurational entropy decreases and requires participation of more and more particles to rearrange (reorganize) the local structure in order that transport can occur [27]. In this way, the relaxation occurs through “cooperative rearranging regions” which grow with decreasing temperature [28]. At a sufficiently low temperature, the configurational

entropy may go to zero in which case a second order transition should be expected to occur. The resulting solid is, thus, an ideal glass [27]. In real glasses, the high viscosity freezes the kinetic motions, prohibiting long relaxation times to reach zero entropy. The consequence is that the transition to the glassy state occurs even before the configurational entropy becomes zero.

Adam and Gibbs gave continuity on this topic and developed further the theory of dynamic heterogeneity. The latter gives the notion of a cooperatively rearranging region, defined as a group of molecules that can rearrange itself into a different configuration as a result of energy fluctuation. At high temperatures, the free volume allows a rapid cooperative rearrangement of groups of particles in the form of large amplitude motion. This increased cooperativity is reflected in a loss of configurational entropy, which is related to an increase in the molecular relaxation time [26]. Only a fraction of atoms in the material can move at a given time, the rest is restricted by its neighbors until the latter moves, generating a new free volume space allowing the rest moves too. The extension and dynamic of movements are also restricted by the viscosity. If the temperature decreases enough until there is no free volume of a sufficient size, the particles are trapped limited by the surrounding particles [19, 29].

Several models have been developed to understand such complex dynamical behavior. The most successful model is the Mode Coupling Theory (MCT), developed by Götze and coworkers in the 1980s [30, 31]. In few words, MCT is a dynamical theory for the behavior of density correlations functions based entirely on first principles, starting from the microscopic picture of a correlated liquid [21, 32]. Despite MCT predicts quite successfully the glass transition, however, it is generally not quantitatively accurate, and cannot account properly for the concept of fragility and the emergence of dynamic heterogeneity [21]. Until yet, a link between dynamical heterogeneity and local structure remains elusive [33].

### 2.3 Potential energy landscape

In 1969, Goldstein indicated the importance of the energy surface topology for the dynamics of glass-forming materials at low temperatures [25]. He described a useful potential energy barrier topography of viscous liquid and glass transition by looking the system on a configurational coordinate, which both the thermodynamics and the



transport properties are determined. Hence, the particles after undergoing the glass transition continues to relax, but the nature of the relaxation is very different to that in equilibrium [34]. The dynamics becomes, then, dominated by the multidimensional potential energy surface which the system can explore as a function of the degrees of freedom of the particles, as shown in Figure 2.1.

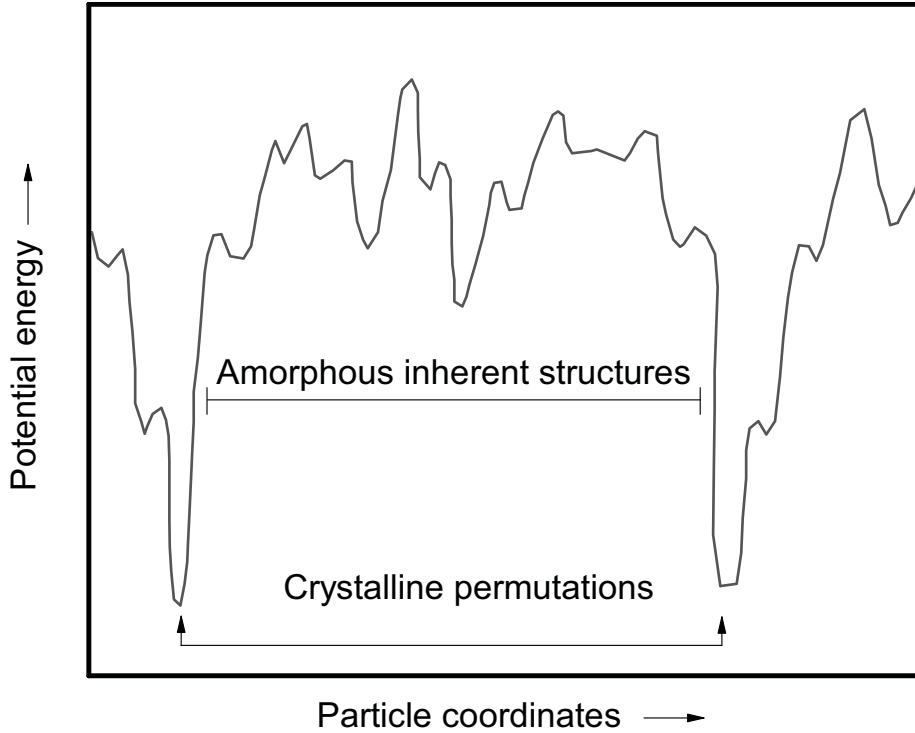


Figure 2.1: Diagram of the potential energy in them multidimensional configuration space for a many particle system. Adapted from [35] with permission from the publisher under license number 4715921386782. Rights managed by Science AAAS.

At low temperatures, the atoms in glasses and crystals vibrate in their limited free volume around quasi-equilibrium positions [19]. If these atoms are displaced by small amounts from their equilibrium positions, restoring forces are responsible to return them. The potential energy surface is a positive definite form in these small displacements. It is a system composed of  $N$  particles, in the system's potential energy, plotted as a function of the  $3N$  atomic coordinates in a  $3N+1$ -dimensional space [36]. The state of a system is represented by a point moving on the surface with a  $3N$  dimensional velocity, which average value is temperature dependent through Boltzmann factor,  $\exp(-U/k_B T)$ . Thermodynamics properties of a glass at very low temperatures are described in terms of a spectrum of harmonic vibration frequencies,

thus, a glass at low temperatures, like a crystal, is at or near a potential minimum [37]. The crystalline state, in general, consists of a potential energy surface of an absolute global minimum, and a variety of local minima of different depths, corresponding to particles arrangements that are completely lacking long-range crystalline order. The variety of local minima are separated by potential energy barriers. As temperature increases, sufficient thermal energy ( $1/2k_B T$ ) becomes available to allow transitions to trespass over the potential barriers. The lowest energy structure is the global minimum, and this corresponds to a temperature of 0 K. This is the state point of a glass that will be trapped in some one minimum. As Goldstein defined, the transition over a potential barrier in a potential energy space is local, i.e., the rearrangement process leads from one minimum to a near-by one, only those in a small region change the atomic coordinates by appreciable amounts [37].

On the one hand, classification of potential energy minima is a key to unify the understanding of condensed phase properties, which allows identification of an inherent structure in liquid that is normally obscured by thermal motions [38]. Furthermore, the vibrational density of states (VDOS) can be determined by the properties of the potential energy landscape, as suggested by Stillinger [35] and confirmed by Ruocco et al. [39] by qualitatively reproducing the VDOS and the dynamic structure factor from (harmonic) vibrational spectrum [40]. On the other hand, depicting the structure of disordered solids regarding the topology of the potential energy landscape is quite challenging [38, 41–43]. One of the main difficulties comes from  $3N+1$  - dimensional surfaces that usually cannot be visualized directly, and low-dimensional projections can be mislead [42].

## 2.4 The physics of vibrations

Any matter is constituted of atoms and all atoms naturally vibrate. The core of an atom vibrates about its equilibrium position and the electrons move around the core. In principle, the total energy depends on the coordinates and velocities of the atomic nuclei and of the electrons. In a solid material, such atoms are tied together with bonds, and consequently, they cannot vibrate independently [44]. In this manner, solids can be classified according to the dominant contribution to their cohesive energy (type of bonding): van der Waals, ionic, hydrogen-bonded, covalent solids and metals

[45].

Because of such interconnecting bonds, their association behave as an elastic medium. A crystalline solid has symmetries and the thermal vibrations can be analysed as collective modes of motion of the ions, which propagate through the lattices, along the material, while the bonds between the atoms are considered harmonic. These modes correspond to collective excitations, which can be excited and populated just like electronic states. These excitations take the form of quantized elastic waves, known as phonons [46]. A concept of phonon originates from relative motion of the atoms, rather than the motion of their center of mass – a phonon does not carry a momentum and, thus, is considered as a quasi-particle [44]. Since a solid consists of a number of  $N$  atoms, the harmonic oscillators can be treated separately by a normal-mode wave-vector  $\vec{k}$ . The energy eigenvalue for the  $\vec{k}^{th}$  mode at  $n_k^{th}$  quantum level is given by:

$$E_{n_k, \vec{k}} = \left( n_k + \frac{1}{2} \right) \hbar \omega_k \quad (2.1)$$

here,  $\hbar$  is the reduced Planck constant and  $\omega_k$  the frequency. This equation shows that the averaged energy in a classical vibration mode is equal to the energy of its corresponding quantum harmonic oscillator [47]. In the field of quantum mechanics, the normal mode of wave vector  $\vec{k}$  and frequency  $\omega_k$  is a dynamic state that possesses a discrete spectrum of energy levels, i.e.,  $n_k$  is an integer. Each phonon retains a fixed energy of  $\hbar \omega_k$  and its value solely depends upon how fast the parent normal mode vibrates [47]. There is no limit on how many phonons can be present in a normal mode. The energy-level quantum number  $n_k$  has the meaning of occupation number of phonons. Phonons can be, thus, created (and destroyed) if the energy and  $\vec{k}$  are both conserved [47]. Phonons in a crystal are in thermal equilibrium with each other. The average occupation number  $n_k$  in the  $\vec{k}^{th}$  mode in thermal equilibrium at temperature  $T$  obeys Bose-Einstein distribution function:

$$n(\omega) = \frac{1}{e^{(\hbar\omega/k_B T)} - 1} \quad (2.2)$$

At extremely low temperatures there are only a few or even zero phonons ( $\hbar\omega_k > k_B T$ ), in this manner, there is an exponentially small probability for a phonon to be present. At high temperatures ( $\hbar\omega_k \ll k_B T$ ), the number of phonons increase proportionally with temperature. The phonons dispersion can be defined by two groups: i) for a

phonon characterized by a frequency  $\omega$ , wave-vector  $\vec{k}$  and its phase velocity,  $\nu_p$ , defined by a linear dispersion  $\omega = \nu_p \vec{k}$ ; ii) for a group of phonons having frequencies around  $\omega$ , it is defined by  $\nu = \partial\omega/\partial k$  [44]. Considering harmonic oscillators, a maximum frequency for the normal modes of a linear chain is  $\omega(k) = \sqrt{2\lambda(k)/M}$ , which  $M$  is the mass of the  $i^{\text{th}}$  atom and  $\lambda(k)$  the vibration related to its wavelength. A continuous set of  $\omega(k)$  values gives two branches of phonon dispersion curves, as illustrated in Figure 2.2. At small values of  $\vec{k}$  (or long wavelength) the neighboring atoms move in phase with each other with the same amplitude [45, 48]. This is a characteristic vibration of sound waves and, for this reason, is called **acoustic** branch. The other branch has opposite signs, meaning that neighboring atoms of different types moving out of phase with the mass normalization, implying that the center of mass of the unit cell is not displaced in the wave. If the two atoms have opposite charges of them, such a mode of vibration could be excited by an electric field of appropriate frequency. This is known as **optic** branch [44, 48].

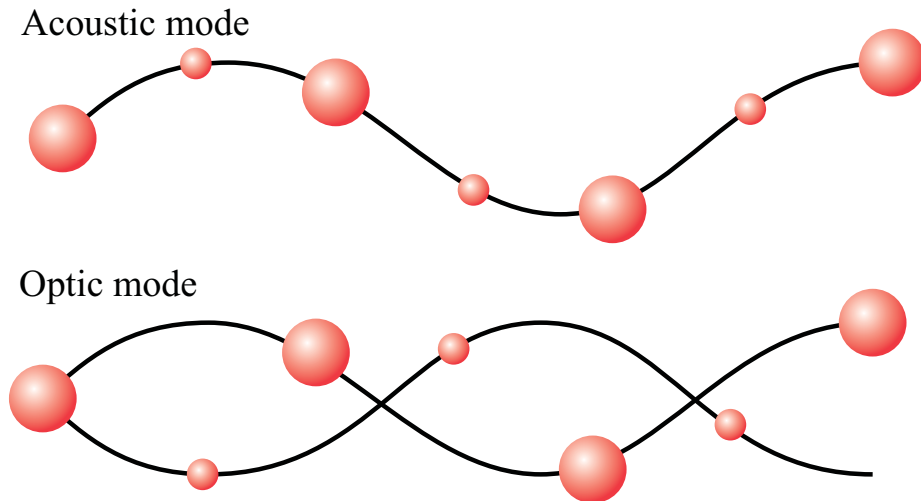


Figure 2.2: Representative illustration of acoustic mode (top) and optic mode (bottom).

The sound waves and their propagation speed are known as the sound velocity of the material. Their modulus is given by  $\vec{k} = 2\pi/\lambda$ , which  $\lambda$  is the wavelength of the sound wave. Monoatomic materials and lattices exhibit acoustic phonons only.

Materials made from more than one atom per unit cell exhibit both kinds of phonons: acoustical and optical. In three-dimensional structures, these branches are then divided into longitudinal and transversal modes [49]. For each  $\vec{k}$  state, the vibration is decomposed in three polarizations, one longitudinal (or compressional),  $\nu_L$ , which the material is alternately compressed and expanded and, two transverse waves,  $\nu_T$ , in which the displacement of atoms is sheared in alternating directions, perpendicular to the orientation of propagation [50, 51]. Glasses are essentially isotropic in all directions, therefore they follow the same conditions as three-dimensional structures [49]. Even though glasses lack long range order, most glasses possess reasonable molecular or kind of unit cell order, which gives them well-defined, though broad, modes of vibrations and phonons resonances [49].

#### 2.4.1 Debye model

In 1912, Peter Debye introduced a quantum mechanical model which provided a reasonable approximation to the observed heat capacity for solids in a wide temperature range [52]. He pointed out that the low frequencies of vibration correspond to long wavelengths, many times the atomic diameter, and can be discussed by use of the ordinary theory of deformation of elastic solids [50]. Details of the atomic structure are ignored and the solid is treated as a continuous elastic medium [52]. Even though the Debye model was developed for crystals, this model is a fundamental key to understand the phonon contribution (vibrational energy) correlated for the specific heat in solid materials.

In the Debye model a linear dispersion can be used as an approximation, which the frequency  $\omega$  and the wave-vector  $\vec{k}$  are related to the phase velocity  $\nu_p$  by the sound velocity  $\nu_{T,L}$ , as  $\omega = \nu_{L,T}\vec{k}$ . Considering one longitudinal,  $\nu_L$ , and two transversal,  $\nu_T$ , degenerate phonon branches,  $\nu_{L,T}$  is defined as Debye sound velocity,  $\nu_D$ :

$$\nu_D = \left[ \frac{1}{3} \left( \frac{1}{\nu_L^3} + \frac{2}{\nu_T^3} \right) \right]^{-\frac{1}{3}} \quad (2.3)$$

Limiting the system to a sphere, the number of allowed states having wavevector magnitude smaller than some  $\vec{k}_{max}$  corresponds to the number of states enclosed by such sphere, that is the Debye cut-off wavevector,  $\vec{k}_D$ . The number of allowed states with wavevectors less than  $\vec{k}_D$  is the volume of the sphere times the number of states

per unit volume:

$$\begin{aligned} N_{st} &= \frac{4\pi}{3} \vec{k}_D^3 \frac{V}{(2\pi)^3} \\ &= \frac{1}{6} \frac{1}{\pi^2} V \vec{k}_D^3 \end{aligned} \quad (2.4)$$

here,  $N_{st}$  is the number of states in the crystal of volume  $V$ .

From this equation, the Debye frequency can be already defined considering the linear dispersion,  $\omega_D = \nu_D \vec{k}_D$ :

$$\omega_D = \left( \frac{6\pi^2 N_{st}}{V} \right)^{\frac{1}{3}} \nu_D \quad (2.5)$$

The density of states for lattice waves in terms of the number of states in a narrow range of frequencies  $d\omega$  about  $\omega$  is given by:

$$\begin{aligned} g(\omega) &= \frac{dN_{st}}{d\omega} = \frac{V}{6\pi^2} \frac{\omega^3}{\nu_D^3} \\ &= \frac{\omega^2 V}{(2\pi^2 \nu_D^3)} \end{aligned} \quad (2.6)$$

The distribution of phonons modes inside the sphere follow the Bose-Einstein statistics. The total internal energy is:

$$U = \int \hbar\omega \frac{1}{e^{\hbar\omega/k_B T} - 1} g(\omega) d\omega \quad (2.7)$$

here,  $k_B$  and  $\hbar$  is the constants of Boltzmann and reduced Planck, respectively, and  $T$  is the temperature. Substituting  $g(\omega)$  of Eq. (2.6) in Eq. (2.7), it gives:

$$\begin{aligned} U &= 3 \int_0^{\omega_D} \frac{V}{2\pi^2} \frac{\omega^2}{\nu_D^3} \frac{\hbar\omega}{e^{\hbar\omega/k_B T} - 1} d\omega \\ &= \frac{3V\hbar}{2\pi^3 \nu_D^3} \int_0^{\omega_D} \frac{\omega^3}{e^{\hbar\omega/k_B T} - 1} d\omega \end{aligned} \quad (2.8)$$

the number 3 comes from the three modes of polarization (one longitudinal and two transversals). The heat capacity is the partial derivative of the total energy over partial derivative of the temperature,  $C_V = (\partial U / \partial T)$ :

$$\begin{aligned} \frac{\partial}{\partial T} \frac{\omega^3}{e^{\hbar\omega/k_B T} - 1} &= \frac{\omega^3}{(e^{\hbar\omega/k_B T} - 1)^2} e^{\hbar\omega/k_B T} \frac{\hbar\omega}{k_B T^2} \\ C_V &= \frac{3V\hbar^2}{2\pi^2 \nu_D^3 k_B T^2} \int_0^{\omega_D} \frac{\omega^4 e^{\hbar\omega/k_B T}}{(e^{\hbar\omega/k_B T} - 1)^2} d\omega \end{aligned} \quad (2.9)$$

The integral can be simplified by making the substitution:

$$x = \frac{\hbar\omega}{k_B T} ; \quad d\omega = \frac{k_B T}{\hbar} dx \quad (2.10)$$

$$\begin{aligned}
C_V &= \frac{3V\hbar^2}{2\pi^2\nu_D^3 k_B T^2} \int_0^{\hbar\omega_D/k_B T} \left(\frac{k_B T}{\hbar}\right)^4 \frac{x^4 e^x}{(e^x - 1)^2} \frac{k_B T}{\hbar} dx \\
&= 9N_{st} k_B \left(\frac{T}{\theta_D}\right)^3 \int_0^{\theta_D/T} \frac{x^4 e^x}{(e^x - 1)^2} dx
\end{aligned} \tag{2.11}$$

The temperature does not depend on  $\omega_D$ . Instead,  $\omega_D$  defines the Debye temperature,  $\theta_D$  by:

$$\begin{aligned}
k_B \theta_D &= \hbar \omega_D \\
\theta_D &= \frac{\hbar \nu_D}{k_B} \left(\frac{6\pi^2 N_{st}}{V}\right)^{1/3}
\end{aligned} \tag{2.12}$$

The  $\theta_D$  is a constant associated with the highest allowed vibration mode and is a property of the material. At low temperatures, when  $T \ll \theta_D$ , the integral upper limit goes to infinity and the heat capacity becomes:

$$C_V = \frac{12\pi^4}{5} N_{st} k_B \left(\frac{T}{\theta_D}\right)^3 \tag{2.13}$$

here,  $N_{st}$  can be approximated by Avogadro's number. Originally, it is valid for heat capacity at constant volume ( $C_V$ ), but it can be approximated to heat capacity at constant pressure ( $C_P$ ) for glasses since they are condensed substances in which  $(C_P - C_V)/C_P$  is less than 0.1% [53].

#### 2.4.2 Debye anomalies in glasses

Debye approximation works fairly well for solids of high symmetry containing only one kind of atom or two atoms of similar masses and bonding characteristics, but becomes increasingly inadequate as the bond type, coordination, and mass of different atoms become different. This is because vibrational frequencies are not uniformly distributed and specific covalently bonded groups retain some of their individual vibrational identity in crystals [54].

This model successfully has described the characteristics of solids until 1971, when Zeller and Pohl published a detailed work comparing specific heat, at the range between 0.05 and 100 K, of crystalline and vitreous  $\text{SiO}_2$ , Se, and silica- and germania-based glasses [55]. Their work has shown that glasses exhibit physical properties very different from those of crystalline solids, especially at low frequencies or low temperatures [56]. Since  $\theta_D$  is a physical constant of the material, a dependence of  $C_P$  proportional to  $T^3$  is expected. However, above 1 K the specific heat of glasses

deviates strongly from  $C_P \propto T^3$ , exhibiting, instead, a broad maximum in  $C_P/T^3$ . This has been further investigated and is considered as a universal feature in glasses, polymers, proteins, and other disordered and amorphous materials [57–59].

After Zeller and Pohl work, a lot of effort has been placed to understand the nature of this excess that has been called Boson peak ( $Bp$ ). At this spectral region, the temperature dependence of the strength follows the Bose-Einstein statistic characteristic of harmonic modes [60]. The very nature of the  $Bp$  remains as one of the major debated and unsolved problems of condensed-matter physics [61]. However, it is now accepted that the  $Bp$  is related to an excess in the vibrational density of states,  $g(\omega)$ , over the crystalline behavior, leading to a maximum in  $g(\omega)/\omega^2$  at frequencies  $\omega/2\pi$  (see Eq. (2.6)) of the order of  $\sim 1 - 5$  THz [61, 62]. Specific heat at low-temperature appears as a “hump” around 10 K, when  $C_P$  is plotted as  $C_P/T^3$  versus  $T$  [60], and at low frequency Raman spectroscopy such typical “hump” appears in the frequency region around 30 - 170  $\text{cm}^{-1}$  [63]. Moreover, evaluations of the  $Bp$  frequency,  $\omega_{Bp}$ , and its intensity position has already been extensively investigated. For example, available results are all in agreement: the  $Bp$  shifts toward higher frequencies and decreases in intensity when the sample becomes stiffer (increase in elastic constants) [64]. Recent studies suggested the central role played by the changes in the elastic properties to explain the  $Bp$  [65]. Truthfully, in the case of glasses, it can be assumed that the local elastic moduli fluctuate from location to location in space [66]. This is the definition itself of elastic heterogeneities of glasses and have been postulated and related to intermediate range order of glasses [66]. Accordingly, investigations of the boson peak vibrations and their interaction with acoustic waves bring complementary information about the topology and intermediate-range order of glasses [60].

## 2.5 Structure of silica, vitreous boric oxide and silicate glasses

### 2.5.1 Silica glass

The basic building block of all silicates and  $\text{SiO}_2$ -crystalline forms is the  $[\text{SiO}_4]$  tetrahedron, a structural unit with a silicon atom in the center of four surrounding oxygen atoms. All four oxygen atoms simultaneously touch the silicon atom and their external coordination partners [67], as graphically represented in Figure 2.3. Geometrically and



chemically, such structural units are very stable. Considering the electronic structure of silicon ( $1s^2 2s^2 2p^6 3s^2 3p^2$ ), relatively a small energy is required for the conversion of the ground state ( $3s^2 3p^2$ ) to four unpaired electrons ( $3s^1 3p^3$ ). All electrons in the highest energy level of silicon obtain a parallel spin moment, the spherical s orbital and the three extended p orbitals lead to a formation of  $sp^3$  hybridized atoms [67]. In the case of oxygen being the coordination partner, this brings a stable structural element. The bond angles of  $109.28^\circ$  between two oxygen atoms are close to the ideal geometrical tetrahedral angle of  $109.5^\circ$ . The Si-O bond distance is  $1.60 \text{ \AA}$ , and the edge length of the  $[\text{SiO}_4]$  tetrahedron is  $2.62 \text{ \AA}$  [67].

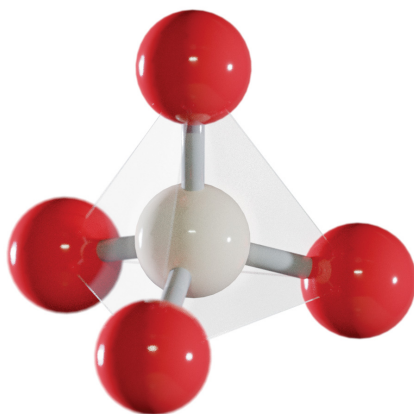


Figure 2.3: Graphical representation of fundamental building block of silica glasses and crystals. The white sphere represents the silicon, whereas the red spheres represent the oxygen atoms.

If one only considers the large difference in the electronegativity, the character of the bond between silicon and oxygen (Si-O) in this tetrahedron would be expected a predominately ionic character, however, the hybridization of the valence electrons in silicon also contributes a considerable covalent character to the bond [68]. The resultant character of such Si-O bond is a mixed bond. Pauling has shown that such bond has approximately 50/50 percent ionic and covalent character [69]. Therefore, the intertetrahedral bond angle (Si-O-Si) also results in a mixing binding, since the Si-O-Si bond angle is found experimentally around  $140^\circ$  with a range of  $\pm 20^\circ$ , while an angle of  $90^\circ$  and  $180^\circ$  corresponds to a pure covalent  $\sigma$  and a pure  $\pi$  bonding, respectively [67, 70]. These bonds are quite flexible and the differences between the units can be traced how they are linked together [70].

Silica is a prototype example of a network glass former as a continuous random network (CRN), since two building blocks share one such bridging oxygen, consequently the  $\text{SiO}_2$  stoichiometry is maintained [71], as shown in Figure 2.4. The primary polyhedral unit remains the same in glass as in its crystalline phase in the CRN model. These building blocks define a short-range configuration, with a length scale defined by the first, second, or even more distant neighbouring, as long as the bond lengths and bond angles are not distorted [72]. This usually takes up to a distance of about 1- 3 Å [73].

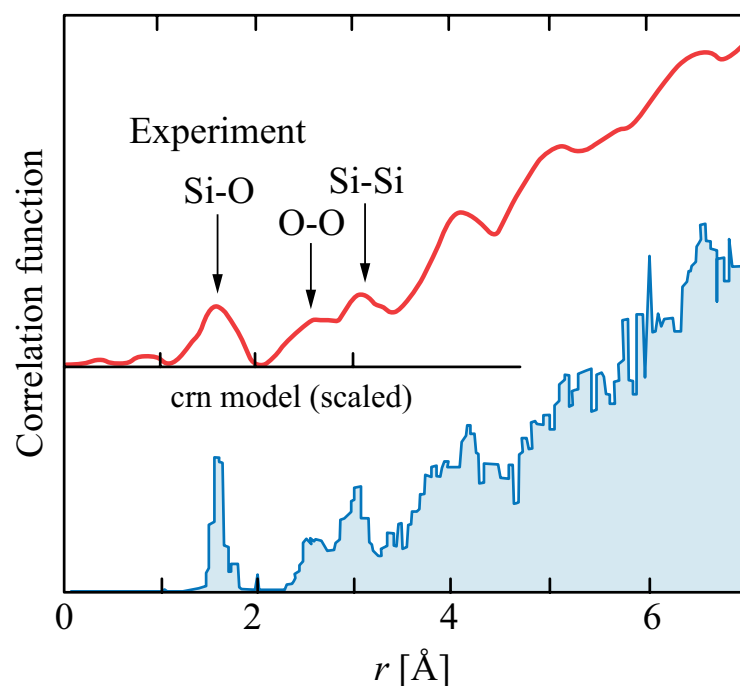


Figure 2.4: Comparison of experimental x-ray RDF for fused silica and crn model. Adapted from Ref. [74] with permission from the publisher under licence number 4716521294767. Rights managed by Springer Nature.

The silica tetrahedra are linked via bridging oxygen at all four corners, which results in formation of a 3-dimensional network [68]. It is important to note that the dimensionality of glass network can exist in both 2 and 3 dimensions. For example, vitreous silica consists of tetrahedral building blocks  $[\text{SiO}_4]$ , while boron can be present as trigonal building blocks  $[\text{BO}_3]$ .  $[\text{SiO}_4]$  forms naturally a 3-dimensional network, while  $[\text{BO}_3]$ , being planar, becomes 3-dimensional only if distorted. Extension of bond lengths and bond angle within reasonable limits in combination with rotation

around single bonds leads to complete loss of periodicity over long distances [72].

The connectivity of these building blocks in the glass defines closed paths along the bonds, forming rings [72]. However, such rings vary in quantity of Si-O bonds. The smallest ring known is constituted of 3 Si-O bonds (3-membered rings), the most abundant consists of 5-, 6- or 7-membered rings, while it is still possible to find rings which 10, 12 or even more Si-O bonds are present [72]. Some examples of types of rings are depicted in Figure 2.5.

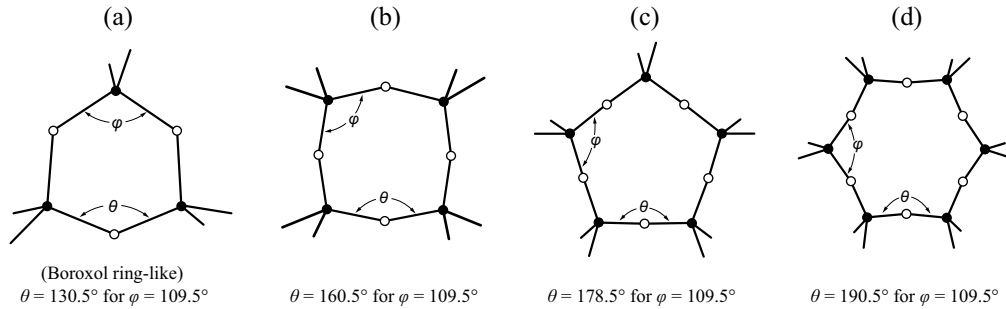


Figure 2.5: Clusters composed of (a) 3-, (b) 4-, (c) 5- and (d) 6-membered rings. The black spheres are related to the silicon atoms and the white spheres to oxygen atoms. Adapted from Ref. [75] with permission from the publisher under license number 4715930899303. Rights managed by Elsevier B. V..

It is important to note that the angle between the O-Si-O bond ( $\varphi$ ) is kept unaltered. Besides 2-membered rings are statistically probable, following Uchino et al. [76], such rings are less probably to be found in  $\text{SiO}_2$  glass because of its large strain energy (1.85 eV). Figure 2.6 shows the distribution of ring sizes by computer simulations on two- and three-body terms of fused silica [77].

The concept of dimensionality allows the possibility of arrangement of building blocks in a more extended order and, also, in a more organized way than that predicted by a purely random building blocks connection scheme [78]. A convincing evidence that vitreous silica cannot be predicted by a random network is given by the two distinctive lines seen at  $495 \text{ cm}^{-1}$  ( $D1$ ) and  $606 \text{ cm}^{-1}$  ( $D2$ ) at the Raman spectra, due to their unusually sharp features, which suggests regular configurations. The  $D1$  and  $D2$  lines are assigned to in-phase breathing motions of oxygen atoms in puckered 4- and planar 3-membered rings, respectively [76]. Most of the 3- and 4-membered rings have such regular configuration and stable structure, even if they are connected by Si-

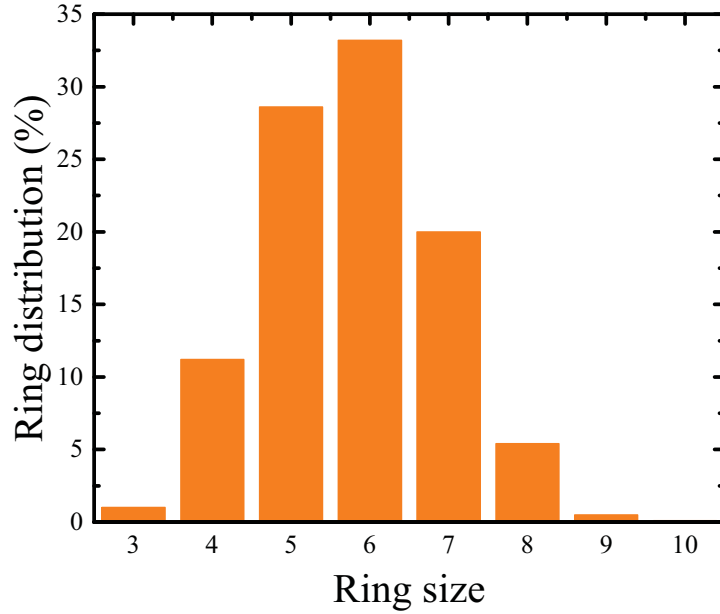


Figure 2.6: Distribution of ring sizes of vitreous silica by computer simulations. Adapted from Ref. [77] under the Creative Commons CC BY License. Rights managed by The Optical Society of America (OSA).

O-Si bond with other types of silica rings. On the other hand, geometries larger than 6-membered rings are considerably distorted, resulting in irregular configurations. For example, 5- and 7-membered rings may contribute to yielding “low-pressure” bond-parts and “high-pressure” bond-parts, respectively, in silica glass [79] (Figure 2.7).

Another important aspect about the glass structure is the free volume, which is usually ignored in structural models. It should be noted that these are likewise constituent of the glass empty spaces structure [80]. Besides they surely have an influence on some properties of glass and are crucial to understand any behavior of volume-dependent properties such as the density, refractive index and thermal expansion coefficient, this is a very challenging topic to be investigated [78, 80]. Theoretically, it amounts to approximately 20 - 25 % of the molar volume and increases with increasing alkali content [78]. The average free volume is defined considering the elastic modulus,  $E$ , Poisson’s ratio  $\nu$  and a correlation with the activation energy  $E\eta$  for this free volume, by the equation:  $V \approx 3(1 - 2\nu)E\eta/E$ .

The extension of the rings can reach over significant distances within the structure. Beyond adjacent tetrahedra, they can form a reasonable semblance to some positional

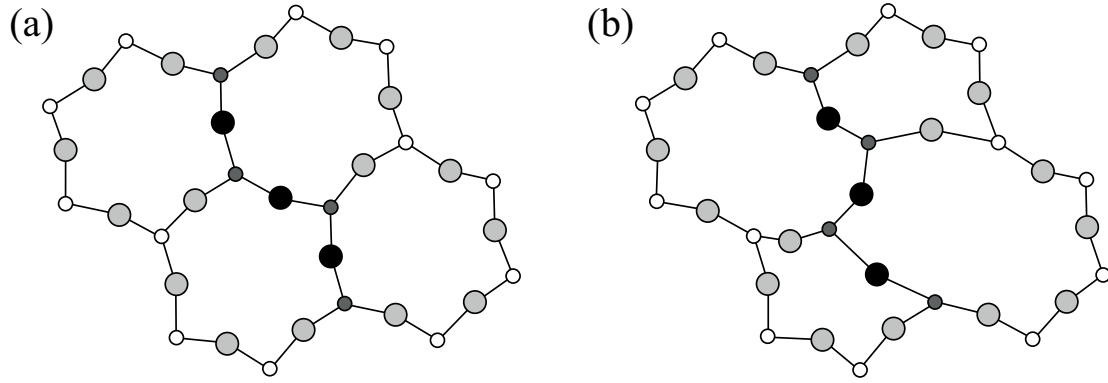


Figure 2.7: Schematic illustration of topological bond switch from 6-membered rings (a) to 5- and 7-membered rings (b). The dark path denotes the least distorted configuration in (a) and the "low-pressure" and "high-pressure" in (b). Adapted from Ref. [79] with permission of the publisher under license number 1005555-1. Rights managed by IOP Publishing.

ordering and other interconnected units to constitute what is known as intermediate-range-order (IRO). Despite its delimitation or length scale still retains definition, it is closely associated with the network topology [72, 81, 82].

A unique characteristic of vitreous silica is the presence of small rings, 3- and 4-membered rings. The influence of the small rings is expected to affect the intermediate-range properties in a severe way due to the small angles and planarity of such structural units [83–85]. Evidences of IRO in  $v\text{-SiO}_2$  have been demonstrated mainly by diffraction experiments, which imply on existence of a pseudo-periodicity characterized by scale of the first sharp diffraction peak (FSDP), appearing at the wave number  $Q1 = 1.51 \text{ \AA}^{-1}$  [79], which corresponds to a distance estimated as  $R1 = 2\pi/Q1 \approx 4.2 \text{ \AA}$ . Another evidence of IRO is characterized by Rayleigh scattering loss, that is an indication of presence of density fluctuation in atomic arrangements, which is caused by non-organized distribution of a group of atoms [86].

Although the IRO still lacks a substantial definition, its existence is more speculative. Since none model has been proved a unique structure until now, all models for intermediate range order must be treated only as potential descriptions of a network and not as absolutely established [78]. This comes from the difficult of characterization, even by the most sophisticated current methods of investigation. Several terms, such as structural domains, local composition fluctuation, density fluctuation etc. has

been used to define such regions [81]. In general, IRO can be regarded as resulting from SRO [87]. The characteristics of IRO can be affected by changing the distribution of bond angles, by compression or thermal treatment, for example, modifying the statistical distribution of the ring sizes. Changes in the chemical composition also causes a disorder because the SRO itself is altered due to changes in the first coordination shell, which is known as chemical disorder [72]. All cases can alter completely the local connectivity and generally implies in a topological disorder [72].

### 2.5.2 Vitreous boric oxide

Boric oxide is a glass former. This glass is hard to crystallize by itself, but it does only under pressure. Even though in crystalline compounds boron occurs in both triangular  $[\text{BO}_3]$  and tetrahedral coordination  $[\text{BO}_4]$ , in vitreous configuration the building blocks are composed only by triangular  $[\text{BO}_3]$  [78]. The electronic configuration of boron is  $1s^2 2s^2 2p^1$ , resulting in a  $sp^2$  hybridization. Compared to oxygen, the size of boron ion is very small. It can fit into the trigonal void created by 3 oxide ions in mutual contact to form the  $[\text{BO}_3]$  triangle [88]. As expected from electronegativity considerations, the B-O bond character is more covalent than the Si-O bond. Besides several structural studies have been performed on  $\text{B}_2\text{O}_3$ , proposed different models of their connectivity have been a long subject of discussion. The type of building block is well established, the molecular building block is the planar  $[\text{BO}_3]$  triangle. The bond length between B-O is 1.37 Å and O-O is 2.37 Å.

The first proposed model of vitreous  $\text{B}_2\text{O}_3$  was described as all triangles connected by bridging oxygen (BO) at all three corners to form a linked continuous random network [78]. This model has been further discarded because of the extremely sharp peak at  $808 \text{ cm}^{-1}$  present at Raman spectroscopy, which is attributed to the in-phase breathing of oxygen ions inside of planar threefold rings (3  $[\text{BO}_{3/2}]$ ) triangles, called boroxols [89]. A graphical representation of boroxol ring and  $[\text{BO}_3]$  triangle is depicted in Figure 2.8 (a) and (b), respectively. Barrio et al. have shown by computer simulations that, in the real glass, not all boron atoms form rings and it is not crucial as far as the vibrational density of states is concerned [90]. Following NMR spectroscopy, the  $[\text{BO}_3]_{\text{ring}}$  has an internal bond angle ( $\alpha$ ) of  $120^\circ$  (Figure 2.8 (a)). The external bonds ( $\beta$ ) of the boroxol can bond to other  $[\text{BO}_3]_{\text{ring/non-ring}}$ . Although they are linked

to the rings of the glass network, it is less constrained than inside the rings, being centred around  $133^\circ - 134^\circ$  [91]. By quantum chemical calculations, the non-constrained  $[B-O-B]_{\text{non-ring}}$  bond angle ( $\gamma$ ) is around  $132^\circ$ . On the staggered configuration,  $\gamma$  is around  $131.6^\circ$  and eclipsed  $137^\circ$  [92] (Figure 2.8 (b)).

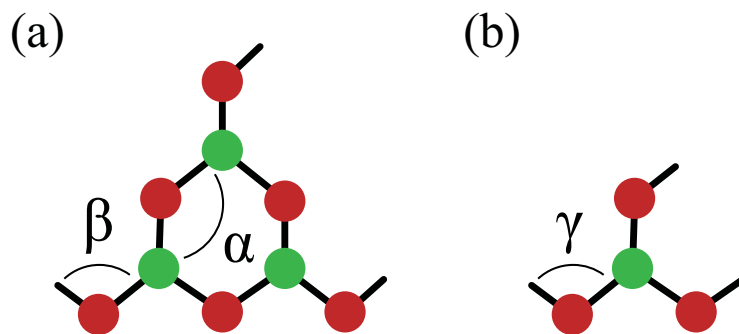


Figure 2.8: Illustrative representation of boroxol rings (a) and trigonal boron (b). In (a),  $\alpha$  denotes the internal bond angle and  $\beta$  the external bond angle. In (b),  $\gamma$  denotes the non-constrained bond between inter-structural units.

The vitreous boric oxide is, therefore, constituted of a non-ring  $[BO_3]$  matrix, with regions formed by boroxol rings, configuring the intermediate-range order [78].

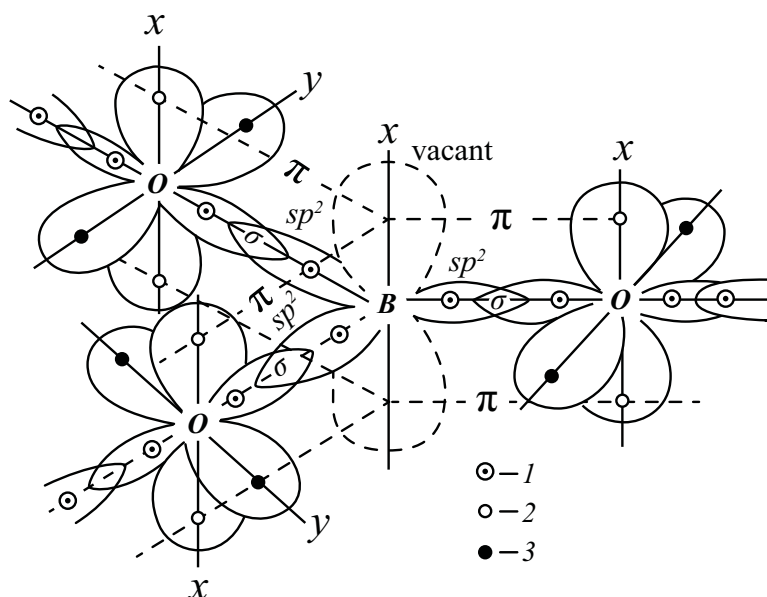


Figure 2.9: The superposition of orbitals in  $B_2O_3$ . (1) denotes the  $\sigma$ -electrons, (2)  $\pi$ -electrons and (3) lone pair electrons. Adapted from Ref. [88] with permission from the publisher under licence number 4716530350601. Rights managed by Elsevier.

The hybridization of the  $[\text{BO}_3]$  units leaves one empty 2p orbital, that is not used for  $\sigma$ -bonding and, thus, is available for  $\pi$ -bonding. The existence of  $\pi$ -bonds is possible only for  $[\text{BO}_3]$  units because it is a trigonal planar unit. Such bonding allows the electronic charge to spread onto the boron atoms, leading to a delocalization of the electron density throughout the  $[\text{BO}_3]$  network [93], as depicted in Fig 2.9. This delocalization also contributes to stability of boroxol [88].

Since the building block of this network is planar, a 3-dimensional linkage can occur only if the network is crumpled. In this way, the primary bonds exist only on the plane of the triangle, bond in a third dimension is very weak and the structure is easily disrupted. One consequence of this structure, for example, can be found in the low  $T_g$  of vitreous boric oxide, which is only 260 °C [78].

### 2.5.3 Binary aluminosilicate glasses

The binary  $\text{SiO}_2\text{-Al}_2\text{O}_3$  glass system has been extensively investigated because of its great importance in glass technology, ceramics and geosciences. However, no unified picture of the structure of this glass is well settled. This comes from the difficulties on the glass preparation, since without any modifier it requires very high temperatures to be formed ( $> 1730$  °C) and phase separation may occur for concentrations higher than 8 mol%  $\text{Al}_2\text{O}_3$ , depending on the fabrication method used. Additionally, its structure is very sensitive to the preparation method and history of the glass [94]. Nuclear magnetic resonance spectroscopy is also challenging, because triple quantum magic angle spinning (3 QMAS) technique is not quantitative for aluminum, making the determination of populations of silicon sites with varying numbers of aluminum neighbors very model-dependent [95, 96]. This system has recently received attention from the glass community, because it has been recognized that  $\text{Al}_2\text{O}_3$  into  $\text{SiO}_2$  may increase the solubility of rare-earths (RE). Usually an Al/RE ratio of about 10 is necessary to ensure good dissolution of rare-earth clusters in silica [97].

It is already well known that  $\text{Al}_2\text{O}_3$  alone is not a glass former. The electronic configuration of aluminum is  $1s^2 2s^2 2p^6 3s^2 3p^1$ . The three valence electrons ( $3s^2 3p^1$ ) mean that aluminum has an optimum oxidation state of +3. Considering Pauling's packing rule, the ratio between ionic radius of  $[\text{Al}^{3+}]$  and  $[\text{O}^{2-}]$  gives a value about 0.38 (ionic radius of  $[\text{Al}^{3+}] \sim 0.53$  Å, while  $[\text{O}^{2-}] \sim 1.4$  Å). This value corresponds to a



preference for octahedral/tetrahedral boundary of  $[\text{Al}^{3+}]$ , with coordination number of 6/4, respectively. Neither conditions would allow  $[\text{Al}^{3+}]$  to form glass, because i) aluminum with coordination number of six requires the neighbouring oxygen ions to be 4 coordinated to maintain the charge balance, violating the first Zachariasen's rule and ii) aluminum with coordination number 4 would lead to a located negative charge on the aluminum  $[\text{AlO}_4]^-$ , overloading energetically the system. On the other hand,  $\text{Al}_2\text{O}_3$  can exist as intermediate component in glasses, besides the chemical ordering of aluminum is very complicated when built into the tetrahedral Si-O network [98]. To achieve local charge neutrality,  $[\text{Al}^{3+}]$  ions need a different environment of  $\text{O}^{2-}$  ions than those originating from  $[\text{SiO}_4^{4+}]$  [98].

In glasses, aluminum may be found mainly in 4- fold coordination, and scarcer in 5- and 6-fold coordination, the latter can happen only when either modifiers are present or at higher  $\text{Al}_2\text{O}_3$  concentrations. Computer simulations and NMR spectroscopy have reported that in binary aluminosilicate glasses at low  $\text{Al}_2\text{O}_3$  concentrations ( $< 13 \text{ mol } \%$  and  $< 6 \text{ mol } \%$   $\text{Al}_2\text{O}_3$ , respectively) [98], aluminum atoms are mainly four-fold coordinated by oxygens. However, without further charge compensation, the oxygen would be incited to bridge three tetrahedra (instead of two) to maintain the charge balance. This oxygen is known as oxygen tricluster. A graphic representation of such tricluster is shown in Figure 2.10. It is worth mentioning that in Figure 2.10 (b) the two  $[\text{SiO}_4]$  tetrahedra is in a staggered configuration related to each other.

While the existence of such triclusters is still debated, evidence of their presence in aluminosilicate glasses has been obtained by NMR spectroscopy [99, 100] and through computational simulation [101, 102]. The appearance of triclusters is an indication for the different local ordering of different cationic species, aluminum and silicon [101]. Moreover, it was suggested that  $[\text{AlO}_4]$  tetrahedra in tricluster configuration is distorted compared to 'normal'  $[\text{AlO}_4]$  [99, 103], which manifests as a denser packing of the  $[\text{AlO}_4]$  tetrahedra than of the  $[\text{SiO}_4]$  tetrahedra [101]. In fact, the presence of triclusters in aluminosilicate glasses would induce a tightening of the silica tetrahedral rings and, potentially, initiate a crystallization process [99, 104].

The aluminum avoidance principle (or Lowenstein's rule), maintains that two  $[\text{AlO}_4]$  tetrahedra may not be linked together through the oxygen. [105, 106]. Even after more than 60 years, this has been and still is a subject of much controversy.

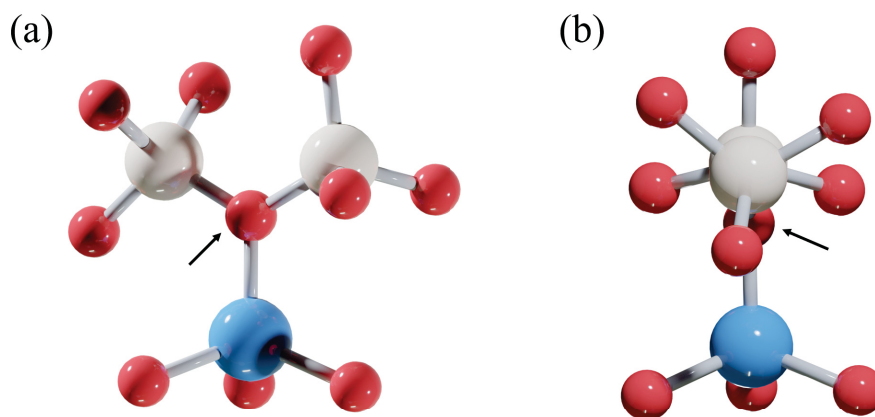


Figure 2.10: Graphic representation of the oxygen tricluster (indicated by the arrows) in front view (a) and in side view (b), emphasizing the staggered configuration of the two silica tetrahedra. The white spheres represent the silicon, the red spheres the oxygen and blue spheres the aluminum atoms.

While [Al-O-Al] is found, for example, in zeolites and ternary  $[(\text{SiO}_2) \cdot (\text{NaAlO}_2)]$  and  $[(\text{SiO}_2) \cdot (\text{CaAl}_2\text{O}_4)]$  glass system [95], some works suggest that the aluminum avoidance principle operates at longer bond distances than previously supposed. Not only the tetrahedral [Al-O-Al] bonds are unstable in aluminosilicates, but the system strives to minimize the number of tetrahedral aluminum coordinated to any silicate tetrahedron [106]. Molecular dynamics simulations on binary  $[(\text{Al}_2\text{O}_3) \cdot 2 (\text{SiO}_2)]$  system have shown that different chemical ordering of aluminum and silicon, in local length scales, also leads to structural ordering on intermediate length scales of the order of 1 nm [98, 101]. At the same composition, it was found oxygen tricluster atoms in combination with three nearest neighbour aluminum, violating Lowenstein's rule [107]. One explanation is because at 33 mol %  $\text{Al}_2\text{O}_3$  concentration, the system seems to enter a microphase separation, which could, in principle, compensate the charge balance. However, at low concentration of  $\text{Al}_2\text{O}_3$  (fully polymerized network) the conjunction of oxygen tricluster may not follow such behavior, but instead, coordinate to two silicon atoms and one aluminum. It was also found by computer simulations that the number of oxygen triclusters of the form [O - 3 (Si, Al)] per Al atom is of the order of one, which is expected to yield charge neutrality in the local environment of Al atoms [98]. Investigations of the degree of aluminum avoidance in aluminosilicate

glasses, suggested that the distribution of framework cations in aluminosilicate glasses is not fully random, but instead, with significant ordering resulting from aluminum avoidance [95].

#### 2.5.4 Binary borosilicate glasses

Although investigations of borosilicate glasses have been extensively explored, only few works comprises the simple binary  $\text{SiO}_2\text{-B}_2\text{O}_3$  system (modifier-free). This comes from the difficulty on handling the  $\text{B}_2\text{O}_3$  precursor due to its hygroscopic behavior, and due to high temperatures ( $\sim 2000\text{ }^\circ\text{C}$ ) required to prepare silica-rich compositions. At such temperatures,  $\text{B}_2\text{O}_3$  vaporizes, limiting to vapor-deposition methods [108, 109]. In this scenario, a study from 1972 by Tenney and Wong [110] about infrared vibrational spectra of vapor-deposited binary borosilicate glasses can be considered a pioneer on describing the atomic structure of such glasses. From their results, they conclude that boron in tetrahedral coordination is absent and, thus, the boron and silicon atoms are three- and fourfold coordinated by oxygens, respectively, and are randomly distributed in the quasi-lattice. This gives three options of linkage: [Si-O-Si], [Si-O-B] and [B-O-B]. They have shown an important aspect of the [B-O-Si] bond, that the glasses are deposited as chemical, rather than just mechanical mixtures. Their results have been recently confirmed by computer simulations and NMR investigations [91, 92, 111–113]. Moreover, NMR spectroscopy has shown that  $[\text{BO}_3]$  mixes very well with  $[\text{SiO}_4]$  and are practically randomly distributed and connected with each other [92, 111, 112].

Binary borosilicate glasses may also contain a fraction of boroxol rings, which amount is proportional to  $\text{B}_2\text{O}_3$  concentration [92]. While in pure  $\text{B}_2\text{O}_3$  glasses a population of 70 % of boroxol rings is expected, only 17 % has been found in a borosilicate sample with ratio Si/B of 0.75 [92]. Boroxol rings also mix well with the silica network. This brings direct consequences to the topology disorder, most of it presumably derives from the flexibility of the bond bridging angle, which rises to broad bond angle distributions, increasing the disorder around the mixed [B-O-Si/B] sites [91, 92].

There is a common phenomenon in borosilicate glasses called “boron anomaly”, where a boron speciation starts in presence of a certain concentration of a glass mod-

ifier (excess of oxygens) [114, 115]. In the  $[\text{BO}_3]$  configuration, boron is electron deficient, i.e., it has just 6 electrons in its outermost orbit, and can accept 2 more electrons in the form of dative bond. If oxide ions are available in the glass composition, then the formation of tetrahedral  $[\text{BO}_4]$  over trigonal  $[\text{BO}_3]$  are thus readily formed, and the glass are mainly composed of those two species [116]. However, in a system which oxygens are not in excess, it is expected that such speciation is not likely to happen. Indeed, NMR investigation on binary borosilicate glasses containing 40 mol %  $\text{B}_2\text{O}_3$  has shown that only three-coordinated boron is found [111]. Later, a very systematic NMR study on binary and ternary  $[\text{SiO}_2 \cdot \text{B}_2\text{O}_3 \cdot \text{Na}_2\text{O}]$  borosilicate glasses confirms the same for a group of binary glasses with  $\text{B}_2\text{O}_3$  concentration varying between 10 and 90 mol %, [112]. Molecular dynamics simulations also indicate the presence of only trigonal  $[\text{BO}_3]$  as framework unit for  $[(\text{B}_2\text{O}_3) \cdot 5 (\text{SiO}_2)]$ ,  $[(\text{B}_2\text{O}_3) \cdot 4 (\text{SiO}_2)]$  and  $[6 (\text{B}_2\text{O}_3) \cdot 4 (\text{SiO}_2)]$  binary borosilicate glasses [113]. This result seems reasonable considering that there are not so many oxygens available to be shared and  $[\text{BO}_4]$ , as  $[\text{AlO}_4]$ , has a negative charge associated.

## 3 Experimental

### 3.1 Powder sintering technology

All samples were prepared by reactive powder sintering process (REPUSIL)[4, 117, 118]. This technology was developed by the Institute of Photonic Technology (IPHT, Jena) in cooperation with Heraeus Quarzglas. Basically, this method is a modification of the solution-doping for production of the Al/RE-doped silica layer for optical fiber preforms. The doping and purification process are achieved outside the silica tube by using a suspension-doping step. Because of this outside step, larger amounts of uniformly doped silica can be produced.

The process starts with synthetic porous  $\text{SiO}_2$  nano-particles, which is dissolved in an aqueous silica slurry. The latter is doped by addition of a solution of co-dopants and/or rare earth (eg. Yb, Al, B etc). Thereafter, the slurry mixture is cast into molds, dehydrated and isostatically pressed to yield rod-shaped preform bodies of about 20 mm in diameter and a length of few centimeters. After several dehydration and purification steps by chlorine at elevated temperatures to remove impurities from raw materials like iron, and, most importantly, bonded water [4], the cleaned glass is fed into a matched fused silica tube (Heraeus F300). The sintering process of the preform is carried out by applying mild vacuum between the preform body and silica tube at temperatures of up to 2200 °C (obtained from passing an oxygen-hydrogen burner). Subsequent vitrification process is also carried out at the same temperature. The final preform is a cylinder with the doped glass in the core and a silica ring around. The ring can be easily removed by further either physical or chemical process.

All samples investigated in the Chap. 4.1 and Chap. 4.2 were produced by REPUSIL process by the optical fiber technology department under supervision of Stephan Grimm, Kay Schuster and Katrin Wondraczek at Leibniz-Institute of Photonic Technology.

### 3.2 Low-temperature heat capacity

Heat capacity ( $C_P$ ) is, by its simpler definition, the amount of heat in Joules required to raise the temperature of a substance by 1 Kelvin. The heat capacity at low-temperature reveal much information about the electronic properties of a solid, for example the lattice or vibrational properties, in particular the low-frequency phonon density of states, acoustic modes, and optic modes [119]. The heat capacity can be measured at low-temperature at constant pressure  $(\frac{dQ}{dT})_P$ . The result is then divided by the mass to obtain the *specific* heat capacity.

The VDOS can be directed extracted from ( $C_P$ ) data through the relation:

$$C_P \approx C_V = 3N_A k_B \int g(\omega) x^2 \frac{e^x}{(e^x - 1)^2} d\omega \quad (3.1)$$

here,  $N_A$  and  $k_B$  is the Avogadro number and Boltzmann constant, respectively, and  $x$  is  $(\hbar\omega/k_B T)$ .

For the binary aluminosilicate system (Chap. 4.1) the extraction of the VDOS from  $C_P$  data was made following Surovtsev et al. [120]. The difficulty on solving Eq. (3.1), is that it presents an *ill-posed* inverse mathematical problem in which the solution is very unstable at perturbations. A Tikhonov regularization scheme was applied in order to mathematically stabilize the solution by adding a functional, which is weighted with the regularization parameter  $\alpha$ . However, the choice of  $\alpha$  is crucial in order to obtain stable solutions without loss of information by excessive smoothing. Knowing that the slope of the reduced density of states  $g(\omega)/\omega^2$  in the frequency range switches only once from positive to negative (instead of oscillating), the higher frequency could be mathematically filtered-out. The choice of  $\alpha$  thus presents a kind of low-pass filtering based on physical knowledge. Two figures of merit were used in order to optimize  $\alpha$ : (i) the relative root-mean-square deviation  $\chi_b$  and (ii) the integral of the squared derivative of  $g(\omega)/\omega^2$ , denoted  $\gamma$  and reflecting oscillatory behavior of the solution. Figure 3.1(a) shows the variations of these two parameters over  $\alpha$  for pristine. Figure 3.1(b) shows the corresponding fit of the same sample.

For the ternary aluminoborosilicate system (Chap. 4.2), the extraction of VDOS from specific heat capacity was calculated by coherent-potential approximation (CPA) [121–123]. The CPA was developed by Schirmacher et al. for topologically disorder system [121]. Using replica of field-theoretical approach, a CPA equation is derived

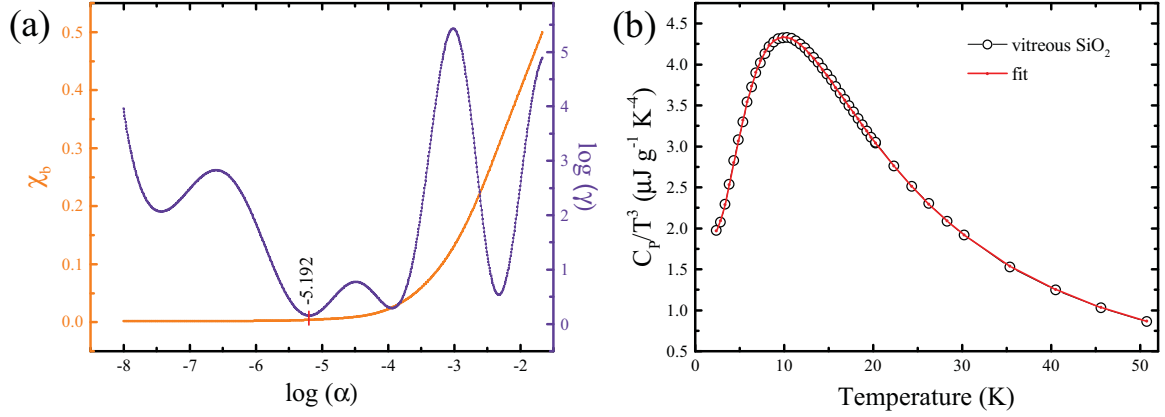


Figure 3.1: (a) Relative residual  $\chi_b$  and oscillating parameter  $\gamma$  over regularization parameter  $\alpha$ . For further fitting, a value of  $\alpha$  is chosen so that  $\gamma$  is minimum while  $\chi_b$  is acceptably small, indicated by the red marker in (a). (b) Corresponding data fit for a vitreous silica and comparison to experimental data.

by taking it as a saddle point of an interacting matrix field theory. In between, a coarse-graining procedure in closed packed hard sphere structure is used to average the Green's function [121]. It assumes that in each cubic box the shear modulus is homogeneous and the size of the box is larger than the correlation length of shear modulus fluctuation, therefore all boxes are considered uncorrelated. This CPA is suitable from macroscopic to intermediate range but not for short range ( $< 1$  nm) structures. Usually it is considered a lognormal distribution of shear modulus that is sampled over these boxes of various sizes (intermediate to macroscopic range). Such a distribution function would allow one to consider from weak to strong disorder without limitation [124]. Using the derived CPA equation, both transversal- and longitudinal sound velocities as well as Debye cutoff wave-vector  $\vec{k}_D = (6\pi^2 N/V)^{1/3}$  as inputs, the low-temperature  $C_P$  data were fitted.

Low-temperature heat capacity experiments were measured by Pierre Lachkar under supervision of Dr. Jean-Luc Garden at Institut Néel (University Grenoble Alpes) (Chap. 4.1) and Prof. Stefan Ebbinghaus at Institute of Chemistry, Inorganic Chemistry (University of Halle-Wittenberg) (Chap. 4.2).

Both computational methods of VDOS extraction were made by Dr. Zhiwen Pan at Otto-Schott-Institute (University of Jena).

### 3.3 Vibrational spectroscopy

Raman and Infrared (IR) spectroscopy are complementary techniques and usually both are required to completely measure the vibrational modes of a molecule. In general, Raman spectroscopy is more suitable at symmetric vibrations of non-polar groups, while IR spectroscopy is best at the asymmetric vibrations of polar groups [125].

IR spectroscopy measures transitions between molecular vibrational energy levels as a result of the absorption. This interaction between light and matter is a resonance condition involving the electric dipole-mediated transition between vibrational energy levels. In Raman scattering, the incident photon is of much higher energy than the vibrational quantum energy, and loses part of its energy to the molecular vibration with the remaining energy scattered as a photon with reduced frequency [125]. The inelastically scattered components consist of information on the phonons of the system. Raman scattering is in principle a three-step process (1) the change in polarizability causing a transition from the ground state to a virtual excited state (2) creation (or annihilation) of phonons by an electron-phonon interaction and (3) return to the electronic ground state. The scattering, thus, depends on electronic polarizabilities of the atoms and the dipole moments accompanying the changes in polarizabilities [126]. When the phonons are due to low frequency acoustic modes, it corresponds to Brillouin scattering with an energy range of  $0.1 - 1 \text{ cm}^{-1}$ . When these phonons have energies in the infrared region, as high as  $10^2 - 10^3 \text{ cm}^{-1}$ , it corresponds to Raman scattering.

The IR and Raman vibrational bands are characterized by their frequency (energy), intensity (polar character or polarizability), and band shape (environment of the bonds). The frequencies of these molecular vibrations depend on the masses of the atoms, their geometric arrangement, and the strength of their chemical bonds (eg. covalent, ionic, metallic, etc) [125]. The intensity of Raman scattering, however, depends on a number of factors, which includes the frequency of the scattered light (energy separation and hence populations), the density of vibrational states, the damping constant etc. The incident frequencies are shifted both in positive and negative direction by magnitudes corresponding to vibrational frequencies. Stokes lines



correspond to the creation and anti-Stokes to the annihilation of phonons [126]. Considering a diatomic molecule with a single spring force constant (classical harmonic oscillator),  $K$ , with the two atoms vibrating against each other, it is easy to show by setting up the equation of motion that this is governed by the relation:

$$\omega = \frac{1}{2\pi} \sqrt{K \left( \frac{1}{m_1} + \frac{1}{m_2} \right)} \quad (3.2)$$

here,  $m_1$  and  $m_2$  are the masses of the atoms in a molecule. For larger molecules consisting of several springs and therefore several spring constants, there will be several ways in which the atoms are displaced [126].

In the case of glasses, minimal assumptions about the vibrational modes of a glass are made (1) the vibrations are harmonic so that they can be analyzed into normal modes; (2) the vibrations couple to light through the displacement dependence of the electronic polarizability of the material; and (3) the coherence length of the normal modes is short compared with optical wavelengths.

In 1970, Shuker and Gammon demonstrated that the Raman intensity of the Stokes lines is related to the vibrational density of states by [127]:

$$I(\omega) \approx \frac{1 + n(\omega)}{\omega} C(\omega) g(\omega) \quad (3.3)$$

here,  $g(\omega)$  is the density of states and  $C(\omega)$  is the factor which depends on the correlation length associated with the modes in the vibrational band. Thus, the spectrum consists of the weighted sum of the densities of states of various bands. The explicit temperature dependence can be removed by dividing the measured intensities by Bose-Einstein distribution (Eq. (2.2)). This is known as reduced Raman spectrum. It has been reported that the depolarization ratio  $HV$  Raman spectrum mimics the VDOS, and that the dominant line in  $HH$  Raman spectrum marks the low-frequency limit of the bands that are due mainly to central forces [128].

Another important point is about the symmetry of a molecule. It defines which vibrations are Raman and/or IR active. Symmetry elements include planes, axes and a center of symmetry. In a molecule with a center of symmetry, vibrations that *retain* the center of symmetry are IR inactive and may be Raman active. Such vibrations generate a change in polarizability during the vibration but no change in a dipole moment. In other case, vibrations that *do not retain* the center of symmetry, may

change the dipole moment and, then, Raman become inactive, but may be IR active [125].

Low-frequency Raman spectroscopy measurements and analysis in Chap. 4.1 counted with contribution of Omar Benzine at Otto-Schott-Institute (University of Jena).

### 3.4 Terahertz time-domain spectroscopy

Terahertz time-domain spectroscopy (THz-TDS) is a vibrational spectroscopy technique that probes the infrared active vibrational modes in the far-infrared and sub-millimeter region of the electromagnetic spectrum using ultrashort pulses of coherent THz radiation (0.1 - 4 THz  $\sim$  3 - 33  $\text{cm}^{-1}$ ) [129]. The THz regime also coincides with the rates of inelastic processes in solids, such as tunneling and quasi-particle scattering [130].

THz-TDS is based on electromagnetic transients generated opto-electronically with use of femtosecond duration laser pulses. Optically-gated detection allows direct measurement of the THz electric field with a time resolution of a fraction of a picosecond [130]. As a time-domain technique, THz-TDS is able to detect both the amplitude and phase of the terahertz electric field, thereby allowing a direct extraction of the complex refractive index without the necessity of applying Kramers-Kronig relation for evaluation of the real and imaginary parts of the refractive index [131]. Disordered materials exhibit a universal frequency dependence of the optical absorption in the far-infrared (FIR) regime [131]. The simplest first-order perturbation process of photon interaction with atomic vibrations in FIR absorption characterized by a linear absorption coefficient,  $\alpha(\omega) = C(\omega) g(\omega)$ , which is measured by IR spectroscopy, is found generally as  $\alpha(\omega) \propto \omega^2$  in the FIR domain. The coupling coefficient, as for Raman (Eq. (3.3)), quantifies the degree of coupling between IR photons and atomic vibrations [132].

The THz-TDS experiments were made by Tatsuya Mori at Division of Materials Science (University of Tsukuba).

### 3.5 UV-Vis spectroscopy

UV-visible spectroscopy is, in principle, an absorption spectroscopy technique. It relies on a sample containing species that absorb light in the ultraviolet to visible range. The UV-visible part of the electromagnetic spectrum corresponds to electronic excitation and the energy levels depend on the chemical bonds within the specimen.  $\sigma$ -electrons, involved in covalent bonds, absorb high energy photons in the UV region, whereas  $\pi$ -electrons absorb photons at longer wavelengths, often in the visible region [133]. These absorptions relates to the electronic transitions of the molecules from a ground state to an excited state. When less energy is required for this transition, the wavelength of absorption is higher and vice versa [134]. The Lambert-Beer law forms the mathematical-physical basis of the attenuation of a light beam travelling through a light-absorbing medium:

$$I(\nu) = I_0(\nu)e^{[-\alpha(\nu)l]} \quad (3.4)$$

here,  $I_0(\nu)$  is the intensity of a transmitted beam in the absence of the absorbing species,  $\alpha(\nu)$  is the absorption coefficient of the medium for light of frequency  $\nu$ , and  $l$  is the thickness of the sample, where the light has to pass through out. If a sample contains molecules, aggregates or regions smaller than the wavelength of light, incoming light will be scattered elastically. This is known as Rayleigh scattering and its dependence is proportional to the wavelength by  $1/\lambda^4$ . Since the light scattered will not reach the detector of the spectrometer, this will be interpreted by the instrument as absorbed light. This scattering is obviously more intense towards the blue end of the spectrum and can be seen as the first absorption band.

The absorption spectroscopy is complementary to fluorescence spectroscopy, i.e., the fluorescence concerns the electronic transitions from the excited state to the ground state, while absorption spectroscopy measures transitions from the ground state to the excited state. For this reason, it is very useful to measure the UV-visible spectroscopy to map the absorption bands (photoluminescence excitation) before measuring the photoluminescence spectroscopy.

### 3.6 Photoluminescence spectroscopy

Photoluminescence can be defined as the radiation emitted from a molecule or a solid. Basically, an external source incites the material, which specific molecules absorb a quantity of energy and transfer it into electronic excited states. To return to its ground electronic state, the molecules emit partially the energy in form of photons [135]. Photoluminescence spectroscopy, in turn, is a highly sensitive method that involves the selective photoabsorption of an analyte by a light source, followed by detection of the radiative decay (photoemission) process [136].

The optical path layout of the photoluminescence measurement is quite similar to the UV-Vis spectroscopy measurement, except that it is possible to collect the emitted photons from any side of the sample, either the front side where the probing light incidents, or the back side, or the edges [137].

The spectral transitions, which lead to the absorption spectrum, are related to the energy diagram on the basis of the Franck-Condon principle. This principle is based on the fact that electrons move and rearrange at a much higher speed than that of the vibrational movement of the nuclei of a molecule. In absorbing energy provided by light, the system acquires the associated excitation energy and moves to an upper electronic excited state. There are many ways in which the system can return to the lower energy state. The excess energy can be lost to the vibration, rotation, and translation of the surrounding molecules or ions. This thermal degradation transforms the excitation energy into thermal motion of the environment, generating heating. Another possibility is radiative decay, which occurs when the molecule or ion pair loses its excitation energy as a photon. In this case, two different radiative decay mechanisms are possible: i) fluorescence, when the radiation emitted in a transition between states of the same spin multiplicity and ii) phosphorescence, when the radiation emitted in a transition between states of different spin multiplicity.

The measurements were made by Yicong Ding at Otto-Schott-Institute (University of Jena).

### 3.7 Impedance spectroscopy

The impedance spectroscopy is an extension of resistance of an ideal resistor, but in a sinusoidal alternating current (AC) circuits, defined by  $R \equiv E/I$  ( $R$  is the electrical resistance,  $E$  the voltage and  $I$  the current), which is a measure of the ability of a circuit to resist the flow of electrical current. The impedance spectroscopy measures the resistance and capacitance properties of a material via application of a sinusoidal AC excitation signal. An impedance spectrum is obtained by varying frequency over a defined range [138]. In this way, the impedance of the system ( $Z(\omega)$ ) can be given by the ratio between the input and output signal in function of time  $t$ :

$$Z(\omega) = \frac{E_t}{I_t} = \frac{E_0 \sin(\omega t)}{I_0 \sin(\omega t + \Phi)} \quad (3.5)$$

here,  $\omega$  is the angular frequency,  $E_t$ ,  $E_0$ ,  $I_t$  and  $I_0$  are the total and initial voltage and current, respectively, and  $\Phi$  is the phase shift.

Since the relation between the input and output of signals in the system is complex, usually an Euler's relationship is applied. The impedance is then represented as a complex number:

$$Z(\omega) = Z_0(\cos\Phi - i \sin\Phi) = Z'(\omega) - i Z''(\omega) \quad (3.6)$$

where ( $Z'$ ) and ( $Z''$ ) is composed of a real and imaginary part, respectively.

If the real part is plotted over the imaginary part, a "Nyquist plot" is obtained. In an ideal material, only one semicircle is present. However, in a real material, other responses and sometimes more than one semicircle can be present. For example, in ceramic materials, more than one semicircle has origin in different regions with distinct electrical properties [139]. Just to illustrate, a Nyquist plot of a sample from Chap. 4.2, [94.1 ( $\text{SiO}_2$ ) · 1.5 ( $\text{Al}_2\text{O}_3$ ) · 4.3 ( $\text{B}_2\text{O}_3$ )], over 6 variations of temperature is shown in Figure 3.2.

In order to define the resistivity ( $R$ ) of an ionic conductor, an intersection of the semicircle with the  $x$  axis is used. This is done by fitting the semicircles by  $f = (x - x_c)^2 + (y - y_c)^2 - r^2$ . Concomitantly, in a sample with a given area  $A$  and thickness  $d$ , under an electrical uniform current, the resistivity ( $\rho_r$ ) of the ionic conductor is defined by:

$$\rho_r = R \frac{A}{d} \quad (3.7)$$

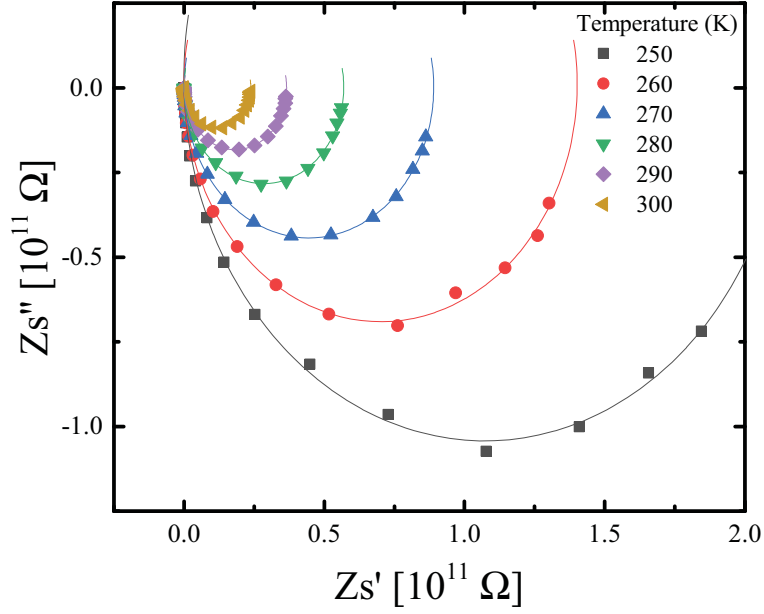


Figure 3.2: Example of Nyquist diagram. Real part ( $Z'$ ) over imaginary part ( $Z''$ ) represents the complex plane.

The reciprocal of the resistivity is the conductivity ( $\sigma$ ), that is used to describe the capacity of electrical conduction of a material.

The Arrhenius equation plays a dominant role in classical studies of chemical kinetics. It expresses the dependence of the rate constant over a wide range of temperature in terms of only two parameters, where  $A$  is the pre-exponential factor and  $E_A$  is the experimental activation energy in Joules by the following equation [140]:

$$\sigma T = A \exp\left(\frac{-E_A}{k_B T}\right) \quad (3.8)$$

here,  $T$  is the temperature in Kelvin.

The measurements and analysis were made by Yang Xia at Otto-Schott-Institute (University of Jena).

### 3.8 Polarization microscopy

To evaluate the polarization microscope data, the Eq. (3.9) has been derived from Fresnel equations to describe the transmission  $T$  of two birefringent crystals with their

ordinary and extraordinary axis orthogonal to the optical path:

$$T = \sin^2\varphi \sin^2 \left[ \frac{\pi}{\lambda} (R_C - R_S) \right] \quad (3.9)$$

This formula requires the ordinary axis of the compensator to be aligned with extraordinary axis of the sample and vice versa (subtraction position) while the angle with the polariser is  $\varphi$ . Here,  $R_C$  is the optical retardation of the compensator which can be varied and  $R_S$  the retardation of the sample, which is constant. When the compensators retardation values are increased, the brightness of each pixel changes proportional to the second  $\sin^2$ -term. This is valid for every point in the field of view. Then the brightness variation of every pixel could be observed with a computer program and fit  $\sin^2[\pi/L(x-r)]$  to the gathered curve, being  $x$ , the optical retardation of the image center, an independent variable and  $L$  and  $r$  are fitting parameters. In this way, it is possible to get the optical retardation of each pixel as well as its corresponding vacuum wavelength. The same procedure was applied to the baseline measurement. The relative retardation of every pixel can be calculated as

$$\frac{R_S}{\lambda_G} = \frac{r}{L} - \left( \frac{r}{L} \right)_{zero} \quad (3.10)$$

here, the zero term is the baseline optical retardation for the corresponding pixel. From the optical retardation, the stress was calculated by the stress-optic law [141]:

$$\Delta\sigma = \frac{R_S}{dC} \quad (3.11)$$

where  $d$  is the sample thickness and  $C = 3.54 \text{ nm mm}^{-1} \text{ MPa}^{-1}$  is the stress optical constant [142]. This sign convention has been cross checked by the sensitive tint of the first-order red compensator under white light incidence.

The measurements, calculations and imaging were made by Aaron Reupert at Otto-Schott-Institute (University of Jena).

### 3.9 Refractive index

The refractive index,  $n$ , of a dielectric may be expressed as the summation of the contribution of  $i$  oscillators of strength  $f_i$  each, as:

$$\frac{n^2 - 1}{n^2 + 2} = \frac{4\pi}{3} \frac{e^2}{m\varepsilon_0} \sum_i \frac{f_i}{\omega_i^2 - \omega^2 + i\Gamma_i\omega}, \quad (3.12)$$

where  $e$  and  $m$  are the charge and mass of the electron, respectively,  $\omega_i$  is the resonance frequency, and  $\Gamma_i$  is a damping constant of the  $i^{\text{th}}$  oscillator. Therefore, refractive index is a complex quantity, which the real part contributes to the phase velocity of light (the propagation constant), whereas the sign of the imaginary part gives to either loss or gain [143].

The refractive index of all samples was measured by a principle of total internal reflection. A sample of refractive index  $n_{\text{sample}}$  is clamped to a prism of known refractive index  $n_{\text{prism}}$ . For obvious reason, the refractive index of the prism must be higher than the sample. The attenuation coefficient  $\alpha$  is related to the imaginary refractive index  $n_i$  as  $\alpha = 2n_i\omega/c$ , where  $\omega$  is the laser frequency and  $c$  is the speed of light. If the sample is transparent ( $\alpha = 0$ ), the incident angle  $\theta_i$  encounter a critical angle  $\theta_c$  at which the angle of refraction  $\theta_r$  becomes  $90^\circ$ . Snell's law is then applied to obtain  $n_{\text{sample}} = n_{\text{prism}}\sin\theta_c$  [144]. Figure 3.3 shows a graphical representation of this principle.

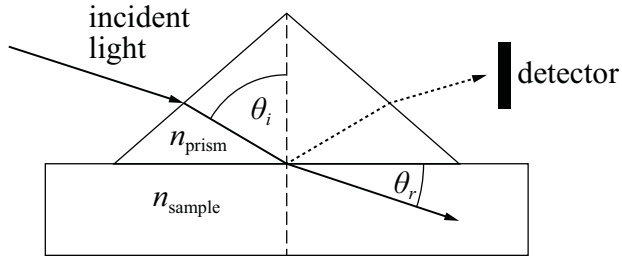


Figure 3.3: Graphical representation of the total internal reflection.

### 3.10 Femtosecond-induced structural modification in glass

Femtosecond (fs) laser processing of glass leads to a direct writing of complex refractive index structures, such as diffractive elements, waveguides, and local refractive index modification [143].

The phenomenon of non-linear photo-induced modifications is related to the spot of a weakly diffracting Gaussian beam in a medium:

$$D = \frac{0.61\lambda}{NA} \quad (3.13)$$

here,  $NA$  is the numerical aperture of a beam and  $\lambda$  is the wavelength and  $D$  is the



image resolution. Since the incoming beam induces a refractive index change in the medium, the power is dependent on the profile of the beam, and in the case of the Gaussian trapped beam, the critical power required to reach self-trapping is defined as [143]:

$$P_{cr} = \frac{\pi(0.61\lambda)^2}{8n \times n_2} \quad (3.14)$$

here, the  $n_2$  is the coefficient of non-linear refractive index.

The self-focusing threshold of silica, at a wavelength of 1  $\mu\text{m}$ , is equivalent to around  $10^{14} \text{ W cm}^2$ . This means that a single pulse with a peak power of this value propagates spatially unaltered in silica, forming a spatial soliton. The center of the beam has higher intensity than its wings, leading to a weak refractive index profile, which closely resembles the intensity profile. The fast collapse of the propagating beam increases the intensity parametrically, leading to optical damage. The high intensities cause the breakage of molecular bonds through intense ionization and the generation of heat, with enormous pressures building up within the bulk of the glass [143].

The femtosecond laser modification lines of fused silica were made by Maximilian Heck at Institute of Applied Physics, Jena.

### 3.11 Brillouin scattering

Brillouin scattered light originates from light interaction with propagating acoustic phonons. This phenomenon is due to an excitation of the bulk property of the material, such as propagating period density fluctuations of an acoustic wave in the medium [145]. The Brillouin frequency shift  $\omega_B$  is orders of magnitude smaller than the optical frequency, meaning that the frequency of the incident light  $\omega_L$  is proportional to the frequency of the scattered light [145]. The linear wavelength dispersion is given by:

$$\omega_B = \vec{k}_B \nu = 2\omega_L \left(\frac{n}{c}\right) \nu \sin\frac{\theta}{2} \quad (3.15)$$

where  $c/n$  is the velocity of light in the medium,  $\nu$  is the velocity of the acoustic phonon and  $\theta$  is the angle between the wavevectors of incident and scattered light.

A frequency broadening of the scattered radiation occurs due to the finite lifetime of the excitation  $\tau_Q$ . For an exponentially damped matter excitation, the line shape

is Lorentzian with the full width at half maximum intensity,  $\Delta_\nu$ , given by [145]:

$$\Delta_\nu = \frac{\Gamma}{2\pi} = \frac{1}{2\pi\tau_Q} \quad (3.16)$$

here,  $\Gamma$  is the angular frequency linewidth.

At room temperature, the width of the Brillouin peak is mainly due to dynamic attenuation [146].

Brillouin scattering experiments were measured by Alexander Veber under supervision of Prof. Dominique de Ligny at Institute of glass and ceramics (University of Erlangen-Nuremberg).

### 3.12 Mechanical properties

The sound velocity in a material is a constant dependent on its chemical and structural nature. Since the sound velocity is directly related to elastic properties of the material, the bulk modulus ( $K$ ), elastic modulus ( $E$ ), Poisson's ratio ( $\nu$ ), longitudinal modulus ( $L$ ) and shear modulus ( $G$ ) can be defined as [147]:

$$K = \rho \left( c_L^2 - \frac{4}{3}c_T^2 \right) \quad (3.17)$$

$$E = \rho \left[ \frac{3c_L^2 - 4c_T^2}{(c_L/c_T)^2 - 1} \right] \quad (3.18)$$

$$\nu = \frac{c_L^2 - 2c_T^2}{2(c_L^2 - c_T^2)} \quad (3.19)$$

$$L = \rho c_L^2 \quad (3.20)$$

$$G = \rho c_T^2 \quad (3.21)$$

here,  $\rho$  is the mass density of the material and  $c_T$  and  $c_L$  are the transversal and longitudinal sound velocities, respectively.

The free volume ( $V_f$ ) can be calculate by the mass density ( $\rho$ ), the molar fraction ( $f_i$ ) and molar mass of species  $i$  ( $M_i$ ) [148]:

$$V_f = \frac{\sum f_i M_i}{\rho} - \sum f_i V_i \quad (3.22)$$

the molar volume ( $V_i$ ) is defined as  $V_i = 4/3N\pi(x r_a^3 + y r_b^3)$ , which  $r_a$  and  $r_b$  are the radii of the cation and ion species, respectively, and  $x$  and  $y$  denote their stoichiometry.

The Vickers hardness  $H_V$  is determined through microindentation

$$H_V = \frac{1.8544 P}{d^2} \quad (3.23)$$

where  $P$  is the applied load and  $d$  is the average length of the two projected diagonals of the imprint (in mm). In this work, the applied load was 0.981 N during a penetration time of 15 s.

The sound velocities, hardness and strain-rate sensitivity were measured by Dr. René Limbach at Otto-Schott-Institute (University of Jena).

## 4 Results and discussion

### 4.1 Binary aluminosilicate glasses

In this chapter, the binary system  $[\text{SiO}_2 \cdot \text{Al}_2\text{O}_3]$  is considered, both as a fundamental model for a mixed tetrahedral network and for the wide relevance of aluminosilicates, ranging from geosciences to optical fiber and high-power laser gain media [149]. In the latter, alumina is one of the most significant dopants used in silica-based active fiber laser applications. This is primarily for improving the solubility of rare-earth ions and to prevent their clustering. Besides that, it has impact on other important properties, such as reducing the strength of Brillouin and Raman scattering, making it particularly attractive for high-power glass fiber laser applications [150–152]. Typical strategies for compositional design remain, however, empirical due to the lack of understanding regarding the structural role of alumina on intermediate length scale. On the other hand, high dopant capacity allows for shorter fiber lengths and/or significantly higher power levels.

The low-frequency modes of binary aluminosilicate glasses through analysis of low temperature heat capacity and low frequency Raman scattering is explored to find quantitative scaling parameters and, subsequently, relations between chemical composition, intermediate-range order and the length-scale of elastic heterogeneity. This is to enable a design strategy for glasses with high dopant capacity, but also to provide new insight at the structural origin of the excess in the vibrational density of states and the Boson peak of aluminosilicate materials.

The composition investigated in this study is a binary system  $[(100-x) (\text{SiO}_2) \cdot x (\text{Al}_2\text{O}_3)]$  glasses, with  $2.05 < x < 7 \text{ mol}\%$ . Chemical analysis of all such-derived samples was conducted through wavelength-dispersive electron probe microanalysis (WD-EMPA). Besides the primary constituents, impurities of chlorine and water were present in the samples with average concentrations in the doped zone of less than  $0.15 \text{ mol}\%$  ( $\text{SiCl}_4$ ) and  $< 10 \text{ ppm}$  (OH, determined by infrared optical spectroscopy). In the following, samples are denoted according to their  $\text{Al}_2\text{O}_3$  concentration,  $x = 0, 2.05, 3.20$  and  $7.00$ , (Table 4.1). Sample homogeneity was examined by optical microscopy and through transmission electron microscopy (TEM-EDS). It was con-

firmed that they do not contain any kind of crystals, pores or bubbles. Furthermore, on a length-scale of 5 – 3000 nm, they did not contain any visible fluctuations in chemical composition or density.

Since the binary aluminosilicate system is modifier-free (and concentration of impurities are very low), it is expected a fully polymerized network, which all building blocks are consisted of tetrahedral  $[\text{SiO}_4]$  and  $[\text{AlO}_4]$ . Corresponding Raman spectra are shown in Figure 4.1 (a). All glasses exhibit similar band shape, except for the range from 1050 up to  $1250\text{ cm}^{-1}$  that is associated to  $[\text{Si-O}]$  stretching vibrations in  $[\text{SiO}_4]$  tetrahedra connected to one Al polyhedron. In the lower frequency region, the band at around  $430\text{ cm}^{-1}$  is related to rocking and symmetric bending motions of bridging oxygen (BO) species [153]. The position of this band remains unchanged with addition of  $\text{Al}_2\text{O}_3$ . This indicates that there is no substantial change in the  $[\text{Si-O-Si}]$  bond angle [94]. On the other side, the total integrated area from 165 up to  $470\text{ cm}^{-1}$  increases almost linearly with addition of  $\text{Al}_2\text{O}_3$ , meaning that the amount of larger rings is increased. The sharp peaks at approximately 490 and  $600\text{ cm}^{-1}$  correspond to symmetric bridging oxygen bending vibrations in 4- and 3-membered rings [75]. For both peaks, the relative intensity decreases with increasing  $\text{Al}_2\text{O}_3$  content, further indicating that the addition of  $\text{Al}_2\text{O}_3$  affects the ring-size distribution in the  $\text{SiO}_2$  glass system. In the mid-frequency region, the band at about  $800\text{ cm}^{-1}$  results from the motion of Si atoms in their tetrahedral oxygen cage [154]. The high-frequency bands at about  $1050 - 1250\text{ cm}^{-1}$  are usually assigned to Si-O stretching vibrations of tetrahedral  $[\text{SiO}_4]$  groups. The increasing intensity with addition of  $\text{Al}_2\text{O}_3$  suggests that an interconnected  $[\text{Si-O-Al}]$  network is formed [94].

IR absorbance spectra of the binary glasses and a silica reference are shown in Figure 4.1 (b). All glasses exhibit similar band shape, dominated by the characteristic vibrations of vitreous silica, i.e., asymmetric stretching of  $[\text{O-Si-O}]$  ( $\sim 1120\text{ cm}^{-1}$  and  $1230\text{ cm}^{-1}$ ) and  $[\text{O-Si-O}]$  bending ( $\sim 800\text{ cm}^{-1}$ ) [94]. The band at  $1120\text{ cm}^{-1}$  is observed to shift slightly (to lower frequency) when  $\text{Al}_2\text{O}_3$  is present, while the  $1230\text{ cm}^{-1}$  band broadens somewhat at the same time [155, 156]. It was previously suggested that this is related to the extent of disorder in the  $\text{SiO}_2$  network [157], which seems to increase with the addition of  $\text{Al}_2\text{O}_3$ . This interpretation agrees with the gradually disappearing shoulder at  $1200\text{ cm}^{-1}$  [158].

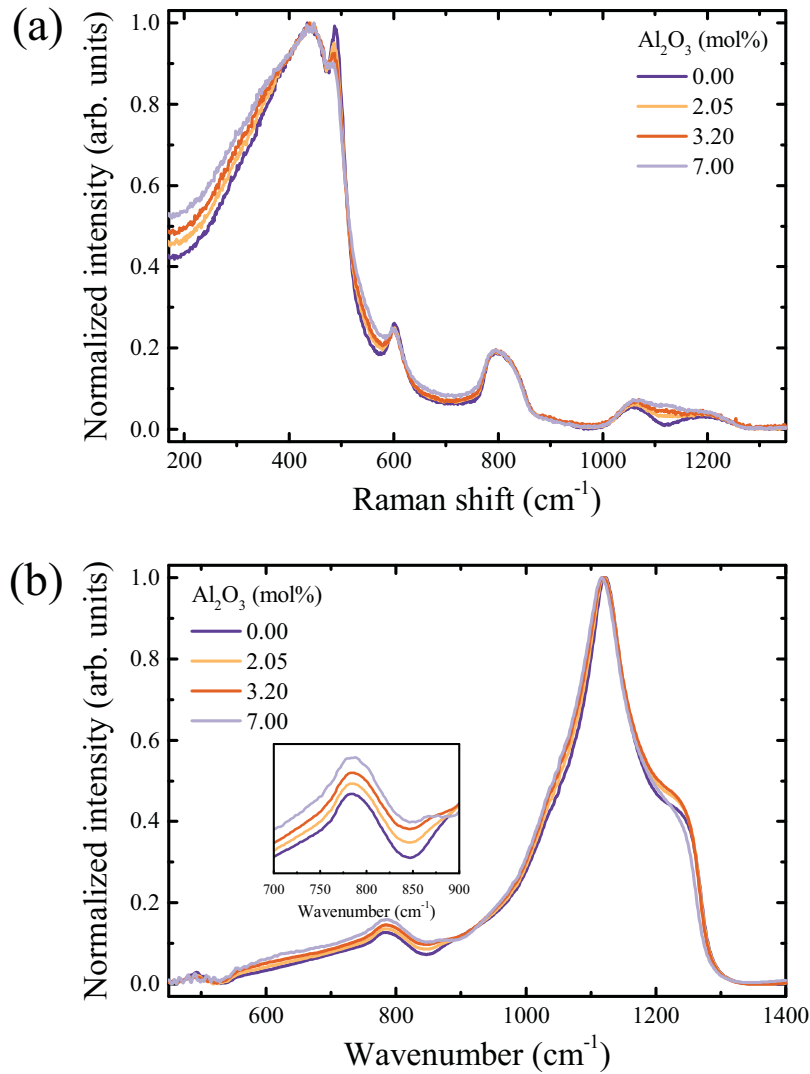


Figure 4.1: Raman scattering spectra (a) and FTIR absorbance (b) of silica and binary aluminosilicate glasses. The inset in (b) is a zoom-in at the IR absorbance in the spectral region of 700 - 900  $\text{cm}^{-1}$ . Adapted from Ref. [149] under the Creative Commons CC BY License. Rights managed by Springer Nature.

Since there are no distinct variations in the shape of the characteristic band envelope, it is assumed that aluminum speciation is dominated by four-fold coordination,  $[\text{AlO}_4]$ . There are several studies that found evidence for the predominance of this coordination state in low-alumina aluminosilicate glasses. NMR spectroscopy and extended X-ray absorption fine structure (EXAFS) have shown that for  $\leq 0.4 \text{ mol\%}$  of  $\text{Al}_2\text{O}_3$ , the aluminum ions are predominantly four-fold coordinated [159, 160]. Amorphous thin films were investigated by X-ray emission spectroscopy, from which it was concluded that all aluminum ions are coordinated tetrahedrally for samples contain-

ing up to 5 mol % of  $\text{Al}_2\text{O}_3$  [161]. Schmücker et al. [103] have shown by NMR that aluminosilicate glasses containing up to 10 mol % of  $\text{Al}_2\text{O}_3$  contain predominantly aluminum at four-fold coordination. Finally, Pfeleiderer et al. [98] arrived at the same conclusion through computational simulation of ensembles with up to 13 mol % of  $\text{Al}_2\text{O}_3$ .

Replacement of one silicon ion for one aluminum ion, without further charge compensation and in tetrahedral coordination, incites one oxygen to bridge three tetrahedra (instead of two) to maintain the charge balance [94, 103, 104, 162]. While triclusters could be bonded either to two aluminum and one silicon or to two silicon and one aluminum [163]. According to the principle of aluminum avoidance proposed by Loewenstein [105], it is assumed that the latter species is usually dominant. In Figure 4.2, an illustration of the structure of binary  $[\text{Al}_2\text{O}_3 \cdot \text{SiO}_2]$  glasses is provided in accordance with these arguments.

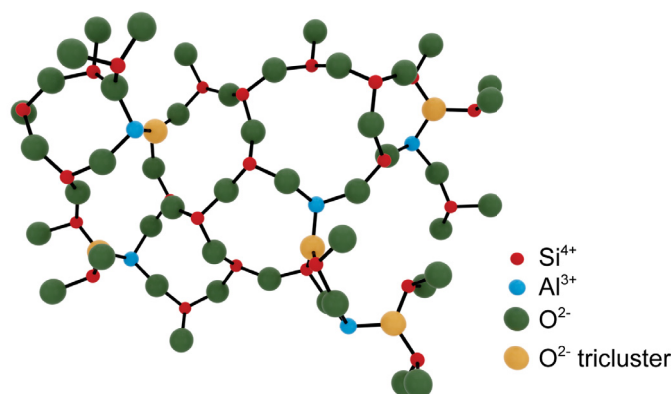


Figure 4.2: Graphical representation of the network topology in a binary aluminosilicate glass based on the assumption that all cations are in fourfold coordination and a certain fraction of oxygen triclusters is present. The  $[\text{SiO}_4]$  and  $[\text{AlO}_4]$  were kept in 2-dimensions to facilitate the view. Reproduced from Ref. [149] under the Creative Commons CC BY License. Rights managed by Springer Nature.

As for the present case, the presence of phase separation was excluded by high-resolution transmission electron microscopy (TEM) down to a length scale of about 5 nm. Also, on microscopic scale, Raman microscopic mapping and polarization microscopy did not reveal any heterogeneity. The following observations of low-frequency Raman scattering, and low-temperature heat capacity are therefore directly resulting from structural heterogeneity at the nanometric length scale. The determined physi-

Table 4.1: Mass density  $\rho$ , refractive index  $n$  at 633 nm, bulk modulus  $K$ , Young’s modulus  $E$ , Poisson ratio  $\nu$ , longitudinal sound velocity  $\nu_L$ , transversal sound velocity  $\nu_T$ , Debye temperature  $\theta_D$  and, Debye frequency  $\omega_D$  of silica and binary aluminosilicate glasses investigated in this study.

<b>Al<sub>2</sub>O<sub>3</sub> (mol%)</b>	<b>0.00</b>	<b>2.05</b>	<b>3.20</b>	<b>7.00</b>
$\rho$ (g/cm <sup>3</sup> )	2.20	2.21	2.22	2.23
$n$	1.458 ( $\pm$ 0.002)	1.461 ( $\pm$ 0.002)	1.465 ( $\pm$ 0.002)	1.479 ( $\pm$ 0.001)
$K$ (GPa)	38.2 ( $\pm$ 1.2)	38.9 ( $\pm$ 1.2)	41.3 ( $\pm$ 1.5)	43.4 ( $\pm$ 1.3)
$E$ (GPa)	73.4 ( $\pm$ 2.3)	75.6 ( $\pm$ 2.4)	77.2 ( $\pm$ 2.8)	79.5 ( $\pm$ 1.3)
$\nu$	0.180 ( $\pm$ 0.010)	0.184 ( $\pm$ 0.011)	0.188 ( $\pm$ 0.013)	0.195 ( $\pm$ 0.011)
$\nu_L$ (ms <sup>-1</sup> )	6017.3 ( $\pm$ 60.1)	6098.2 ( $\pm$ 61.0)	6163.2 ( $\pm$ 61.6)	6272.3 ( $\pm$ 62.7)
$\nu_T$ (ms <sup>-1</sup> )	3758.1 ( $\pm$ 37.6)	3794.4 ( $\pm$ 37.9)	3819.1 ( $\pm$ 38.2)	3859.9 ( $\pm$ 38.6)
$\theta_D$ (K)	498.59	504.72	508.83	514.88
$\omega_D$ (THz)	10.33	10.43	10.60	10.72

cal quantities are given in Table 4.1. The density and the refractive index are linearly increasing with addition of Al<sub>2</sub>O<sub>3</sub> such as the elastic constants.

According to the Debye model, one usually expects a cubic temperature-dependence of the specific heat capacity (Eq. (2.13)). However, experimental studies have shown a deviation from this behavior for most non-crystalline materials. Figure 4.3 (a) displays the specific heat capacity(dQ/dT) at constant pressure of silica and binary aluminosilicate glasses. When  $C_P$  is divided by the relative cubic temperature, the excess of vibration is seen as a “hump” in the region between  $\sim$  2 to 80 K, as shown in Figure 4.3 (b). The Debye contribution  $C_D$  calculated by the Eq. (2.13) is shown in Table 4.1. It is important to note that it was calculated only for one point, i.e., for the sound velocity measured at room temperature at frequency between 8 and 12 MHz. This denotes that Debye’s prediction of the specific heat must follow such Debye levels and any above contribution is the called “excess” of vibrations, or Boson peak.

Prior to the determination of the Boson peak frequency of low-frequency Raman, all data were corrected for air scattering and a constant baseline was subtracted



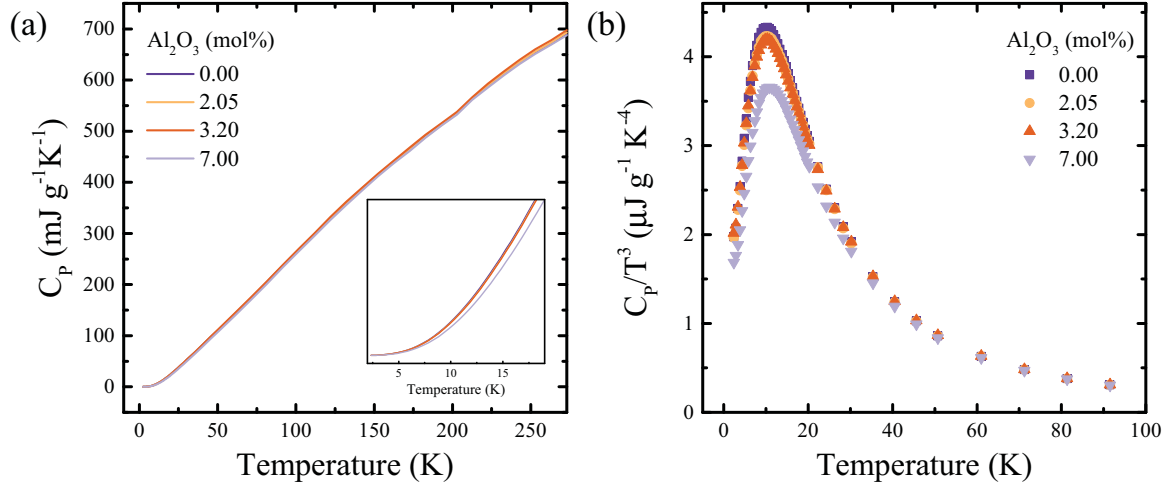


Figure 4.3: (a) The specific heat capacity of silica and aluminosilicate glasses. The inset in (a) is a magnification of the  $C_P$  in the range of 4 - 18 K. (b) The specific heat capacity divided by the cubic temperature, revealing the Boson peak.

individually. In order to compare the intensities of spectra in the low frequency region ( $\omega < 175 \text{ cm}^{-1}$ ) the intensity of all samples was normalized to the area under the band peaking at  $800 \text{ cm}^{-1}$  over the range of  $650 \text{ cm}^{-1} < \omega < 870 \text{ cm}^{-1}$ . This band is related to the bending of silicon inside the tetrahedra cage, that remains practically unchanged with addition of  $\text{Al}_2\text{O}_3$ , within the considered range of compositions.

The measured intensity  $I_{mes}(\omega, T)$  was converted into the reduced Raman intensity through the approach of Shuker and Gammon (Eq. (3.3)) to rule-out the temperature-dependence of the Raman spectra (Figure 4.4 (a)). The density of states was extracted from  $C_P$  data following the Eq. (3.1) and divided by the frequency square to follow the predicted theory that the VDOS is  $g(\omega)$  inversely proportional to  $\omega^2$  (Eq. (2.6)) (Figure 4.4 (b)).

All samples present a clear dependence of the excess vibrational density of states. Moreover, the maximum of this peak,  $\omega_{BP}$ , shifts toward higher frequency and its intensity decreases with increasing  $\text{Al}_2\text{O}_3$  content, according to concentration of alumina in aluminosilicate glasses. For the maximum frequency,  $\omega_{BP}$ , of vitreous silica is found a value of  $\sim 32.2 \text{ cm}^{-1}$ . In the literature it is given a value of  $\sim 33 \text{ cm}^{-1}$  for vitreous silica (Hereaus F-300) [164]. This difference may come from the REPUSIL process, which the pristine has passed by. The values of  $\omega_{BP}$  for VDOS and low-frequency Raman for silica and binary aluminosilicate glasses are shown in Figure

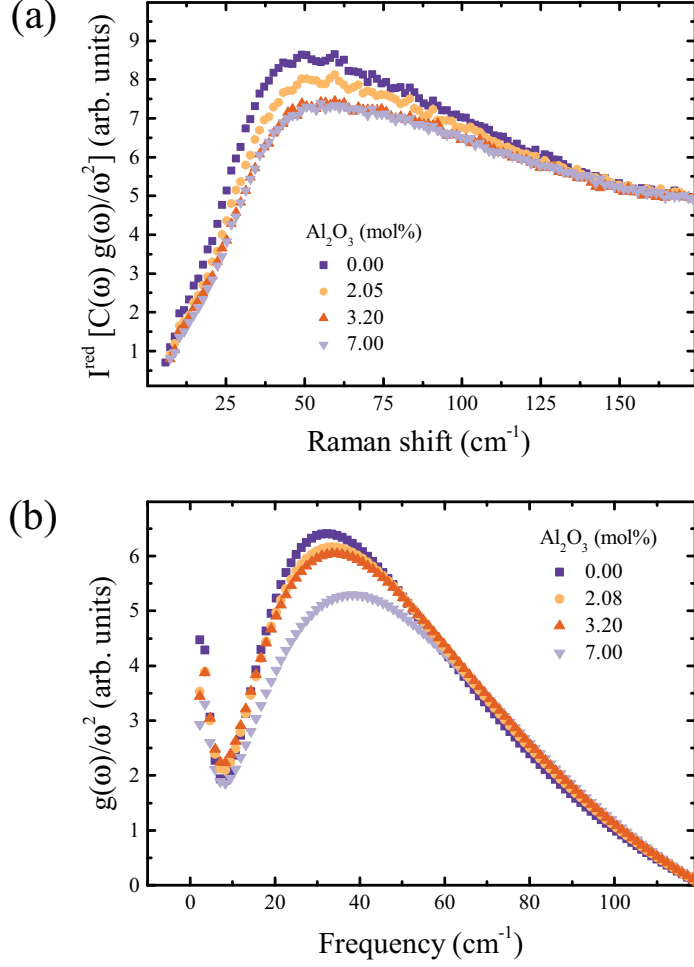


Figure 4.4: (a) Reduced low-frequency Raman spectra of silica and binary aluminosilicate glasses. (b) The VDOS extracted from low-temperature heat capacity for silica and binary aluminosilicate glasses. Adapted from Ref. [149] under the Creative Commons CC BY License. Rights managed by Springer Nature.

4.5.

Similar variations have previously been related to increasing stiffness induced by several parameters, including density [165], pressure [166] or network connectivity [167]. Building on these previous observations, the present trend is explained on the basis of the elastic properties of binary aluminosilicate glasses. Al<sub>2</sub>O<sub>3</sub> acts on the local symmetry of tetrahedral [SiO<sub>4</sub>] stretching motions [168], decreasing the degrees of freedom in the system and increasing stiffness. This reflects in increasing bulk modulus (Table 4.1). Further understanding is derived from the inhomogeneity models explained above. The average size of heterogeneities  $\xi$  have been related in the literature to the position of the Raman Boson peak frequency,  $\omega_{Bp}$ , and transversal

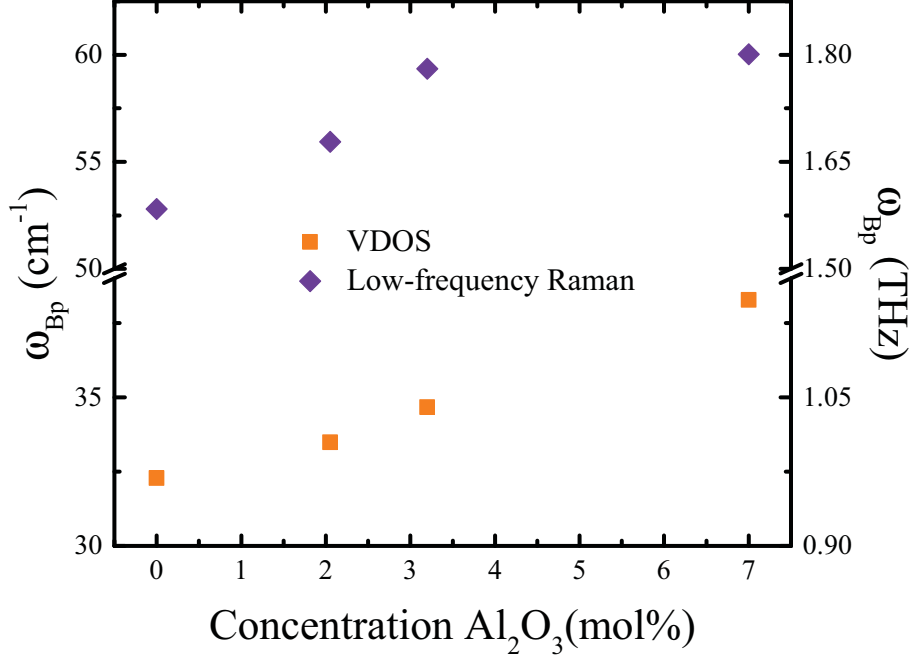


Figure 4.5: Boson peak frequency of low-frequency Raman scattering and VDOS as a function of Al<sub>2</sub>O<sub>3</sub> concentration in binary aluminosilicate glasses. Adapted from Ref. [149] under the Creative Commons CC BY License. Rights managed by Springer Nature.

sound velocity through the relation [169–171]:

$$\xi = S \frac{\nu_T}{\omega_{Bp}} \quad (4.1)$$

here  $S$  is a shape factor. The latter is not easy to be defined due to the difficulty to deduce its shape. Usually it is assumed to be 1 for spherical particles [171, 172]. Figure 4.6 displays the variation of the average length scale of  $\omega_{Bp}$  from VDOS as a function of Al<sub>2</sub>O<sub>3</sub> content, considering  $S=1$ . Clearly, there is a decrease of the average size of heterogeneities  $\xi$  from 3.38 nm in v-SiO<sub>2</sub> (compared to 3.74 nm as reported previously [173]) to 3.36 nm for an alumina content of 7 mol %.

In order to investigate the frequency of the Boson peak with changes in the elastic medium transformation, a Debye corrected representation for  $Bp$  - VDOS is investigated by evaluating the Debye frequency  $\omega_D$  and Debye DOS  $g_D(\omega)$  in terms of longitudinal and transverse sound velocities:

$$\begin{aligned} \omega_D &= k_D \nu_D \\ g_D(\omega) &= \frac{3\omega^2}{\omega_D^3} \end{aligned} \quad (4.2)$$

here,  $k_D$  is Debye cutoff wavevector [174]. If the frequency is normalized by  $\omega/\omega_D$  and

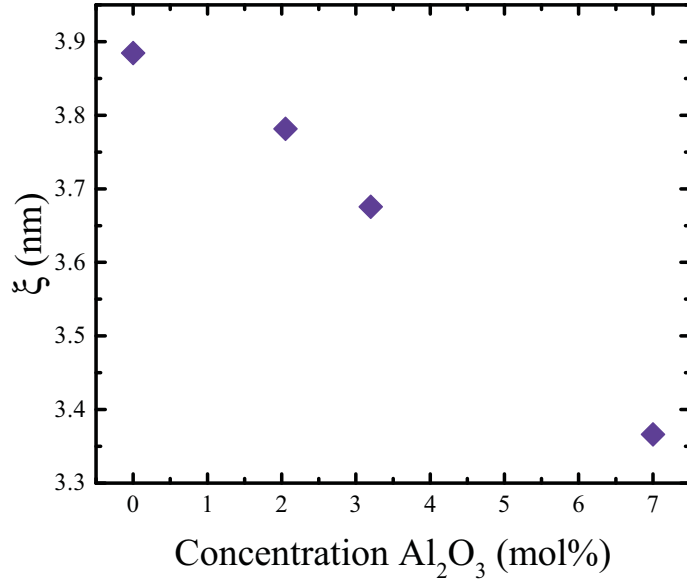


Figure 4.6: Variation of the dynamic correlation length  $\xi$  in silica and binary aluminosilicate glasses as a function of alumina content. Adapted from Ref. [149] under the Creative Commons CC BY License. Rights managed by Springer Nature.

the DOS by  $g(\omega)/g_D(\omega)$ , it should lead to a universal curve if a same material is subjected to external parameters as temperature, pressure or the amount of polarization [123]. The Debye corrected representation for the aluminosilicate glasses investigated in this work is shown in Figure 4.7.

If the disorder is not changed (eg. the topochemical heterogeneity) but just the value of the mean elastic constants or density, this must correspond to elastic-transformation scaling and all data points should fall onto a same curve. In the present case, this is clearly not the case because addition of Al<sub>2</sub>O<sub>3</sub> modifies the glass structure and, consequently, the state of disorder is changed by changing the external conditions [123].

The maximum of the normalized intensity  $[g(\omega)/g_D(\omega)]_{\max}$  and rescaled frequency  $[\omega/\omega_D]_{\max}$  is shown in the inset of Figure 4.7. In general, it follows a tendency of increasing the frequency while the intensity decreases. The correlation length, which refers to the minimum size of the shear fluctuation, is intrinsically related to the frequency and intensity. A smaller value of  $\xi$  leads to a decrease of the  $\omega_{Bp}$  intensity and shifts its position to higher frequencies. Considering the correlation length (shown in Figure 4.6), indeed,  $[g(\omega)/g_D(\omega)]_{\max}$  and  $[\omega/\omega_D]_{\max}$  confirms such behavior. Another factor that influences the position and/or intensity of the  $Bp$  is

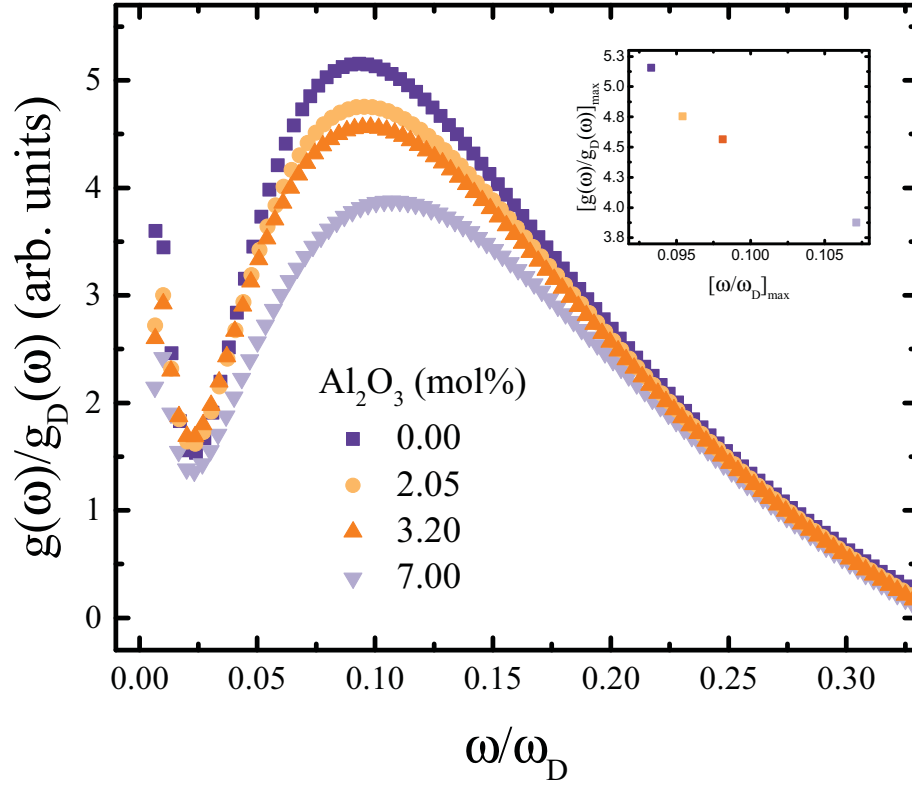


Figure 4.7: Reduced density of states  $g(\omega)/g_D(\omega)$  vs. the rescaled frequency  $\omega/\omega_D$ . Maximum normalized intensity and maximum rescaled frequency is plotted in the inset (top right). Adapted from Ref. [149] under the Creative Commons CC BY License. Rights managed by Springer Nature.

the structural “degree of disorder”. Increasing the “degree of disorder” just leads to an enhancement, while keeping the  $\omega_{Bp}$  position constant [123], which is not the case since the “disorder” seems to decrease almost linearly according to addition of alumina. Furthermore, the scalability shows that the changes are not occurring only in the elastic properties, instead, the addition of  $\text{Al}_2\text{O}_3$  leads to a topochemical heterogeneity of the material.

Even though investigations of the Boson peak have shown that alumina doping leads to a structural homogeneity on molecular scale, the UV-Vis spectra of silica and aluminosilicate glasses shows the influence of topochemical heterogeneity in a more extended picture. Figure 4.8 shows the UV-Vis spectra of silica and aluminosilicate glasses. The inset box, from 175 nm up to 220 nm, shows the absorption related to the Rayleigh scattering (the light is scattered and does not reach the detector, then the equipment interprets it as absorbed light). Interestingly, in this region addition of

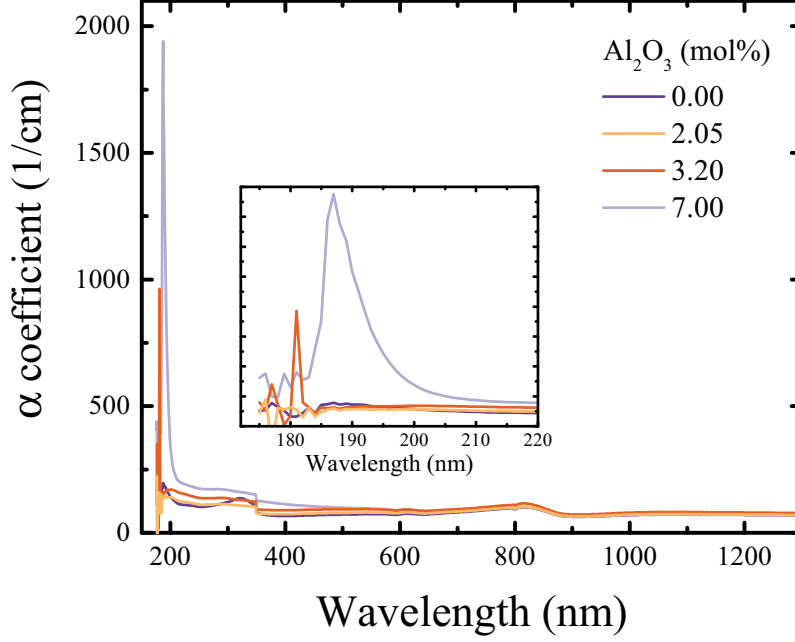


Figure 4.8: UV-Vis spectra of silica and binary aluminosilicate glasses from 175 up to 1350 nm. The inset is a magnification in the range of 175 - 220 nm.

alumina shows a suppression of the Rayleigh scattering, except for 7 mol %  $\text{Al}_2\text{O}_3$ . The relation between Rayleigh scattering and particles size (valid for spherical particles) can be written as the analytic function [175]:

$$\sigma_{Ray} = \frac{8\pi}{3} \left( \frac{2\pi n_{med}}{\lambda} \right)^4 a^6 \left( \frac{m^2 - 1}{m^2 + 2} \right)^2 \quad (4.3)$$

here  $\lambda$  is the vacuum wavelength,  $a$  is the particle radius, and  $m = n_{sph}/n_{med}$  is the ratio of the refractive index of the particle to that surrounding medium. Initially, this suppression may have influence from the size of the heterogeneity, represented by the particle radius in Eq. (4.3). In this context, a study from Champagnon et al. confirms that the decrease of the heterogeneity is accompanied by decreasing optical loss of the glass due to decreasing the Rayleigh scattering [16]. Furthermore, the  $[\text{AlO}_4]$  tetrahedra in tricluster configuration is “distorted” compared to ‘normal’  $[\text{AlO}_4]$  tetrahedra. At a certain alumina concentration, these tricluster centers may bring structural stresses from the inherent states that is manifested by an increasing of the refractive index of the surrounding medium (e.g. higher  $n_{med}$  and lower  $m$ ). The contribution of the latter may be dominant over the average size of the heterogeneity, leading to an increase of the Rayleigh scattering, as depicted by the sample containing 7 mol %  $\text{Al}_2\text{O}_3$  in Figure 4.8.

## 4.2 Ternary aluminoborosilicate glasses

Despite there are several works concerning the  $[\text{SiO}_2 \cdot \text{Al}_2\text{O}_3 \cdot \text{B}_2\text{O}_3]$  (SAB) glass system, its extent of structure, dynamic features and nature of mixing of the network-forming cations (silicon, boron and aluminum) are still not fully understood [176, 177]. Most of these studies include modifiers in their composition due to the difficulty in obtaining homogeneous materials [109, 178–182]. Introduction of modifiers, however, disguise the fundamental chemical topology and heterogeneity of such glass system.

Investigations by NMR reported that inclusion of few amounts of  $\text{Al}_2\text{O}_3$  in borosilicate glasses avoid the formation of tetrahedral  $[\text{BO}_4]$  [177, 181, 183, 184]. In a chemical point of view, this is reasonable, because an excess of oxygen would prefer to conciliate tetrahedral aluminum  $[\text{AlO}_4]^-$  to compensate its deficient charge than a formation of  $[\text{BO}_3]$  to  $[\text{BO}_4]$ .

Following Pauling's rules for ionic crystals [69], the most probable configuration of both,  $[\text{Yb}^{3+}]$  (ionic radius of 0.868 Å) and reduced,  $[\text{Yb}^{2+}]$  (ionic radius of 1.02 Å) must be octahedral (coordination number equals to 6). However, similarly to boron speciation case, without modifiers to donate oxygens the probability that ytterbium ions would increase its coordination number is very low, considering a full polymerized network.

Since there is no oxygen in excess in this glass system, it is expected that the building blocks will be composed fundamentally of trigonal boron-oxygen  $[\text{BO}_3]$ , tetrahedral silicon-oxygen  $[\text{SiO}_4]$  and tetrahedral aluminum-oxygen  $[\text{AlO}_4]$ . Following the same reasoning, ytterbium is also expected to be in its most probable configuration, octahedral ytterbium-oxygen  $[\text{YbO}_6]$ .

The composition investigated in this study is a ternary system  $[(98.4 - x) (\text{SiO}_2) \cdot x (\text{B}_2\text{O}_3) \cdot 1.5 (\text{Al}_2\text{O}_3)]$  glasses, with  $1.25 < x < 9.35$  mol%, doped with a low concentration of 0.1 mol%  $\text{Yb}_2\text{O}_3$ . All samples are, with the naked eye, colorless, except the sample containing 1.40 mol%  $\text{B}_2\text{O}_3$ , that is visible light yellowish and is an indicative of presence of divalent ytterbium ions  $[\text{Yb}^{2+}]$ . A deeper analysis carried by UV-Vis and photoluminescence spectroscopy shows a presence of both, tri- and di-valent, ytterbium ions in all samples. The  $\alpha$  coefficient spectra of ternary glasses are shown in Figure 4.9 (a). The first band reveals a high UV absorption (or Rayleigh

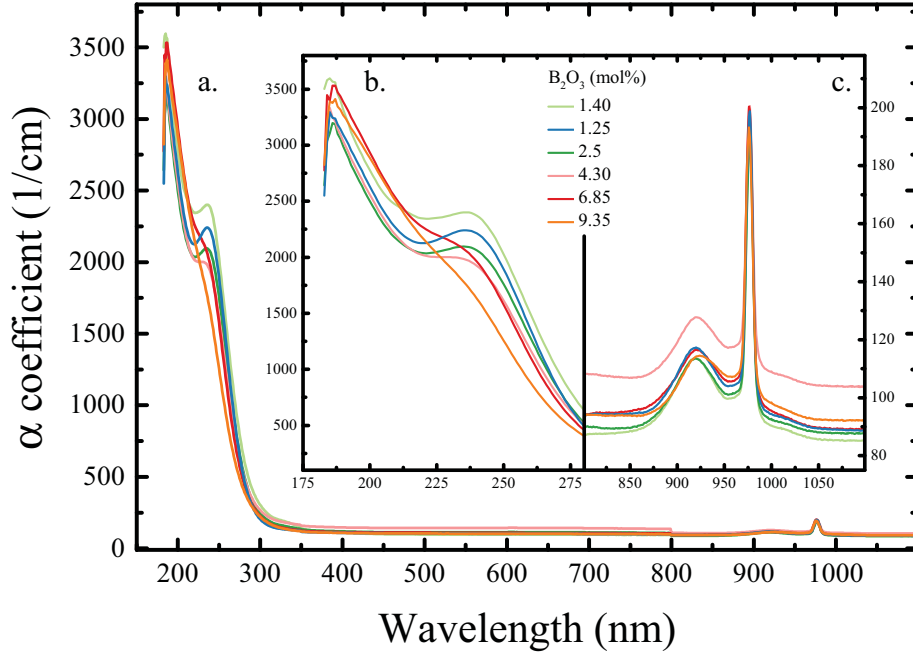
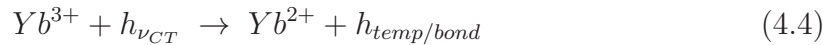


Figure 4.9: (a) General overview of UV-Vis-NIR spectra of ternary aluminoborosilicate glasses. The UV absorption region related to  $[Yb^{2+}]$  is shown in (b) and (c) is related to the absorption peak of  $[Yb^{3+}]$ .

scattering). The strong peak located near at  $\sim 230$  nm is related to charge transfer (CT) absorption band due to the valence instability of the ytterbium ions. This is a typical peak for aluminosilicate glasses doped with ytterbium [185, 186]. A CT transition involves an interaction between the trivalent ytterbium ion and the host lattice and corresponds to the transfer of an electron from a nearby oxygen ligand to the ytterbium ion. This process of  $[Yb^{3+}]$  reduction is given by [187]:



here,  $h_{\nu_{CT}}$  represents the excitation energy to the different CT states and corresponds to a temporarily formed or a bound hole,  $h_{temp/bond}$ , which is left behind on the oxygen ligand. Aluminum is a known effective co-dopant for improving solubility of rare-earth (RE) ions. Addition of aluminum content result in a replacement of  $[RE-O-RE]$  and  $[RE-O-Si]$  by stable  $[RE-O-Al]$  linkages and, in this case, aluminum ions will be attracted to ytterbium- local domains [188]. In aluminosilicate glasses doped with  $[Yb^{3+}]$ , the bound hole is most likely an Al-oxygen hole center (OHC), where the OHC is formed by  $[AlO_4]^\circ$  [189]. The absorption peak below 230 nm (Figure 4.9 (b)) is usually caused by excitation of electrons in oxygen and shifts to more energetic



wavelength with a weakening of the oxygen bond [67]. There is also evidence that the absorption edge in visible/UV region (associated with the CT band) is moved to higher wavelengths as a result of increased electron polarization [190]. Figure 4.9 (c) shows a typical absorption of  $[\text{Yb}^{3+}]$  ( $\sim 915$  and  $975$  nm) and indicate its presence in the glass structure.

Photoluminescence spectra of ternary glasses are shown in Figure 4.10. The Figure 4.10 (a) shows the excitation spectra of  $[\text{Yb}^{2+}]$  ions in  $[\text{Yb}^{3+}]$ -doped ternary glasses. The three bands at approximately 300, 325, and 400 nm are characteristic of the excitation spectra and correspond to the  $4f^{14} - 4f^{13} 5d$  transitions of  $\text{Yb}^{2+}$  [186]. The Figure 4.10 (b) shows the emission bands of  $[\text{Yb}^{2+}]$  under 240 nm excitation and has a maximum at approximately 525 nm. This broad band is assigned to the  $4f 5d - 4f$  transitions of  $[\text{Yb}^{2+}]$  [186] and to  $[\text{AlO}_4]^\circ$  centers [191]. As expected, the sample visible yellow (1.40 mol %  $\text{B}_2\text{O}_3$ ) presents the highest intensity. The Figure 4.10 (c) shows the typical spectra of  $\text{Yb}^{3+}$  emission ( ${}^2\text{F}_{5/2} \rightarrow {}^2\text{F}_{7/2}$ ), with two emission peaks at 975 and 1020 nm [191].

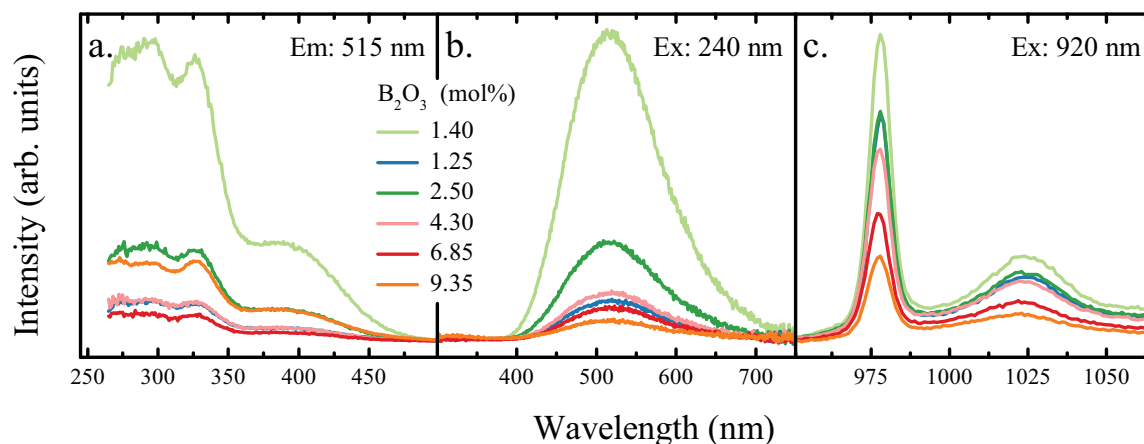


Figure 4.10: Photoluminescence spectra of ternary samples. (a) Excitation spectra of  $\text{Yb}^{2+}$  ions by emission at 515 nm. (b) Emission spectra of  $\text{Yb}^{2+}$  and  $[\text{AlO}_4]^\circ$  centers by excitation at 240 nm. (c) Emission spectra of  $\text{Yb}^{3+}$  by excitation at 920 nm.

Impurities of chlorine and water content were present in the samples with average concentrations of less than 0.06 mol % ( $\text{SiCl}_4$ ) (determined by WD-EPMA) and  $< 10$  ppm (OH, determined by infrared optical spectroscopy), respectively.

The determined physical properties are given in Table 4.2. The density and the refractive index are linearly decreasing with addition of  $\text{B}_2\text{O}_3$  such as the elastic

constants. The Poisson's ratio and free volume increases with addition of  $B_2O_3$ .

Table 4.2: Mass density  $\rho$ , refractive index at 633 nm  $n$ , Young's modulus  $E$ , longitudinal modulus  $L$ , shear modulus  $G$ , bulk modulus  $K$ , Poisson ratio  $\nu$  and, molar free volume  $V_f$  of ternary aluminoborosilicate glasses investigated in this study.

$\text{B}_2\text{O}_3$ (mol%)	$\rho$ (g/cm <sup>3</sup> )	$n$	$E$ (GPa)	$L$ (GPa)	$G$ (GPa)	$K$ (GPa)	$\nu$	$V_f$ (cm <sup>3</sup> )
1.25	2.216 ( $\pm 5.7 \times 10^{-3}$ )	1.4613 ( $\pm 1.0 \times 10^{-4}$ )	73.3 ( $\pm 0.9$ )	79.8 ( $\pm 0.6$ )	31.0 ( $\pm 0.2$ )	38.4 ( $\pm 0.5$ )	0.182	14.95
1.40	2.217 ( $\pm 1.7 \times 10^{-3}$ )	1.4618 ( $\pm 4.5 \times 10^{-5}$ )	73.3 ( $\pm 1.5$ )	79.7 ( $\pm 0.9$ )	31.0 ( $\pm 0.3$ )	38.4 ( $\pm 0.8$ )	0.182	14.94
2.50	2.211 ( $\pm 2.7 \times 10^{-3}$ )	1.4608 ( $\pm 7.1 \times 10^{-5}$ )	71.4 ( $\pm 1.0$ )	77.7 ( $\pm 0.6$ )	30.2 ( $\pm 0.2$ )	37.5 ( $\pm 0.5$ )	0.183	14.99
4.30	2.195 ( $\pm 3.5 \times 10^{-3}$ )	1.4602 ( $\pm 1.6 \times 10^{-4}$ )	67.3 ( $\pm 1.1$ )	73.8 ( $\pm 0.6$ )	28.3 ( $\pm 0.2$ )	36.1 ( $\pm 0.6$ )	0.190	15.16
6.85	2.178 ( $\pm 3.9 \times 10^{-3}$ )	1.4595 ( $\pm 1.2 \times 10^{-4}$ )	62.2 ( $\pm 1.0$ )	68.9 ( $\pm 0.6$ )	26.0 ( $\pm 0.2$ )	34.3 ( $\pm 0.6$ )	0.198	15.33
9.35	2.154 ( $\pm 7.3 \times 10^{-4}$ )	1.4588 ( $\pm 3.5 \times 10^{-4}$ )	57.5 ( $\pm 0.6$ )	64.6 ( $\pm 0.4$ )	23.8 ( $\pm 0.1$ )	32.9 ( $\pm 0.3$ )	0.209	15.61

Regarding the present ternary glass series, only from the trend of the physical quantities,  $B_2O_3$  seems to be mainly incorporated inside the silica matrix as trigonal units ( $[BO_3]$  triangles), because tetrahedral  $[BO_4]$  is considerably denser than the  $[SiO_4]$  tetrahedron [192] and the lower packing density of  $[BO_3]$  units causes a decrease in mass density [193] (see Table 4.2). A lower coordination number also implies in a less dense packing of the glass structure and consequently to a lower refractive index [176] (see Table 4.2). The hardness and strain-rate sensitivity are shown in Figure 4.11. While hardness decreases linearly with  $B_2O_3$  addition, the strain-rate sensitivity shows two different regimes, suggesting that a structural difference may occur between 2.5 and 4.3 mol %  $B_2O_3$ .

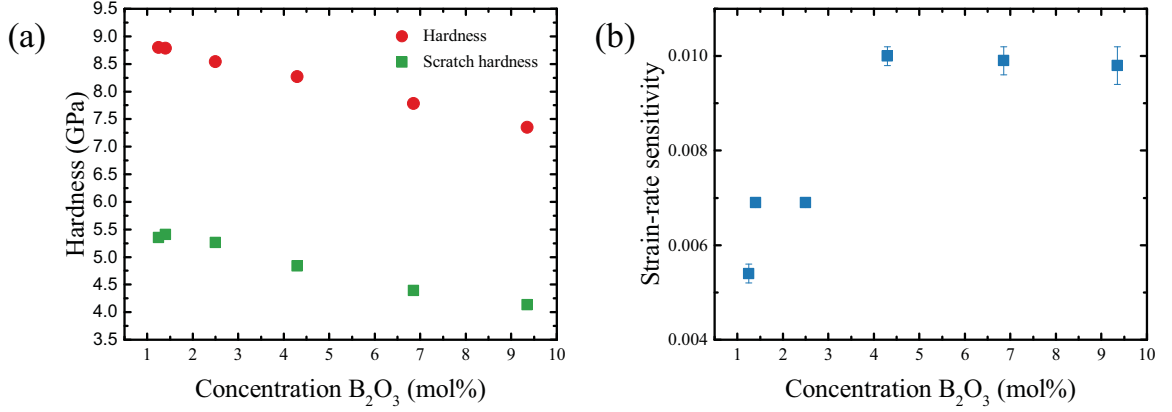


Figure 4.11: Hardness and scratch hardness (a) and strain-rate sensitivity (b) of aluminoborosilicate glasses.

In the present work, the theoretical optical basicity ( $\Lambda_{th}$ ) was calculated by [194]:

$$\Lambda_{th} = \sum x_i A_i \quad (4.5)$$

here,  $x_i$  are the equivalent fraction of the oxides and  $A_i$  are the optical basicity values of the constituent oxides. The values adopted of  $A_i$  for the glass system are:  $Yb_2O_3 = 0.89$  [195],  $Al_2O_3 = 0.60$  [194],  $SiO_2 = 0.48$  [194] and,  $B_2O_3 = 0.42$  [194]. The values follow the sequence  $Yb_2O_3 > Al_2O_3 > SiO_2 > B_2O_3$  and refer to a decreasing capacity to donate electrons, i.e., from a basic characteristic to acid. From Figure 4.12, it is clear to see that glasses  $[98.4 (SiO_2) \cdot 1.5 (Al_2O_3) \cdot 0.1 (Yb_2O_3)]$  increase the optical basicity ( $\Lambda = 0.4824$ , represented by a blue dashed-dot line) related to pure  $SiO_2$  ( $\Lambda_{SiO_2} = 0.48$ , represented by a black dashed line), whereas  $[(99.9 - x) (SiO_2) \cdot x (B_2O_3) \cdot 0.1 (Yb_2O_3)]$  presents an opposite behavior. The latter is because

$B_2O_3$  has a lower polarizability and optical basicity than that of the other oxides in the glass matrix [196]. Thus, continuous addition of  $B_2O_3$  to the glass means that the oxide ions are losing the ability to transfer electrons.

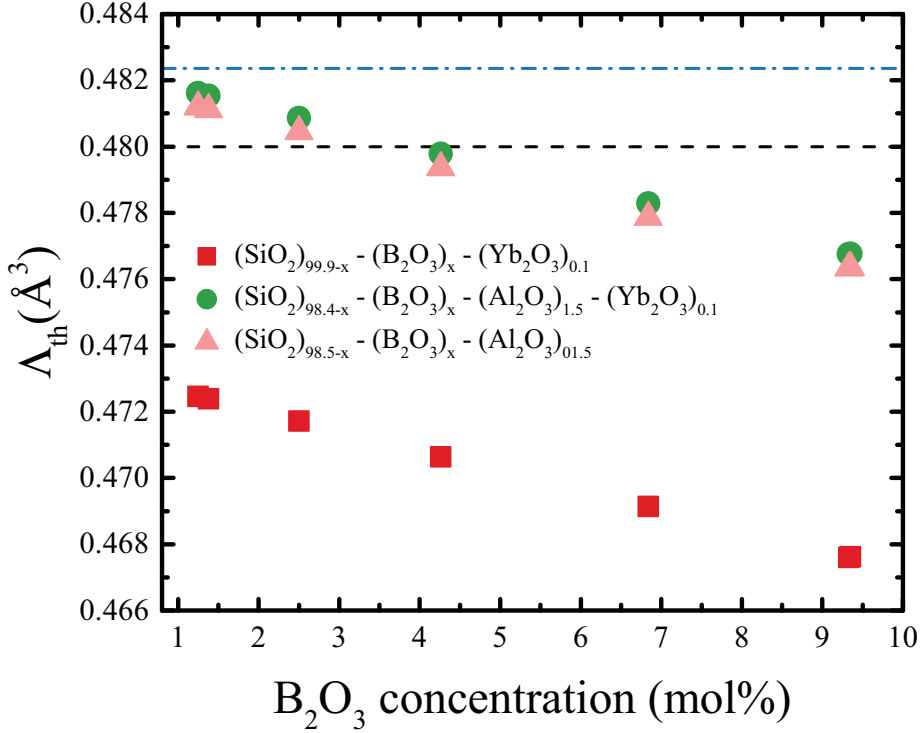


Figure 4.12: Optical basicity of  $[(SiO_2) \cdot (Al_2O_3) \cdot (B_2O_3) \cdot (Yb_2O_3)]$  glass system. Green circles are the optical basicity calculated for the glass systems studied in this work. Pink triangles are the aluminoborosilicate glasses without  $Yb_2O_3$  and, the red squares are the optical basicity of borosilicate glasses doped with  $Yb_2O_3$ . The black dashed line located at  $0.48 \text{ \AA}^3$  and the blue dashed-dot line at  $0.4824 \text{ \AA}^3$  is a reference of the optical basicity of pure  $SiO_2$  glass and  $Al_2O_3$  in silica matrix  $[98.4 (SiO_2) \cdot 1.5 (Al_2O_3) \cdot 0.1 (Yb_2O_3)]$ , respectively.

It is very important to note, however, that even small amounts of  $Al_2O_3$  are capable to improve the compatibility of the system by keeping the charges closer to the  $SiO_2$  level, that is the majority component. Here, the sample containing 4.3 mol%  $B_2O_3$  is expected to be the most structurally stable system (charge neutrality), because its optical basicity is very close to the  $SiO_2$  matrix. The optical basicity can be extended to evaluate the polarizability of the oxide glasses. Electronic polarizability of the material is the magnitude of electrons responding to an electric field [197],  $\alpha_m$ , and

can be calculated following the equation [198]:

$$\alpha_m = \frac{3}{4\pi N_A} R_m = \frac{3V_m}{4\pi N_A} \left[ \frac{(n_0^2 - 1)}{(n_0^2 + 2)} \right] \quad (4.6)$$

here,  $V_m$  is the molar volume,  $N_A$  is the Avogadro constant,  $R_m$  the molar fraction and,  $n_0$  the linear refractive index. On the other hand, the oxide ion polarizability,  $\alpha_O^{2-}$ , is calculated through the relation:

$$\alpha_O^{2-} = (\alpha_m - p\alpha_i) / q \quad (4.7)$$

$p$  and  $q$  refer to the number of atoms assuming a simple oxide with common formula  $A_pO_q$  and  $\alpha_i$  is the molar cation polarizability. In the case of binary or ternary system, the  $\alpha_i$  can be calculated considering the average,  $\Sigma\alpha_I = X_i p_i \alpha_i(i)$ , where  $X_i$  is the concentration (mol%) of the system  $i$  and  $\alpha_I(i)$  is the molar cation polarizability for each system  $i$  [199]. In this work, the latter values were taken from [200]. The Figure 4.13 shows the electronic polarizability of the material,  $\alpha_m$ , and of the oxide ion,  $\alpha_O^{2-}$ . The  $\alpha_m$  increases with  $B_2O_3$  addition, indicating that the electronic clouds in the structure are becoming easier to be deformed [201]. Differently,  $\alpha_O^{2-}$  shows a particular mode, whereas a lower value means that the ability of oxide ions to transfer electrons to the surrounding cations is becoming weaker [196]. Both results are in accordance with majority presence of  $[BO_3]$  units, where the  $\sigma$ -covalent bonding dramatically reduces the polarizability of the oxide atoms by tightening effect, while the oxide atom still has a residual tendency to donate electrons (that is its basicity) [93].

In order to explore the character of the bonds with increasing  $BO_3$  content, Yamashita and Kurosawa model was applied [202]. This model proposes a general theory of the dielectric constant of simple ionic crystals based on quantum mechanical treatment of the structure of constituent ions. Dimitrov and Komatsu have adapted this model to glasses for oxide compounds [200] and it gives the interaction parameter,  $A$ , which the physical meaning relates to the charge overlap between neighboring ions:

$$A = [(\alpha_f^- - \alpha_O^{2-})] / [2(\alpha_i + \alpha_f^-)(\alpha_i + \alpha_O^{2-})] \quad (4.8)$$

where  $\alpha_f^-$  is the Pauling's value of  $3.921 \text{ \AA}^3$  and  $\alpha_O^{2-}$  and  $\alpha_i$  are the same used in Eq. (4.7). Chemically, it represents the interionic interaction between 2p-electron cloud of the oxide ion and the valence cloud of the cation in respect to form a chemical bond.

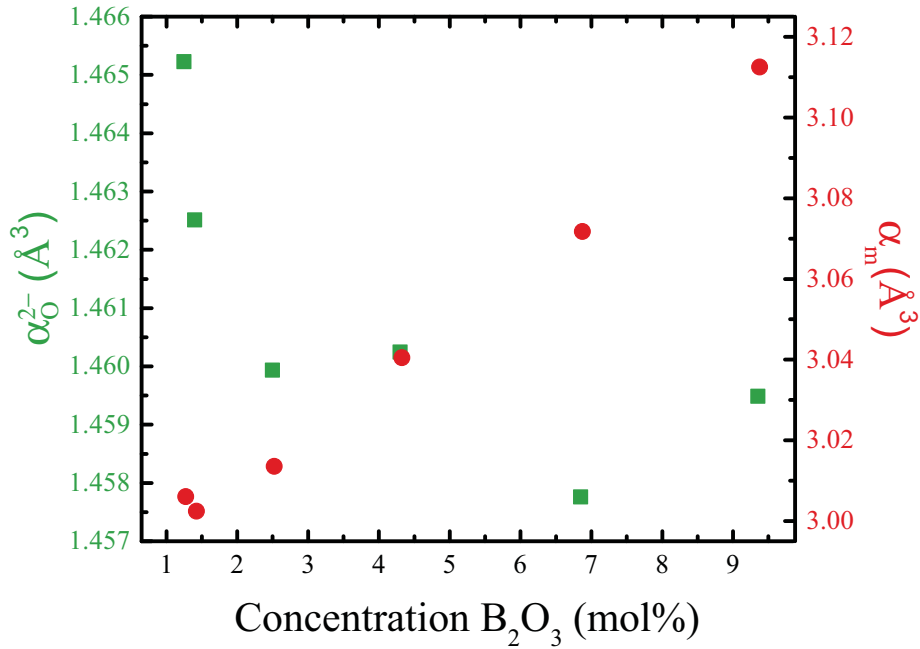


Figure 4.13: The oxide ion electronic polarizability (left side, green squares) and the electronic polarizability (right side, red circles).

The values of the interaction parameter are given in Table 2. It tends to increase with increasing B<sub>2</sub>O<sub>3</sub> content (not linearly), meaning participation of an averaged oxide ion in a more covalent bond character, due to a more shared electron density [199, 200, 203].

Raman scattering spectra of all samples after total area normalization (from 200 to 1450 cm<sup>-1</sup>) are shown in Figure 4.14 (a). The band shape is quite similar for all glasses. The most notable change is related to the main band ( $\sim 440$  cm<sup>-1</sup>), with a pronounced reduction of intensity for samples containing 1.25, 1.40 and 2.5 mol % B<sub>2</sub>O<sub>3</sub> in respective to the other compositions. The rather sharp signals *D1*  $\sim 490$  cm<sup>-1</sup> and *D2*  $\sim 600$  cm<sup>-1</sup> become less prominent with B<sub>2</sub>O<sub>3</sub> addition. A strong band located at  $\sim 935$  cm<sup>-1</sup> and a weaker one located at 1365 cm<sup>-1</sup> appear. Additionally, a very broad band arises around 688 cm<sup>-1</sup>.

Normalized Fourier-transform infrared spectra (FTIR) of the ternary glass series and silica are shown in Figure 4.14 (b). All glasses exhibit similar band shape, dominated by the characteristic vibrations of vitreous silica: between 800 - 900 cm<sup>-1</sup> for bending and around 1050 cm<sup>-1</sup> to 1300 cm<sup>-1</sup> for stretching vibrations of the silica network [157]. The bandwidths of the 1000 cm<sup>-1</sup> band have been related to the organization of the silicon network in gel: the smaller the bandwidth the more regular

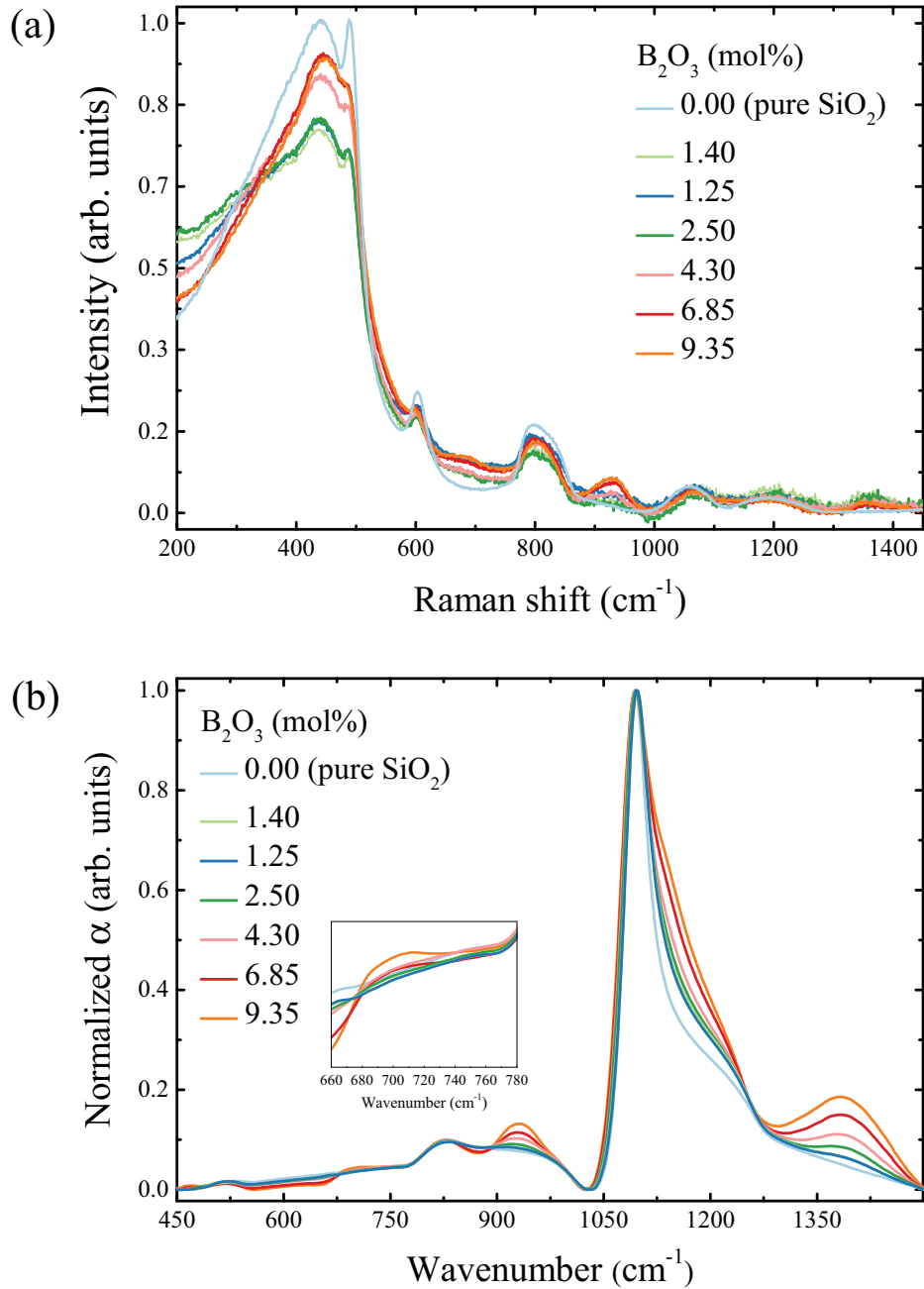


Figure 4.14: Raman scattering spectra (a) and normalized absorption coefficient scattering spectra (FTIR) (b) of aluminoborosilicate glasses. The inset in (b) is a zoom-in of the spectra in the region between 660 and 780 cm<sup>-1</sup> and shows an appearance of B-O-B bond bending for B<sub>2</sub>O<sub>3</sub> concentration higher than 6.85 mol%. The silica glass is shown only for reference.

the silicon network [204]. Two prominent bands emerge at around 932 and 1385 cm<sup>-1</sup> and another band starts to appear at around 1115 cm<sup>-1</sup>. There is also one small band around 700 cm<sup>-1</sup> that is evident only for concentrations higher than 6.85 mol% B<sub>2</sub>O<sub>3</sub>. The latter is attributed to [B-O-B] bond bending vibrations [110, 205–207]. The band



that appears around  $1115\text{ cm}^{-1}$  is related to mixed [Si-O-B] bonds [206]. The bands at  $\sim 932$  and  $\sim 1385\text{ cm}^{-1}$  are usually related to B-O-Si linkages [205, 208] and neutral charged  $[\text{BO}_3]$  triangles [205–207], respectively.

Raman spectra lack of the characteristic signals from boroxol rings at  $\sim 806\text{ cm}^{-1}$  [209]. For  $\text{B}_2\text{O}_3$  concentrations higher than 6.85 mol %, FTIR spectra indicate the presence of direct [B-O-B] linkages, as highlighted in the inset plot. As shown in Table 4.3, the integrated area of both [Si-O-B] stretching bands (at  $\sim 932$  and  $\sim 1385\text{ cm}^{-1}$ ) show a linear increase with addition of  $\text{B}_2\text{O}_3$  and therefore, the borate must be mainly incorporated as isolated, triangular  $[\text{BO}_3]$  entities.

The decrease of the integrated Raman intensity of the main band corresponds to a decrease in connectivity of the glass network [210], which is expected, since tetrahedral  $[\text{SiO}_4]$  are being replaced by triangular  $[\text{BO}_3]$ . The *D1* and *D2* Raman bands are related to breathing motions of oxygens atoms in very symmetric four- and three-membered rings of  $[\text{SiO}_4]$ , respectively [76]. The reduction in intensity with systematic addition of a competing network former means that the population of small rings decreases, with [Si-O-Si] bonds being replaced by a structure containing other species (substitution or rearrangement into larger rings). NMR investigations of borosilicate glasses confirmed a more broadly distributed bond angle between  $[\text{BO}_3]$ -O-Si/B, and thus less symmetric sites and increased structural disorder around such regions [91]. The FTIR spectra also indicates a reorganization of the silicon network by enlarging the width of the bands.

It is very important to note that until here, it has been presented only the most common kind of characterization of glasses. All vibrational spectroscopies and physical measurements, except of strain-rate sensitivity and oxide ion polarizability, point to a linear behavior regarding the addition of  $\text{B}_2\text{O}_3$ , what could, in principle, mislead the structural interpretation to a homogeneous distribution of boron atoms in the glassy network. However, when topological heterogeneity is considered from vibrational density of states and activation energy of ionic conductivity, the glass network reveals a different story.

Before discussing the results, it is valid to briefly introduce a literature review about the short-range structure, mixing of network forming species of aluminoborate glasses and affinity between boron and aluminum atoms.

From the previous chapter (Chap. 4.1), it is already expected that without further charge compensation (e.g. by the Ytterbium ion and  $[\text{AlO}_4]$  in tetrahedral configuration), one oxygen will be incited to bridge with three other elements instead of two. This oxygen is known as oxygen tricluster [94, 103, 104, 162]. A NMR spectroscopy investigation made by Deters et al., on yttrium aluminum borate glasses  $[0.2 (\text{Y}_2\text{O}_3) \cdot x (\text{Al}_2\text{O}_3) \cdot (0.8 - x)(\text{B}_2\text{O}_3); 0.15 \leq x \leq 0.40 \text{ (mol \%)}]$  has shown that any aluminum species (4, 5 and 6) are intimately interacting with borate groups [211]. It is important to note that at high rare-earth concentration (more than 0.5 mol % in sodium aluminoborosilicate network), such ions are preferably inserted as network modifier into the glassy network [212]. Naturally, the ternary aluminoborosilicate system has a lower amount of  $\text{Yb}_2\text{O}_3$  (0.1 mol %) than 0.5 mol %, but it suggests that ytterbium may introduce additional oxygen ions to the system. Another NMR investigation on sodium aluminoborate glasses at several proportions of  $\text{Na}_2\text{O}$  (varying between 25 to 55 mol %),  $\text{B}_2\text{O}_3$  (varying between 30 to 55 mol %) and  $\text{Al}_2\text{O}_3$  (varying between 10 to 30 mol %) made by Bertmer et al. also has shown that aluminum will be bonded to as many  $[\text{BO}_3]$  units as possible [213]. Moreover, the  $[\text{BO}_3 - \text{O} - \text{AlO}_4]$  bond is very stable [181]. Upon crystallization of aluminoborosilicate glasses,  $\text{Al}_4\text{B}_2\text{O}_9$  and  $\text{Al}_{20}\text{B}_4\text{O}_{36}$  can be found [214], giving a strong evidence of their initial atomic link preferences within the glass.

Both works from Bertmer et al. and Deters et al. have described a correlation of the heteronuclear dipolar second moments  $M_2(^{27}\text{Al} - ^{11}\text{B})$  measured by  $^{27}\text{Al}^{11}\text{B}$ -REDOR and  $M_2(^{11}\text{B} - ^{27}\text{Al})$  measured from  $^{11}\text{B}^{27}\text{Al}$ -REDOR. They have found two different dependencies for B/Al ratio lower and higher than  $\sim 2 - 3$  (B/Al ratio of the present work is shown in Table 4.3). For B/Al ratio higher than  $\sim 2.5$ , both three- and four-coordinated boron species showed a linear dependency, while for lower ratios, the three-coordinated boron indicated a saturation of the number of aluminum atoms in their vicinity. And vice versa aluminum sites suggested a saturation in boron atoms. In the present sample series, this transition should occur between 2.5, correspondent to 4.3 mol %  $\text{B}_2\text{O}_3$ .

The work of Deters et al., particularly, affords a conception of the short-range structure on the yttrium sites. Similarly, ytterbium will have comparable behavior as yttrium in ternary aluminoborosilicate glasses. They have shown that oxygen-

tricluster, proceeding from  $[\text{AlO}_4]$ , coordinated to one yttrium ion and two four-coordinated trivalent species ( $\text{B}^{3+}$  and/or  $\text{Al}^{3+}$ ) seems quite favorable from the bond valence considerations [211]. According to these findings related to literature, NMR works on aluminoborosilicate glasses [177, 181–183, 213] and on yttrium aluminum borate glasses [211, 215], an image of the short-range structure of the present aluminoborosilicate glass series could be depicted and is represented in Figure 4.15

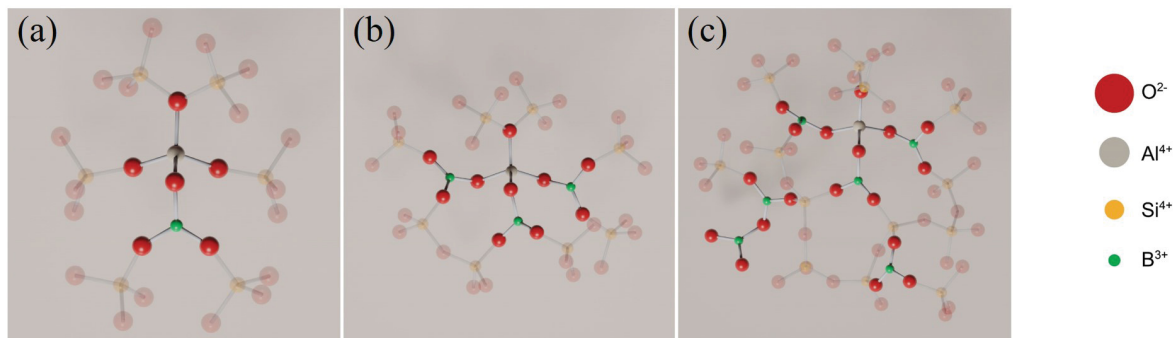


Figure 4.15: Graphical representation of aluminum sites in aluminoborate glasses. (a) shows the aluminum site configuration for a B/Al ratio  $< 1.67$ , (b) for B/Al ratio  $= 2.87$  and (c) for B/Al ratio  $> 2.87$ .

Trigonal coordinated boron will preferably coordinate to alumina. Moreover, both boron and aluminum contribute to the medium range environment of the ytterbium ions. It is expected that boron firstly links to the  $[\text{YbO}][\text{AlO}_4]$  sites within the fourth coordination shell (up to  $\sim 1.5 \text{ mol}\% \text{ B}_2\text{O}_3$ ) (Figure 4.15 (a)) and secondly to isolated alumina sites having tricluster oxygen within the silica network (up to  $\sim 5.1 \text{ mol}\% \text{ B}_2\text{O}_3$ ) (Figure 4.15 (b)). Once all such sites are saturated, any additional boron must, in principle, solely coordinate with silica or other boron (e.g. around  $[\text{YbO}][\text{AlO}_4][\text{BO}_3]$  or  $[\text{AlO}_4][\text{BO}_3]$  regions) (Figure 4.15 (c)).

Table 4.3: Normalized FTIR integrated area at 932 and 1385  $\text{cm}^{-1}$ , Debye contribution  $C_{Debye}$ , longitudinal sound velocity  $\nu_L$ , transversal sound velocity  $\nu_T$ , B/Al ratio and interaction parameter  $A$  of ternary aluminoborosilicate glasses investigated in this study.

$\text{Al}_2\text{O}_3$ (mol%)	FTIR		FTIR		$\nu_L$ (m/s)	$\nu_T$ (m/s)	B/Al ratio	A ( $\text{\AA}$ )
	integrated area (932 $\text{cm}^{-1}$ )	integrated area (1385 $\text{cm}^{-1}$ )	$C_{Debye}$ ( $\mu\text{J g}^{-1}\text{K}^{-4}$ )	integrated area				
1.25	1.05	1.00	0.788		6000 ( $\pm 16$ )	3741 ( $\pm 7$ )	0.83	0.2071
1.40	1.00	1.00	0.787		5996 ( $\pm 16$ )	3739 ( $\pm 7$ )	0.93	0.2077
2.50	1.16	1.12	0.820		5928 ( $\pm 16$ )	3694 ( $\pm 7$ )	1.67	0.2084
4.30	1.40	1.32	0.899		5798 ( $\pm 15$ )	3588 ( $\pm 7$ )	2.87	0.2084
6.85	1.68	1.67	1.015		5623 ( $\pm 14$ )	3452 ( $\pm 6$ )	4.57	0.2091
9.35	2.00	2.00	1.148		5474 ( $\pm 13$ )	3322 ( $\pm 6$ )	6.23	0.2087

Investigations of low-frequency Raman, low-temperature specific heat and THZ-TDS and their interaction with acoustic waves bring complementary information about the topology and intermediate range order of glasses [60]. The reduced low-frequency Raman spectra ( $I^{red}$ ), heat capacity at low-temperatures ( $C_P/T^3$ ), VDOS ( $g(\omega)/\omega^2$ ) extracted from specific heat data, and THZ-TDS ( $\alpha/\nu^2$ ) of aluminoborosilicate glasses are shown in Figure 4.16 (a), (b), (c) and (d), respectively.

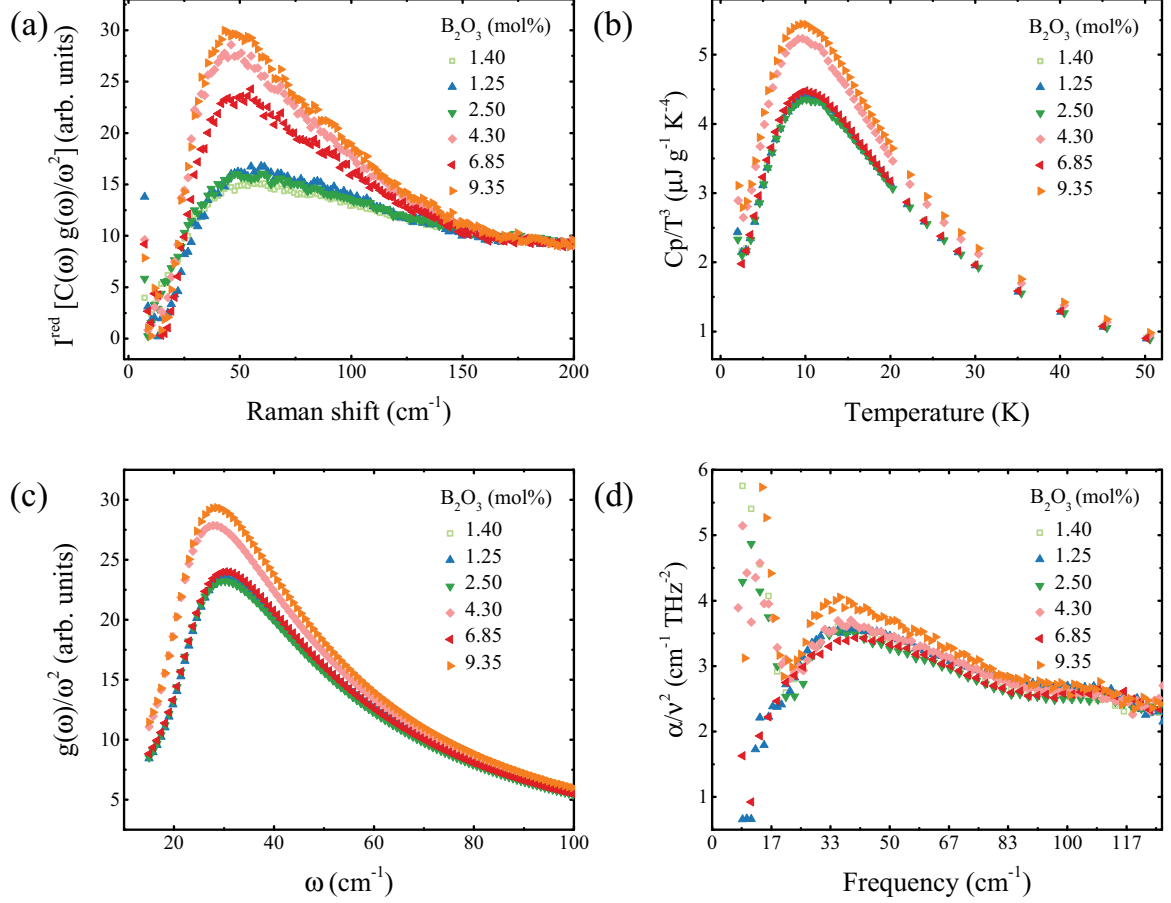


Figure 4.16: Boson peak of (a) Raman low-frequency spectra, (b) specific heat at low-temperature, (c) VDOS normalized over the frequency square as obtained by extraction from specific heat data and, (d) THZ-TDS of aluminoborosilicate glasses.

All samples exhibit a broad asymmetric hump over the Debye contribution (see Debye contribution's value in Table 4.3). The maximum frequency,  $\omega_{Bp}$ , of low-frequency Raman, VDOS extracted from  $C_P$  data and THZ-TDS, follow the same behavior, as shown in Figure 4.17. It has been reported that the  $\omega_{Bp}$  shifts to lower frequencies when the glass becomes less stiff [64, 216], and/or when occur reduction of network connectivity [210]. Recently, it has also been shown that when the bond

directionality increases, the Boson peak shifts to higher frequencies [217].

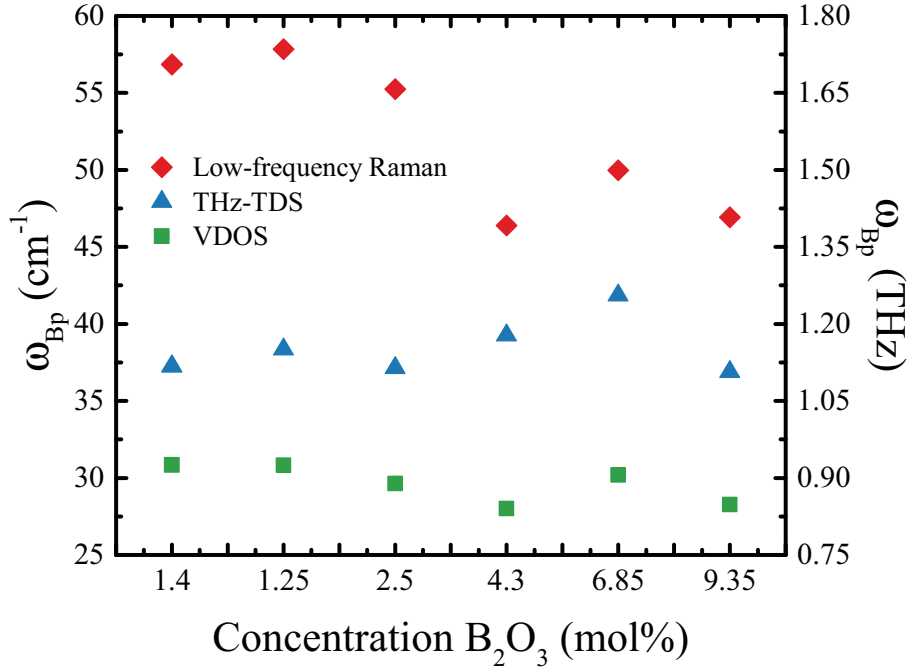


Figure 4.17: The  $\omega_{\text{Bp}}$  from low-frequency Raman (red diamonds), THz-TDS (blue triangles) and VDOS  $g(\omega)/\omega^2$  extracted from low-temperature  $C_P$  (green squares) for aluminoborosilicate glasses.

The average size of heterogeneities  $\xi$  (assuming  $S=1$  in Eq. (4.1)) is shown in Figure 4.18. An increase of the average size of elastic heterogeneities  $\xi$  for the sample containing up to 4.3 mol% B<sub>2</sub>O<sub>3</sub> followed by a strong decrease for the sample containing 6.85 mol% B<sub>2</sub>O<sub>3</sub> is observed. The size of the correlation length for the sample containing 9.35 mol% B<sub>2</sub>O<sub>3</sub> increases back onto the same level as for very low B<sub>2</sub>O<sub>3</sub> concentrations. This reveals that the structure of aluminoborosilicate glasses, especially for borate concentrations twice or three times the molar concentration of alumina, is not simple and major changes not only occur in the short range but also in a more extended intermediate-range structural arrangement. The size of correlated domains is expected to be larger for more open structures than for more densely packed structures [169]. This seems to be evident that the size of the correlation length strongly increases as soon as boron has saturated almost all available Al-sites at around 4.3 mol% and has to start to disrupt the silicon network to form a more open structure. The abrupt decrease on the  $\xi$  for 6.85 mol% B<sub>2</sub>O<sub>3</sub> challenges any explanation. However, above such concentration boron will be forced to coordinate

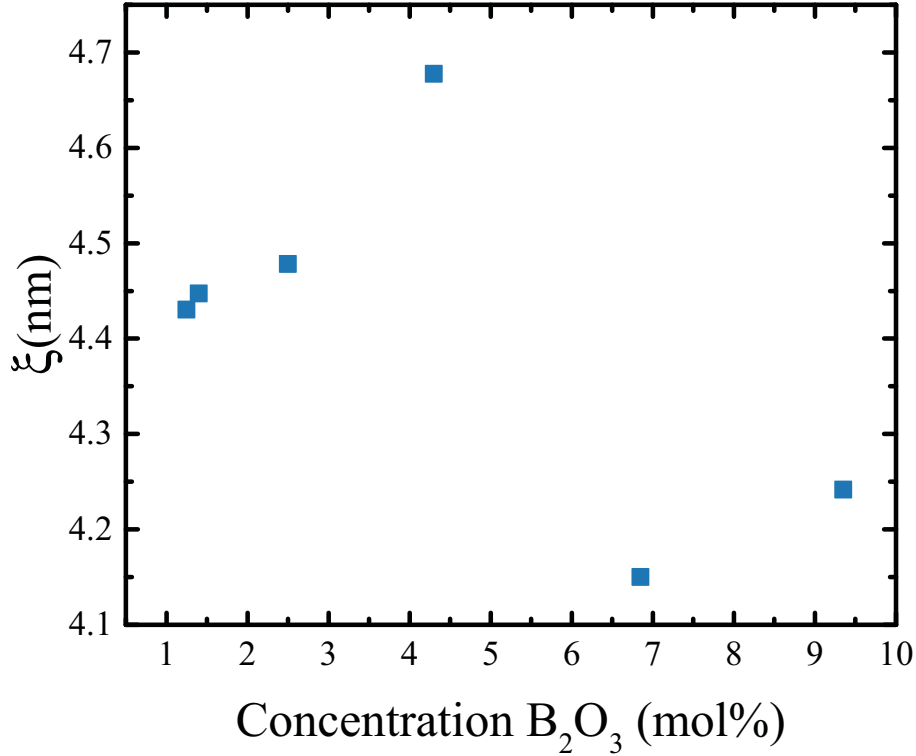


Figure 4.18: Average correlation length of aluminoborosilicate glasses.

with silica, bringing a more broadly distributed bond angle between B-O-Si/B due to lower symmetry of these sites [91]. These two sites (aluminum and boron sites) will compress silica regions, narrowing the distribution of their bond angles (Si-O-Si). Additionally, two distinct regions will be present in the glass network, aluminum sites and B-O-Si/B regions. For the glass containing 9.35 mol % B<sub>2</sub>O<sub>3</sub>, the ratio of boron linked to silica is, in average, like the ratio of boron in the alumina sites (B/Al average of 2.87 in alumina sites and 3.36 distributed in the silica matrix). More boron available in the system means that, statistically, more [SiO<sub>4</sub>] are being substituted by [BO<sub>3</sub>] and boron has the chance to connect with other boron atoms (B-O-B), allowing a more flexible network. Even so, the silica regions are kept compressed.

In order to investigate the frequency of the Boson peak with changes in the elastic medium transformation, a Debye corrected representation for *B<sub>p</sub>*-VDOS is investigated by evaluating the Debye frequency  $\omega_D$  and Debye DOS  $g_D(\omega)$  in terms of longitudinal and transverse sound velocities. The Debye corrected representation for the aluminosilicate glasses investigated in this work is shown in Figure 4.19.

In terms of the CPA model, if the disorder is not changed (eg. the chemical topology) but just the value of the mean elastic constants or density, this correspond

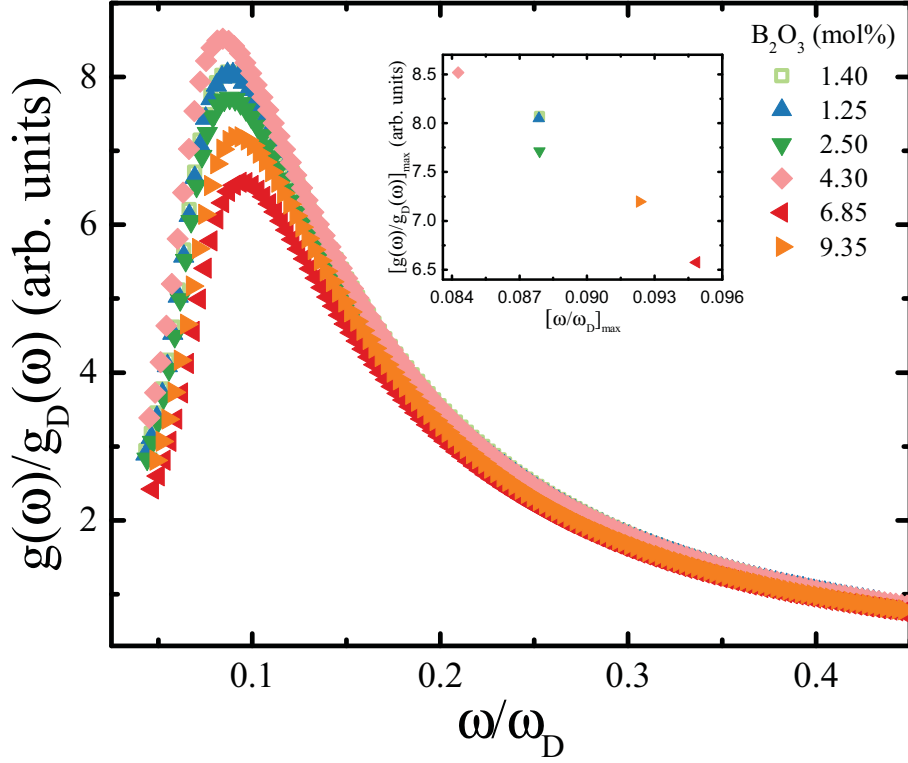


Figure 4.19: Reduced density of states  $g(\omega)/g_D(\omega)$  vs. the rescaled frequency  $\omega/\omega_D$ . The inset shows the maximum normalized intensity  $[g(\omega)/g_D(\omega)]_{max}$  and maximum rescaled frequency  $[\omega/\omega_D]_{max}$ .

to elastic-transformation scaling and all data points should fall onto a same curve. In the present investigations, this is clearly not the case because addition of  $B_2O_3$  modifies the glass structure and, consequently, the state of disorder is changed by changing the external conditions [123].

The maximum of the normalized intensity  $[g(\omega)/g_D(\omega)]_{max}$  and rescaled frequency  $[\omega/\omega_D]_{max}$  is shown on the inset of Figure 4.19. In general, it follows a tendency of increasing the frequency while the normalized intensity decreases. However, only two samples fall into a singular curve, the 1.40 and 1.25 mol %  $B_2O_3$ , which indicates that, structurally, the elastic heterogeneities are similar [123]. The correlation length, which refers to the minimum size of the shear fluctuation, is intrinsically related to the frequency and intensity. Increasing  $\xi$  enhances the  $\omega_{Bp}$  and shifts its position to lower frequencies. Considering the correlation length,  $\xi$ , shown in Figure 4.18, indeed,  $[g(\omega)/g_D(\omega)]_{max}$  and  $[\omega/\omega_D]_{max}$  confirms such behavior. Another factor that influences the position and/or intensity of the  $Bp$  is the structural “degree of disorder”. Increasing the “degree of disorder” just leads to an enhancement, while keeping the



$Bp$  position constant [123]. The sample containing 2.5 mol %  $B_2O_3$  may have a lower “degree of disorder” and for this reason, presents lower frequency.

The ternary aluminoborosilicate glasses present ionic conductivity (even very low), but high activation energy as shown in Figure 4.20.

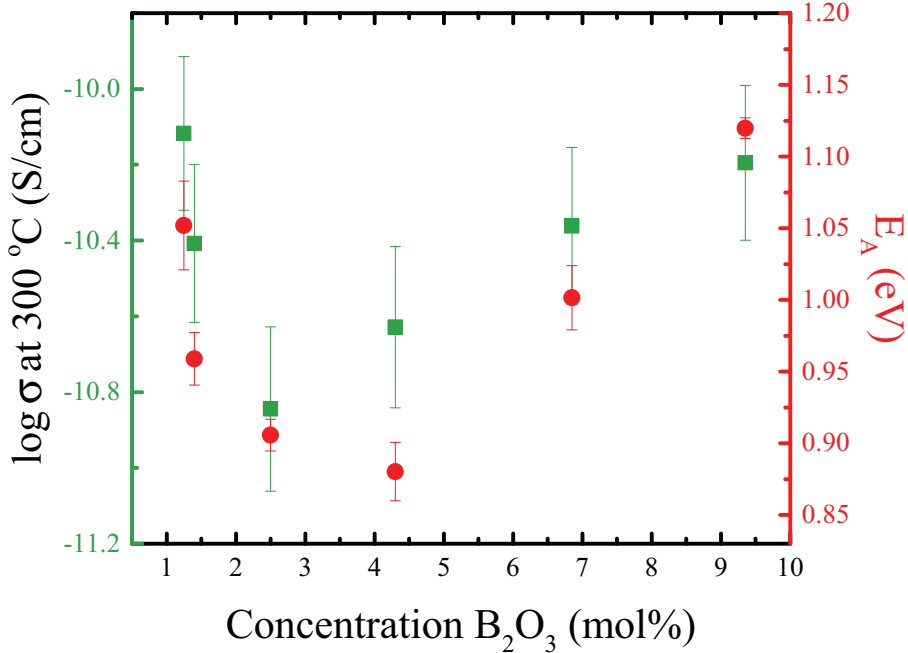


Figure 4.20: Ionic conductivity (green squares, left side) and activation energy (red circles, right side) of aluminoborosilicate glasses.

The ionic conductivity shows a minimum at 2.5 mol % of  $B_2O_3$ , while the activation energy reaches a minimum at concentration of 4.3 mol %  $B_2O_3$ . The main question about ionic conductivity is: what is the element that provides the local charge? Actually, the answer for this question is not simple and additional investigations should be made in order to prove any supposition. Some works on impurities of synthetic and natural quartz crystals, however, [218, 219] pointed out that trivalent aluminum substituting tetravalent silicon leads to a charge deficiency due to trivalent aluminum, that is commonly compensated by monovalent cations present interstitially. The most common compensator of the charge deficiency to aluminum are alkalis (M), giving rise to  $[AlO_4 - M]^0$  centers [220, 221]. In the present case, it may suggest that such centers are oxygen hole centers (OHC) provided by the reduction of trivalent ytterbium by the deficient oxygen of alumina. A local ionic conduction may also come from the effect of mixing network formers glasses. Several works have also shown that the

ionic conductivity is increased when B<sub>2</sub>O<sub>3</sub> is mixed to SiO<sub>2</sub> [222–224], which creates more charge localized structures and thereby cation sites with higher binding energies, allowing a mobile ion by charge density (in a short-range order magnitude) [222, 225].

Besides there are some other models for AC ionic conductivity in glasses, in this work it will be assumed Anderson and Stuart’s [223] model, since it is well established to describe the activation energy of ionic conductivity of silica glasses containing alkali ions [226, 227]. The total activation energy,  $E_A$ , is classified as a sum of two contributions: the electrostatic binding energy,  $E_b$ , and the strain energy,  $E_s$  [223, 226, 227]:

$$E_A = E_b + E_s = \frac{1}{\gamma} \left( \frac{ZZ_0e^2}{r + r_0} - \frac{ZZ_0e^2}{\lambda/2} \right) + 4\pi Gr_D (r - r_D)^2 \quad (4.9)$$

here, for the first part of the equation ( $E_b$ ),  $\gamma$  (also called covalency parameter) accounts for the deformability of the oxygen atom and is assimilated to a dielectric constant.  $Z$  and  $Z_0$  are the respective valences of an ion-oxygen pair,  $e$  the elementary charge,  $r$  and  $r_0$  are the respective ionic radii of the ion and oxygen and,  $\lambda$  is the lattice constant of the jump distance. For the second part of the equation ( $E_s$ ),  $G$  is the shear modulus and  $r_D$  is the radius of doorway, that is the size to connote a passageway between holes.

The present aluminoborosilicate glass series does not contain any alkali ions, which complicates to obtain quantitative values. However, the concept of optical basicity and electronic polarizability can be used to approximate the electrostatic binding energy  $E_b$  of the glass system. Since the electronic polarizability linearly increases,  $\alpha_m$  (see Figure 4.13), it is expected that the binding energy  $E_b$  should also increase with B<sub>2</sub>O<sub>3</sub> addition. Concomitantly, the shear modulus  $G$  has the opposite behavior (see Table 4.2). The  $A$  parameter shown in Table 4.3, indicate that the overlap distances for the bond between the cation and oxygen ions are becoming larger (except for sample containing 9.35 mol % B<sub>2</sub>O<sub>3</sub>, which value decreases around 12 % related to 6.85 mol % B<sub>2</sub>O<sub>3</sub>) and, thus, a more open network becomes easier to polarize.

From the present short-range considerations, the ionic conductivity is very low. It achieves a minimum at concentration of 2.5 mol % B<sub>2</sub>O<sub>3</sub> ( $-10.84 \text{ S cm}^{-1}$ ), and after this point it increases almost linearly. This is in accordance with optical basicity predictions, since until 2.5 mol % B<sub>2</sub>O<sub>3</sub>, the system holds more charge than pure silica and after such value, the charges may increase due to increase on the electronic

polarizability of the system. On the other hand, the activation energy reaches a minimum at concentration of 4.30 mol %  $B_2O_3$  (0.88 eV). This behavior suggests structural differences, that may be correlated to the short- and medium-range structure.

The samples containing the lowest concentration of  $B_2O_3$  (1.25 and 1.40 mol %) present the highest ionic conductivity ( $-10.11$  and  $-10.40$  S  $cm^{-1}$ , respectively) and activation energy (1.05 and 0.96 eV, respectively). This can be explained by the arrangement of boron around aluminum sites. At concentration until 1.40 mol %  $B_2O_3$ , only one boron will be linked to an aluminum site, i.e., the silica around such site will difficult the mobility of the ion (as physical and energetic barrier), resulting in a high activation energy. The same is valid for sample containing 2.5 mol %  $B_2O_3$ . Very interestingly, the sample containing 4.3 mol %  $B_2O_3$  presents the lowest activation energy and one of the lowest conductivities. At this concentration, it is expected that aluminum sites are almost saturated with boron. This will decrease the activation energy due to the boron in the second shell of aluminum sites forming a “barrier” to the silica network. Boron in trigonal configuration has a  $\pi$ -bond available, this brings a flexibility to these units, which would allow the mobile ion to move. The mobility will be facilitated by the trivalent ytterbium, that can act as a bridge to this mobile ion by reducing temporarily to divalent ytterbium. For the sample containing 6.85 and 9.357 mol %  $B_2O_3$ , the activation energy and ionic conductivity increases considerably. The electronic polarizability of the oxide ion,  $\alpha_O^{2-}$  (see Figure 4.13), decreases at this concentration, indicating that the ability of oxygen ions to transfer electrons is reduced. Moreover, at 6.85 mol %  $B_2O_3$  it is suggested that  $[BO_3]$  already started to substitute  $[SiO_4]$  in the network, avoiding regions close to aluminum sites [211]. The  $[Si-O-B]$  centers have a broader angular distribution [91], which leads to a denser silica region between aluminum sites. This fact could increase the activation energy due to local limitation on mobility of the charge.

Recently, the activation energy has been attributed to the reversible displacement of atoms in the structure surrounding the migrating cation [228]. In this manner, the approach of ionic conduction processes in glass can be firmly related to free volume, microscopic interactions and the overall glass structure [224, 229, 230]. A relation between the Boson peak position investigated by inelastic neutron scattering and ionic conductivity was found and correlated with developed free space [231, 232]. However,

in the present work such correlation is not found. Instead, the ionic conductivity and activation energy seems to be only related to the local structure around the aluminum-ytterbium sites. In this manner, the ionic conductivity and activation energy may provide local structural information of a local structure and free space around it, but alone it is incapable to describe the complete picture of the glass structure.

### 4.3 Topological modifications of silica glass by femtosecond laser exposure

Femtosecond (fs) lasers have been extensively used as a tool to provide structural modifications of optical materials. This technique allows cost-effective and single-step prototyping of photonic devices with uncomplicated control of the parameters, which is very important for production in large scale [233]. Nevertheless, characterization of the structured regions is quite challenging due to their micro-scale size and it reflects in the general knowledge of the glass structure. A considerable advance has been made to understand the glass modification after fs-laser infrared irradiation. Permanent structural modification, such as densification, increasing refractive index and fictive temperature,  $T_f$ , are usually reported [233–237].

In this work, analysis of the effect of fs-laser irradiation over  $\text{SiO}_2$  glass on vibrational properties is presented. Since the characteristics of topological heterogeneity of densified glasses have been already extensively investigated in the recent past, a pure silica sample isostatically compressed to 100 MPa\* was used as a reference for comparison to the fs-laser structural modification. Spatially low-frequency Raman spectroscopy, Brillouin scattering, birefringence microscopy, UV-Vis spectroscopy and photoluminescence spectroscopy were employed as a non-destructive characterization techniques to probe topological changes at the short- and intermediate-range order.

The silica glass with frozen-in pressure of 100 MPa was produced by heating at constant pressure up to a temperature of 1523 K and equilibrated for 12 min. After equilibration above  $T_g$ , the glass was cooled down under pressure at a rate of 10 K/min down to room temperature [238].

The fs-laser modified samples were obtained from a rod of commercially available fused silica (Heraeus - Suprasil 2 type A). A thin disc of 2 mm thickness and 3 cm diameter, polished on both sides was prepared. Fs pulses were generated by a single frequency Ti-Sapphire laser (Spectra Physics, Spitfire) regenerative laser amplifier system emitting pulses at  $\lambda = 800$  nm, FWHM = 200 fs and a repetition rate of 1 kHz. The pulse energy was controlled using a half-wave plate and a linear polarizer. The laser beam was focused inside the bulk glass (approximately 200  $\mu\text{m}$  under the

---

\*this sample was prepared by Dr. Shigeaki Sawamura [238].

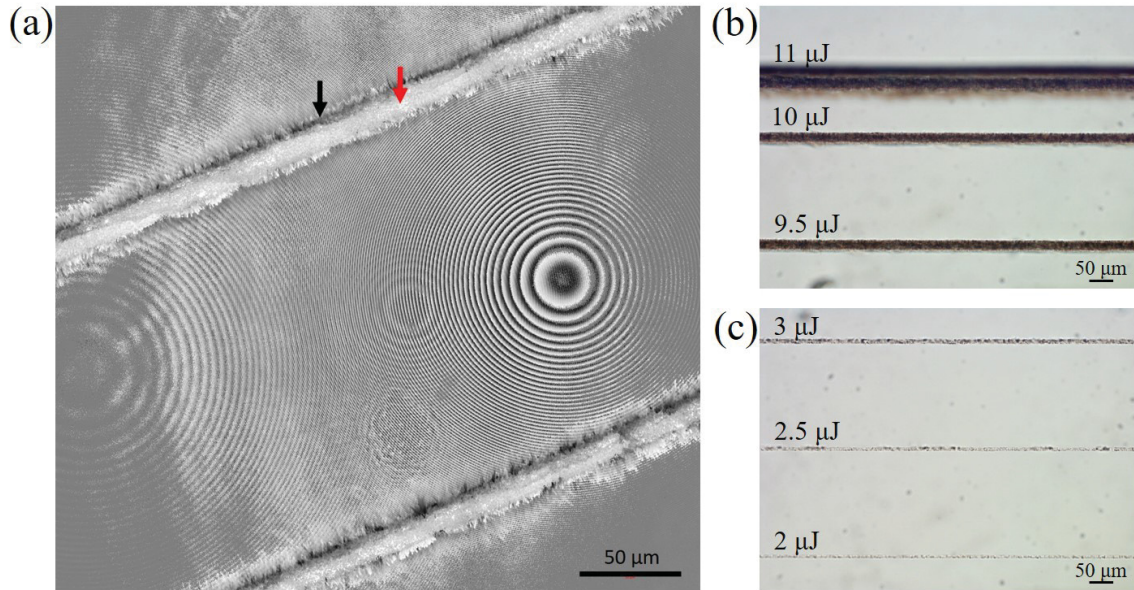


Figure 4.21: (a) Interferometer microscopy image of two structured lines. The line on the top is after exposure of  $10\ \mu\text{J}$  and on the bottom of  $9.5\ \mu\text{J}$  pulse energy. The red arrow refers to measurements focused on the “center”, while the black arrow refers to the point focused on the “edge” of the structured lines. Optical microscopy images of the structured lines of a group of higher pulse energies (b) and a group of lower pulse energies (c).

surface). The irradiation procedure resulted in a laser modification for each energy pulse, while the sample was moved at a constant speed of  $6 \times 10^{-3}\ \text{km/s}$  by a motorized linear stage. Nineteen lines with different pulse energies in the range from  $1.5\ \mu\text{J}$  to  $11\ \mu\text{J}$  were inscribed. Each new line was parallelly shifted around  $200\ \mu\text{m}$  relative to the former to achieve enough separation for singular analysis and avoid any spatial overlap.

The Figure 4.21 shows interferometer- and optical- microscopy images of the silica glass after fs-laser exposure. In Figure 4.21(a), the line on the top is after  $10\ \mu\text{J}$  and on the bottom after  $9.5\ \mu\text{J}$  pulse energies exposure. In this study, two regions were investigated, the center and the edge of the lines (pointed by a red and black arrow, respectively, in Figure 4.21(a)). The depth of the line irradiated by  $10\ \mu\text{J}$  was estimated as  $4\ \mu\text{m}$  and thickness as  $20\ \mu\text{m}$  by interferometer microscopy. Nevertheless, only the range from  $7.5\ \mu\text{J}$  up to  $11\ \mu\text{J}$  was systematically investigated, because the thickness of the lines below such pulse energies becomes very small, as shown in Figure 4.21(b) and (c), challenging any optical measurement.

Analysis of intrinsic defects at short-range order was conducted by photolumines-

cence spectroscopy, as shown in Figure 4.22. After fs-laser irradiation, the photoluminescence emission spectra exhibit three peaks, at 1.9 eV ( $\sim 650$  nm), 2.2 eV ( $\sim 560$  nm) and 2.9 eV ( $\sim 420$  nm).

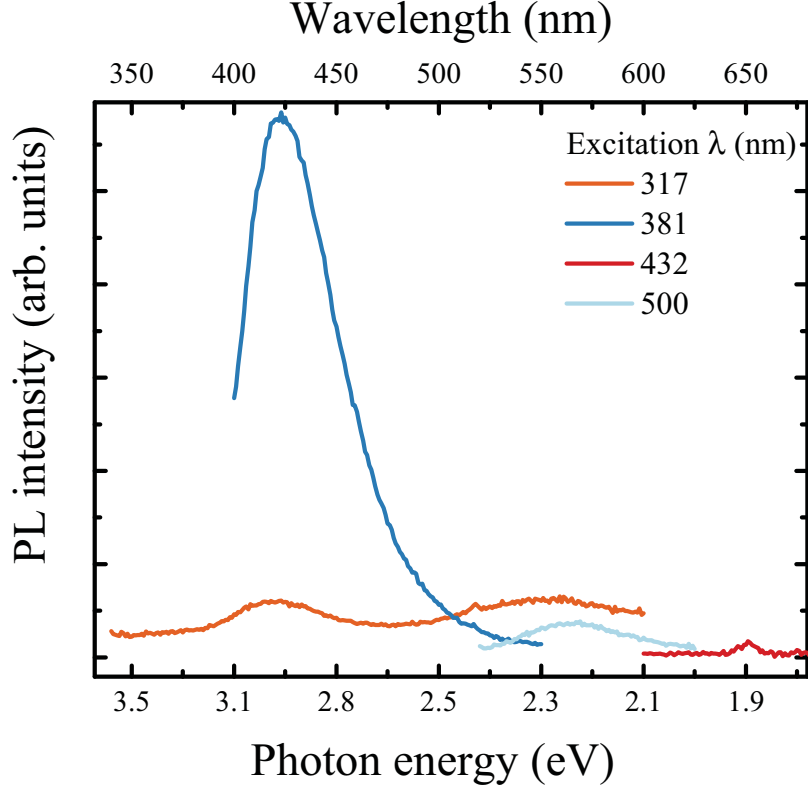


Figure 4.22: Photoluminescence emission spectra of silica glass after fs-laser exposure.

The small band located at around 1.9 eV is already well recognized as a manifestation of non-bridging oxygen hole centers (NBOHC:  $\equiv\text{Si-O}\cdot$ ), described as a hole trapped in a single oxygen atom bound to a single silicon on three oxygen atoms in the  $\text{SiO}_2$  structure [239–242]. The presence of this band seems to be typical for amorphous  $\text{SiO}_2$  irradiated by fs-laser [243, 244] and may have origin from ionizing radiation process, which breaks one oxygen of the silica tetrahedra and ejects the oxygen into an interstitial position [239]. The origin of the peak at about 2.2 eV is still in debate. Some authors relate this band to E'-type defects [245], where a NBOHC and an E' center could be created simultaneously, according to the reaction:  $(\equiv\text{Si-O-Si}\equiv \rightarrow \equiv\text{Si-O}\cdot + \cdot\text{Si}\equiv)$  [246]. Other authors associate it to a radiative recombination of a self-trapped exciton (STE) [242], since in amorphous  $\text{SiO}_2$  the mobility of the hole and exciton is limited to the local disorder, which could facilitate the formation of such self-trapping of these particles [245]. Recently, Zhou and Li associated this photolu-



minescent defect with physical disorder induced by pressure or laser-induced shock waves in SiO<sub>2</sub> network [247]. The most intense band at 2.9 eV, also present in quartz [240] and silicon clusters aged inside aqueous suspensions [248], is usually attributed to an irradiation-produced intrinsic defect. Some contribution from densification is also expected, because it could enhance the yield of the defect pairs [249]. Although, this emission is sometimes associated to various other defects, such O<sub>2</sub><sup>-</sup> defects [250], a weak O-O bonding defect [242] and carbon implanted oxide [251].

Raman spectroscopy at excitation length of 514 nm reveals a high fluorescence background, as shown in Figure 4.23. This fluorescence background may have origin from the stresses present in the structured lines and/or from short-range order defects, such as broken Si-O bonds [235]. The fact that the lines are engraved inside the glass, below 200 μm, could be, in principle, a reason to deviate the original beam focused at the surface. However, measurements conducted at several points from the surface down to 200 μm did not show any deviation from the surface data after baseline subtraction and area normalization by integrated total area.

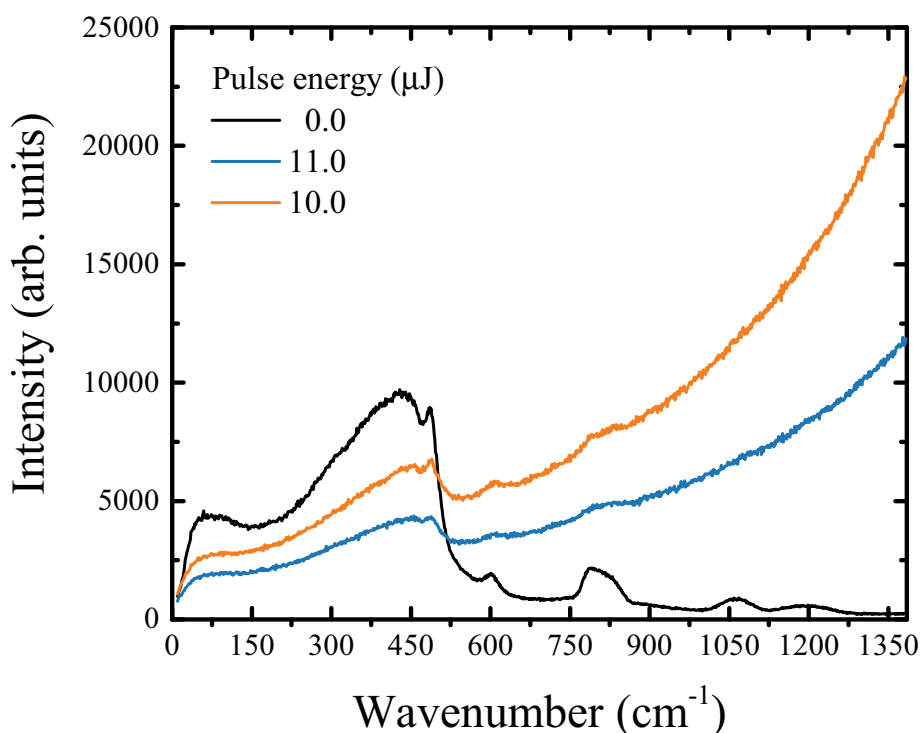


Figure 4.23: Raman spectra of pristine and two structured lines at excitation length of 514 nm. The structured lines show a very high fluorescence background.

Since the origin of this high fluorescence is unknown, a baseline could not be



defined by simple mathematical functions, such as polynomial fit or equivalent, otherwise physical information could be lost due to a wrong baseline choice. In order to not compromise the results, specially at the region of the Boson peak, the disturbing fluorescence background was removed by extended multiplicative signal correction (EMSC) model, followed by an area normalization from 750 up to 870  $\text{cm}^{-3}$ . This method was developed by Stark and Martens in 1989 in order to attain a more effective separation of chemical and physical effects in light spectroscopy, because sometimes the physical and chemical effects in the spectra are sufficiently different, and may be separated by multivariate statistical modelling [252].

The Raman spectra after EMSC model, area normalization and temperature corrected by Eq. (3.3) are shown in Figure 4.24. For better visibility, only some selected pulse energies (selected lines) were displayed. The signal of structured lines is very noisy due to the fluorescence background. Any measurement at longer exposure time and/or several acquisitions has been shown to be very challenging due to saturation of the detector of the equipment. This figure shows a typical vibrational behavior for this kind of structural modification [253, 254]. Upon fs-laser irradiation, the maximum of the MB shifts slightly to higher frequencies. By drawing an analogy between fs-laser irradiation and densification induced irreversible structural changes and permanent increase mass density as consequence, this shift is assigned to a simple decrease of the intertetrahedral angle  $\theta_{Si-O-Si}$  in the silica network [235, 255–257]. Furthermore, the intensity of the MB decreases, revealing a decreasing in connectivity of the glass network [210]. The intensity of the *D1* band increases, however no shift is detected, suggesting an increase of 4-membered rings. The intensity of the *D2* bands also increase and the frequency tends to shift to higher wavenumber, but are marginally affected by fs-laser irradiation (maximum frequency shift of  $3.5 \pm 0.035 \text{ cm}^{-1}$ ) in opposition with the behavior observed in indented silica [258, 259], where a large shift of the frequency of the band *D2* is observed (see Figure 4.26). This observation is in agreement with modification observed both at high temperature [255], high pressure [235] and quenched vitreous silica [76] and, is a clear signature of a different statistical distribution of silica rings. On the other hand, the Raman spectra of the compressed sample reveal that the distribution of silica rings is slightly affected, when compared to pristine. A slight shift towards higher frequency of the MB indicates a decrease of

the intertetrahedral bond angle  $\theta_{Si-O-Si}$  in the silica network and the increase of the  $D2$  band, meaning an increase of the 3-membered rings.

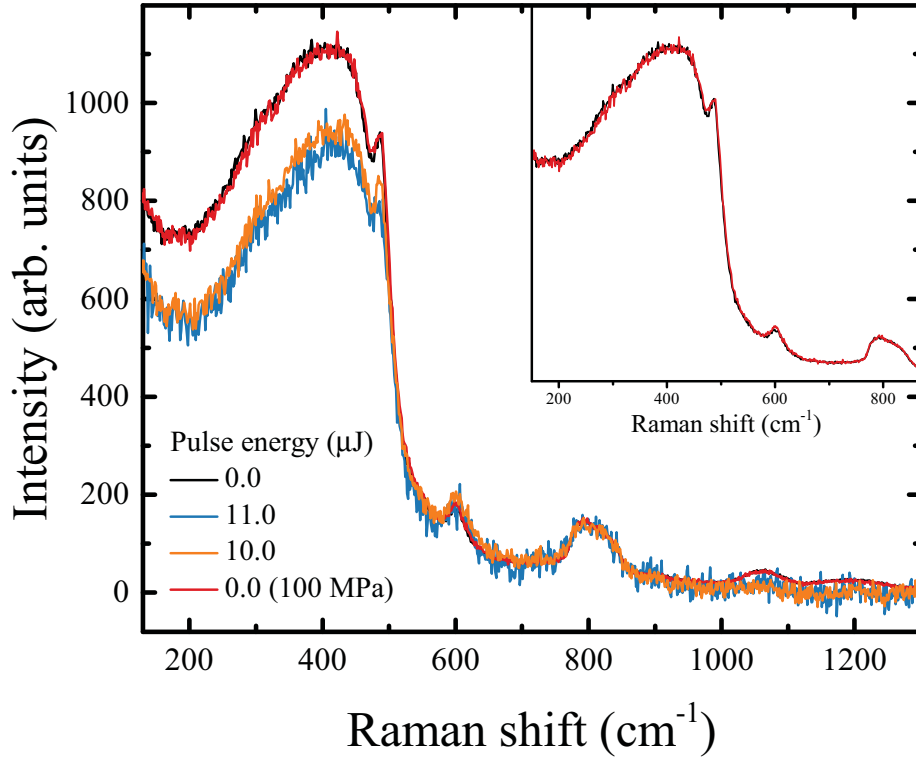


Figure 4.24: The Raman spectra after EMSC model, normalization by integrated area from 750 up to 970 nm and temperature corrected for pristine, selected structured lines and compressed sample. The inset emphasize the spectra of pristine and compressed sample.

Even though the structural changes by fs-laser irradiation in glasses are not completely clear, several studies have already been reported as due to plasma fluctuations (plasmon modes within confined spaces). Micro-explosion of the focal region, exhibiting a signature of a high-pressure wave have been proposed as permanent structural modification [260]. This reaction is due to high temperatures and pressures generated by localization of high electron densities in a focal region during the transfer of the plasma energy [261]. Furthermore, the temperature of the glass rises very fast directly after the absorption of a laser pulse and decreases down to room temperature by ultra-fast thermal quenching with higher fictive temperature than slowly cooled glass. The increase of the fictive temperature  $T_f$ , which represents a temperature at which the liquid structure is frozen during the cooling down, can lead to glass structural relaxation and to a change of average disorder [262]. Martinet et al. [255] have established an empirical correlation between the variation of the Raman main band

peak frequency  $\omega_{MB}$ , with the fictive temperature  $T_f$  for pure silica:

$$\omega_{MB} = 0.02 T_f(^{\circ}C) + 419.5 \quad (4.10)$$

The  $\omega_{MB}$  was determined by decomposition of the band by several Gaussian functions and the  $T_f$  was calculated using the Eq. (4.10). The result is shown in Figure 4.25.

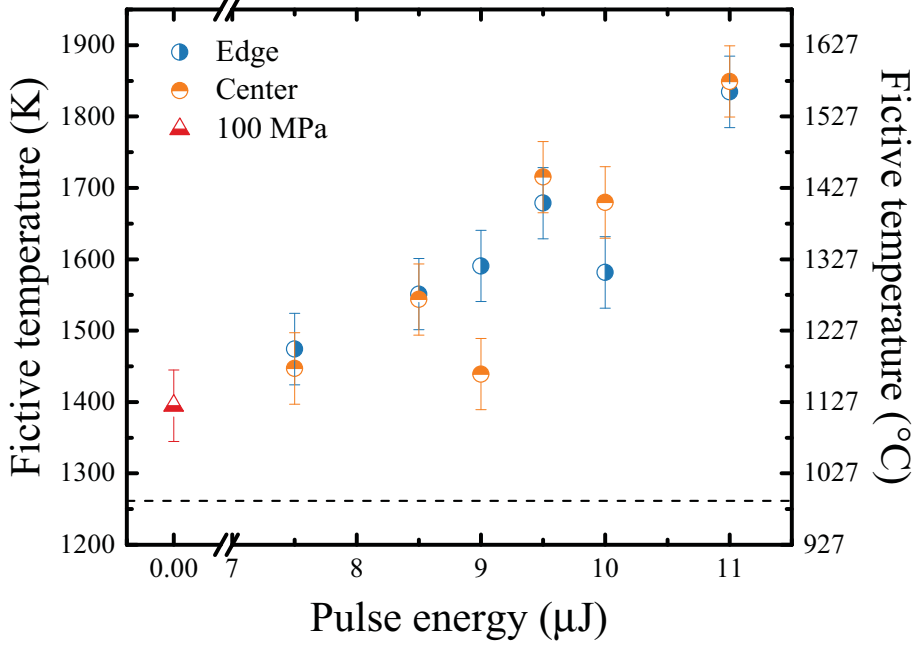


Figure 4.25: Fictive temperature of compressed sample and structured lines measured on the center and edge of the lines. The dashed line located at 1261 K is a reference for pristine.

The fictive temperature increases according to the pulse energies. For all modified lines and compressed sample, the fictive temperature is above  $T_g$  (around 1390 K [238]). Several studies correlate the  $T_f$  with the  $D2$  Raman peak, i.e., increasing  $T_f$  leads to an increase of the number of three-membered rings [243].

Even though there are several evidences indicating that the mechanism of densification by fs-laser irradiation is very different from densification under high-pressure and shock compression [263], the  $D2$  Raman bands are marginally sensitive to residual elastic strains and the frequency position may be related to the density of a silica glass [258, 264]. By shock compression experiments [264], Perriot obtained an empirical relation between mass density and frequency shift of the  $D2$  bands [258]:

$$0.143 \log_{10} \left( \frac{\rho}{\rho_0} \right) = \log_{10} \frac{\nu}{\nu_0} \quad (4.11)$$

here,  $\rho$  and  $\rho_0$  are the mass density of the sample and pristine, respectively, whereas  $\nu$  and  $\nu_0$  are, respectively, the final and initial  $D2$  band frequency position.

Following Eq. (4.11), the mass densities of the structured lines were estimated and are shown in Figure 4.26.

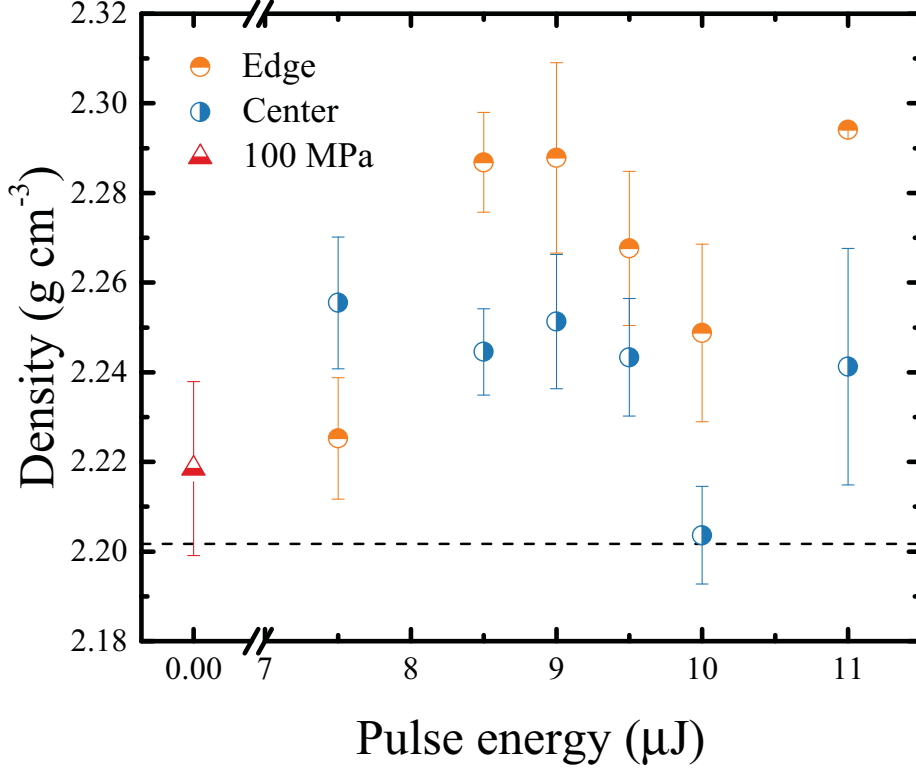


Figure 4.26: Mass density estimated from Eq. (4.11) for structured lines and compressed sample. The dashed line located at  $2.203 \text{ g cm}^{-3}$  is a reference for pristine.

In general, the density of the structured lines is higher than pristine. Only to validate the Eq. (4.11), the compressed sample has a density evaluated as  $2.214 \pm 0.001 \text{ g cm}^{-3}$  using Archimedes' principle (with dry ethanol as the immersion liquid) [238], whereas a value of  $2.2184 \pm 0.0194 \text{ g cm}^{-3}$  is obtained by Eq. (4.11).

It is valid to note that density by itself is not a measure of the degree of densification [264]. Atomistic simulations have been shown that it is possible to produce glasses (either by directly quenched from the high temperature melt or deformed from ambient temperature through cycles of quasi-static compression-decompression) with the same density, similar short- and intermediate-range order, but with significantly different pressures [265]. However, to induce an increase in  $D1$  and  $D2$  intensity bands at Raman spectroscopy, the pressures must be higher than few GPa for static

compression, i.e., the glass must be plastic deformed [235, 266]. From this standpoint, the pressure can be estimated by an equation derived from high-pressure methods (no temperature applied), such as diamond anvil cell [266] and high-pressure cell [267]:

$$\frac{\Delta\rho}{\rho} = \left[ \frac{1}{1 + \beta \exp(-P_{\max}/P_0)} \right] \left( \frac{\Delta\rho}{\rho} \right)_{\max} \quad (4.12)$$

here,  $\rho$  is the density of the material,  $\Delta\rho/\rho$  (%) is the fraction of inelastic density change,  $(\Delta\rho/\rho)_{\max} = 21\%$  is the maximum densification ratio,  $\beta = 5000$  and  $P_0 = 1.67$  GPa.

Following Eq. (4.12), the average pressure of the structured lines is correspondent to an order of magnitude of few tens of GPa (see Table 4.4). This is not in agreement with the pressure values obtained by birefringence microscopy. The estimated stress (cross section of the lines) is in the order of magnitude of few hundred MPa. The Figure 4.27 shows the regions around the edges as tensile stressed, but this result is likely to be distorted by the change in stress field direction. The stress inside the modified region is also additionally distorted due to the unknown change in the photo elastic constant. Nevertheless, the measurement shows stresses that do not exceed 104 MPa. Furthermore, the stress is not evenly distributed along the visible modification (it is possible that the bottom part refers to a crack caused by the cut of the sample), but the top part always shows the maximum stress. Here, the stress distribution seems to be highest for a shell-like structure around the modified volume.

Sugiura et al. [264] have shown that the density after static compression was much higher than that after shock compression up to equal pressure. This occurs because shock loading is reproduced by similar treatment in static compression, although there are large differences in temperature between both methods [264]. In the case of fs-laser irradiation, the process of densification is completely different than both methods, short pulses and nonlinear excitation are involved, because of the strong electromagnetic field. This nonlinear excitation results in an electronic excitation in the small region of the focusing region [237]. Further, the elastic stress is confined in a very small volume (at very short exposure time) and the subsequent relaxation of the stress results in the pressure wave generation, which structural change is dominated by thermal effects [237, 268]. Sakakura et al. have estimated the stress of silica glass after

fs-laser irradiation by detection of a laser induced pressure wave using a transient lens method [263]. They registered a maximum measured stress around 50 MPa, for pulse energy of 300 nJ. At the same pulse energy, they have estimated that the initial stress in the photoexcited region must be around 520 MPa by thermoelastic simulations.

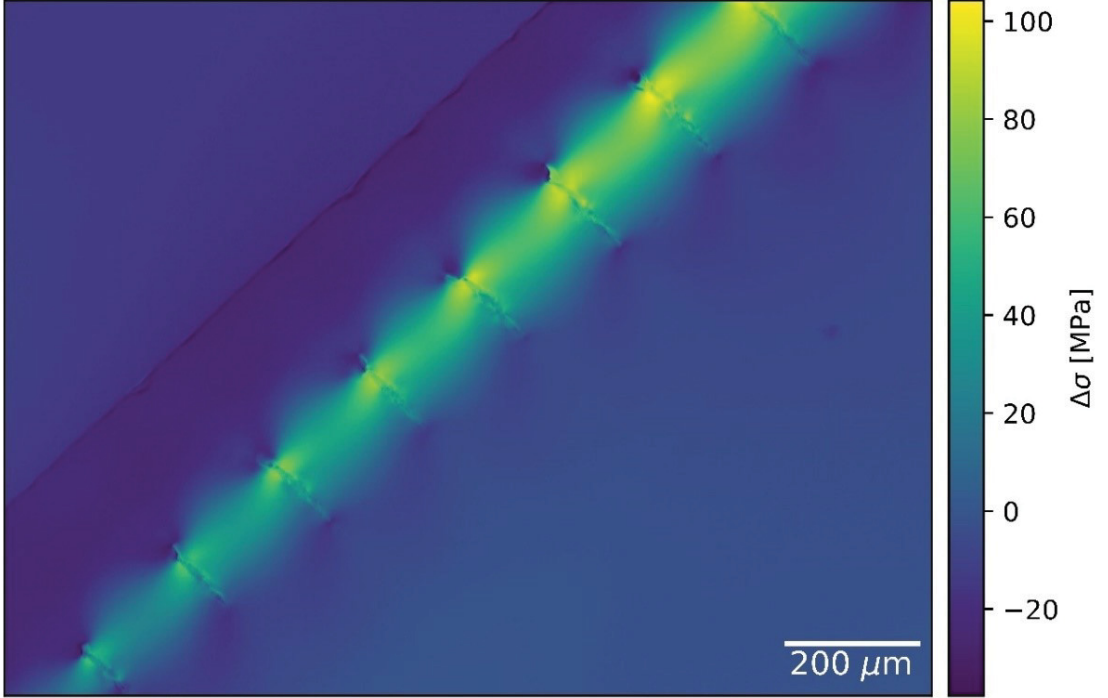


Figure 4.27: Stresses extracted from birefringence measurements. The pulse energy increases from left to right.

The refractive index can be determined by two major factors, density and mean polarizability,  $\alpha$  [269]. They are connected with each other in the Lorentz-Lorenz relation:

$$\frac{n^2 - 1}{n^2 + 2} = \frac{4\pi}{3} \frac{N_A \rho}{M} \alpha \quad (4.13)$$

here,  $M$  is the molar weight and  $N_A$  the Avogadro number. Considering  $n = 1.47$  and  $\rho = 2.20 \text{ g cm}^{-3}$ , the  $\alpha$  parameter is  $\sim 2.96 \times 10^{-24} \text{ cm}^{-3}$  for vitreous silica. The refractive index of structured lines and compressed sample was calculated following Eq. (4.13) and the values are shown in Table 4.4.

The longitudinal sound wave velocity,  $\nu_L$ , is related to the refractive index in back-scattered Brillouin signal by the relation:

$$\nu_L = \frac{f_B}{2n} \lambda \quad (4.14)$$

here,  $f_B$  is the Brillouin frequency and  $\lambda$  is the wavelength of the incident beam. On the other hand,  $\nu_T$  can be estimated from the longitudinal sound velocity and density using the generalized Cauchy relation,  $M = a + bG$ , where  $M$  is given by  $(\rho \nu_L^2)$  and  $G$  by  $(\rho \nu_T^2)$  [270]. The  $a$  and  $b$  are constants. It is assumed a value of  $-24.74 \times 10^9$  and 3.36 for  $a$  and  $b$ , respectively [266, 271, 272]. The Brillouin frequency (measured only on the center of the structured lines), longitudinal sound velocity calculated by Eq. (4.14) and transversal sound velocities calculated by Cauchy relation are shown in Table 4.4.

Table 4.4: Densification  $\Delta\rho/\rho$ , relative pressure, refractive index  $n$  at 633 nm, Brillouin frequency  $f_B$ , longitudinal sound velocity  $\nu_L$ , transversal sound velocity  $\nu_T$ , shear modulus  $G$ , bulk modulus  $K$  and longitudinal modulus  $L$  of structured lines investigated in this study.

Pulse energy ( $\mu J$ )	$\Delta\rho/\rho$ (%)	Pressure (GPa)	$n$ ( $\pm 0.001$ )	$f_B$ (GHz)	$\nu_L$	$\nu_T$	$G$ (GPa)	$K$ (GPa)	$L$ (GPa)
0.0	-	-	1.457	35.745	5984.494 $\pm 1.711$	3742.127 $\pm 0.035$	30.83 $\pm$ 0.08	37.74 $\pm$ 0.15	78.85 $\pm$ 0.26
11.0	1.76	10.23 $\pm$ 0.01	1.467	35.544	5911.959 $\pm 9.304$	3699.691 $\pm 0.191$	30.67 $\pm$ 0.46	37.43 $\pm$ 0.81	78.33 $\pm$ 1.43
10.0	2.09	5.06 $\pm$ 0.25	1.458	35.477	5937.597 $\pm 6.759$	3719.438 $\pm 0.139$	30.48 $\pm$ 0.34	37.04 $\pm$ 0.59	77.69 $\pm$ 1.04
9.5	2.90	11.17 $\pm$ 0.01	1.467	35.460	5895.961 $\pm 5.753$	3691.57 $\pm 0.117$	30.57 $\pm$ 0.29	37.22 $\pm$ 0.50	77.98 $\pm$ 0.88
9.0	2.20	10.64 $\pm$ 0.01	1.469	35.509	5896.285 $\pm 7.369$	3690.25 $\pm 0.150$	30.66 $\pm$ 0.37	37.39 $\pm$ 0.64	78.27 $\pm$ 1.13
8.5	1.91	10.37 $\pm$ 0.01	1.468	35.569	5912.942 $\pm 6.041$	3699.51 $\pm 0.124$	30.72 $\pm$ 0.30	37.51 $\pm$ 0.53	78.47 $\pm$ 0.93
7.5	2.38	10.79 $\pm$ 0.01	1.470	35.543	5897.998 $\pm 6.039$	3690.25 $\pm 1.123$	30.71 $\pm$ 0.30	37.50 $\pm$ 0.52	78.46 $\pm$ 0.93



The linewidth at full width at half maximum (FWHM) of the Brillouin frequency peak is shown in Figure 4.28. For the structured lines, the linewidth increases with increasing pulse energy. A study from Caponi et al. [146] correlated the increasing

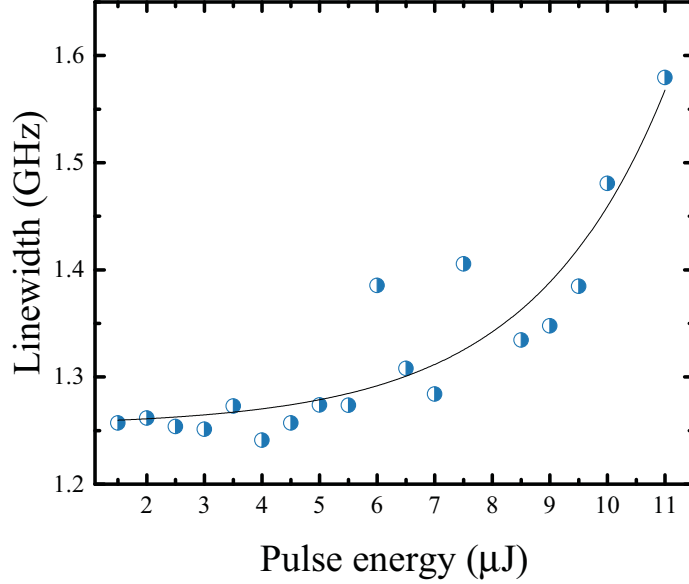


Figure 4.28: Linewidth (FWHM) of visible Brillouin peaks at room temperature versus pulse energies (range 1.5 – 11  $\mu\text{J}$ ) for the center of lines.

of Brillouin linewidth with increasing pore size in silica porous systems, which they related to the effect of absorption due to the disorder produced by the pores, shape, dimension and distance between pores. Equally, fs-laser irradiation causes nanostructures in the glass, well known as nanogratings. The latter was revealed as porous nanoplanes, only observed in tetrahedral glasses, such as silica and slightly doped silica [262, 273]. The nanopores are created due to the fast relaxation of the self-trapped exciton, which prevents recombination and dissociated atomic oxygen, where some of them are dissolved in the condensed glass whilst the rest is trapped inside the nanovoids [262, 273].

Investigations of the topological heterogeneity of silica glass after fs-laser irradiation have been conducted by low-frequency Raman spectroscopy. Different theoretical models have been proposed for the prediction of the spectral dependence of the coupling factor  $C(\omega)$ . For example, Martin and Brenig model [274] expects a quadratic power dependence of the coupling factor as function of the frequency  $C(\omega) = \omega^2$  for damped acoustic plane waves and exhibit a maximum at frequencies close to those of the boson peak. For the case of silica glass, the authors have compared in a previous

study [149] the data obtained by Raman spectroscopy and heat capacity at low temperature, and found that the coupling factor dependence is very well described by a polynomial function  $C(\omega) = A\omega^\alpha + B$ , where  $A$ ,  $B$  are constants and the exponent  $\alpha = 1.647$ . The dependence of the coupling factor to the pressure has been mentioned in some studies and the results and the interpretation converge. Generally, for high densification ratio ( $\sim 21 - 23\%$ ),  $C(\omega)$  has a great dependence with densification ratio [173, 275]. On the other hand,  $C(\omega)$  is assumed to be marginally affected by the densification ratio if it is less than  $\sim 15\%$  [173, 275].

In the present study, the densification ratio is very small ( $< 3\%$ ) and, therefore, the coupling coefficient was assumed to be constant regarding the densification. Considering that all related samples are chemically identical, the  $C(\omega)$  obtained from pure silica obtained in Chap. 4.1 was used to estimate the VDOS of the structured regions and pristine, therefore an interpretation of the characteristic of VDOS could be evaluated. Figure 4.29 (a) shows only some selected pulse energies (to facilitate the view) of the  $g(\omega)/\omega^2$  of the center of structured lines and compressed sample. Figure 4.29 (b) shows the Boson peak frequency  $\omega_{Bp}$  for the center and edge of the structured lines and compressed sample. The dashed line in (b) is a reference for pristine.

For all structured lines, including edge and center position,  $\omega_{Bp}$  shift to lower frequencies while their intensity decrease. This observation is not in agreement with characteristic Boson peak behavior observed in silica glass subjected to external pressure, whether hydrostatic (at room- [276] and high-temperature ( $\sim 500^\circ\text{C}$ ) [173, 272]) or by indentation [259]. The compressed sample shows a typical behavior of silica glass subjected to external pressure, i.e., the intensity decreases and the  $\omega_{Bp}$  shifts to higher frequencies. The only case that the Boson peak present similar behavior, as after the fs-laser irradiation, is for the normal liquid state: the intensity decreases with temperature rise and, the  $\omega_{Bp}$  exhibits a temperature softening, moving to lower energy when heating the glass towards the liquid state [277].

Even though both permanently densified and fs-laser irradiated silica glass leads to an increase of the mass density, a comparison between them reveals that the topological heterogeneity is very different. Figure 4.30 shows that the Boson peak frequency tends to increase according to the pressure in high-temperature high-pressure (HT-HP) compression (temperature  $\sim 500^\circ\text{C}$ ) silica glass, while for the structured lines,

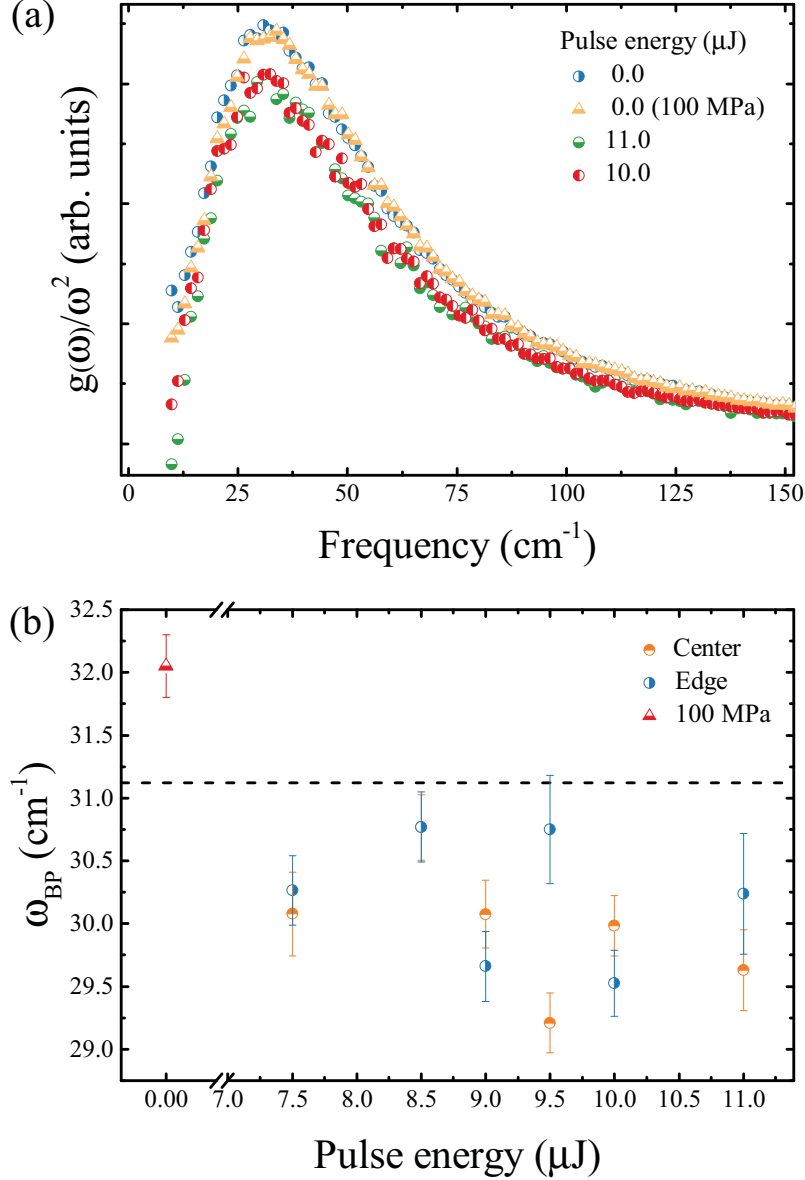


Figure 4.29: (a) Boson peak of VDOS of the center of the lines and compressed sample. (b) the maximum Boson peak frequency ( $\omega_{\text{BP}}$ ) for the edge and center of the structured lines. The dashed line in (b) indicate the  $\omega_{\text{BP}}$  position for pristine.

the Boson peak is even below the pristine and seems to be practically independent of density. This implies that the density by itself is not the only parameter governing the Boson peak behavior. The theory of elasticity with spatially fluctuating elastic constants (heterogeneous-elasticity theory) has been associated to describe the anomalies related to the Boson peak [124].

The mechanical properties ( $G$ ,  $K$ ,  $L$ ) and longitudinal- and transversal-sound velocity usually tend to increase according to increasing pressure and mass density in

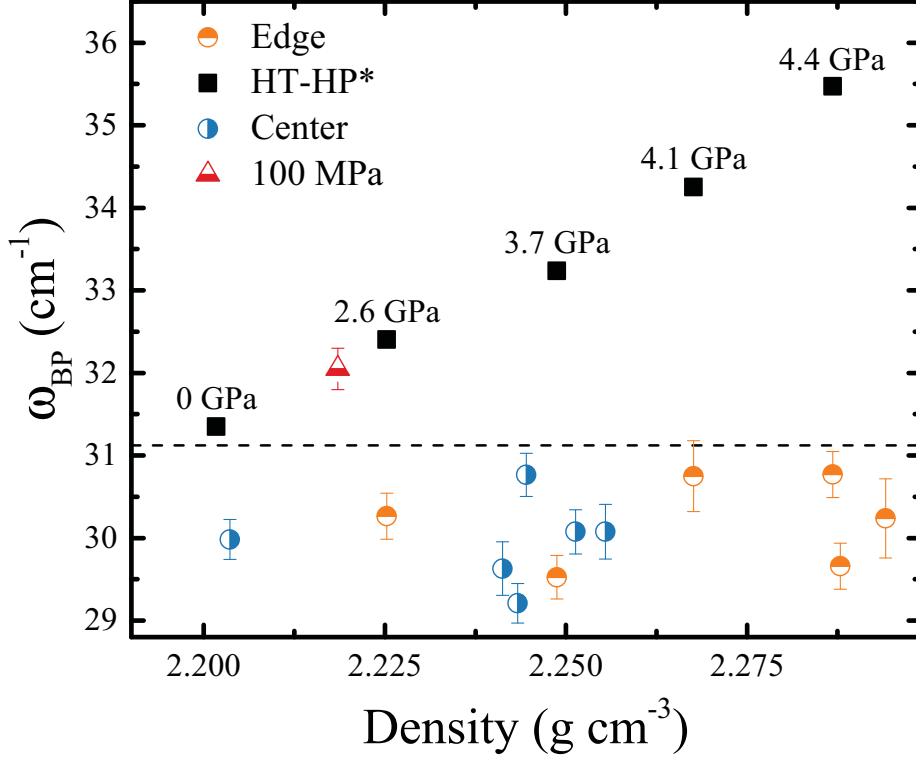


Figure 4.30:  $\omega_{BP}$  comparison between permanently densified silica and fs-laser structured lines. The dashed line is a reference for pristine. See text for details. \* Reference for HT-HP multi-anvil apparatus reproduced from Ref. [272] with permission of the publisher under licence number RNP/19/NOV/020661. Rights managed by American Physical Society.

compressed glasses [238, 278]. The mechanical properties of the compressed sample were determined by means of ultrasonic measurement. Since there is a divergence of the values between this method and Brillouin scattering, a direct comparison of the absolute values is incompatible [279]. However, comparing the mechanical properties and both sound velocities of pristine and structured lines, the values are slightly lower than pristine (see Table 4.4).

Investigations of the temperature dependency of elastic properties of silica glass by molecular dynamics simulations have shown that elastic moduli and longitudinal- and transversal- sound velocities, in the range between 1600 and 2400 K, slowly decrease from their maxima [280]. At this temperature range, for SiO<sub>2</sub> glass, there are two thermal vibrational modes: one is the stretching of the Si-O bond length (as an effect of thermal expansion) and change of the intertetrahedral bond angle; the other is the distortion of the network, by changing the statistical distribution of the rings [280]. These factors impact in the force constants, leading to a dependence of the elasticity.

The average length scale  $\xi$  has been estimated through Eq. (4.1), assuming  $S=1$  and is shown in Figure 4.31. The structured lines present a discrete higher average

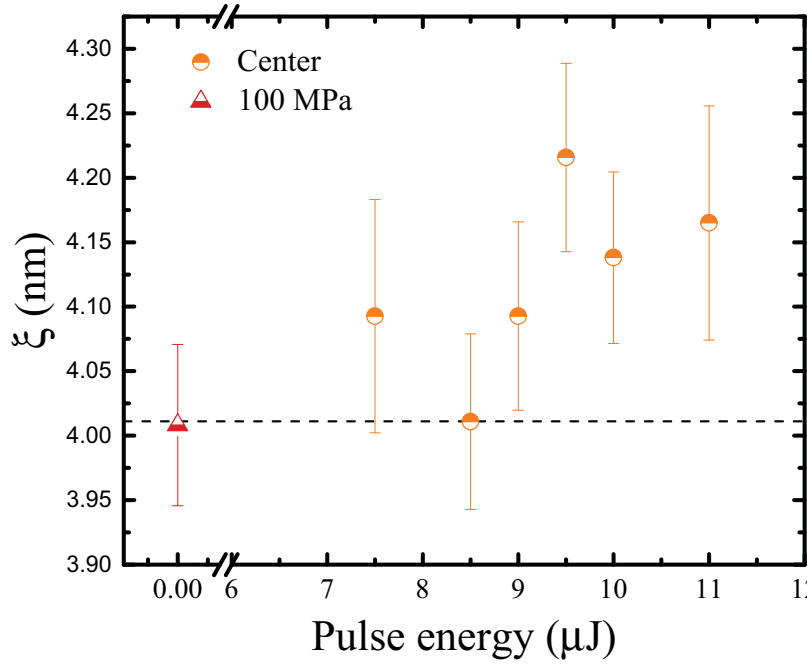


Figure 4.31: Average correlation length of compressed silica and center of structured lines.

size of the heterogeneity than pristine and compressed sample, indicating an increase of elastic heterogeneity.

Silica glass is one of the rare materials in which the microscopic structure of the modes at the origin of Boson peak anomaly has been extensively investigated. One hypothesis is that the number of tetrahedra involved in the rotational motion contributes to the Boson peak in silica. Structural theoretical models based on single, a pair, five and more tetrahedra have been compared to inelastic neutron scattering [62]. Though 6-membered rings dominate, the fraction of 5- and 7-membered rings are each about 10%. Sokolov et al., have estimated that the number density of modes contributing to the Boson peak is of the same order as that for mismatched 5- or 7-membered rings for many types of glasses [79]. Shcheblanov et al. estimated the evolution in the distribution of rings in vitreous silica after femtosecond multipulse irradiation by Raman spectroscopy and molecular dynamics simulations. The statistical distribution of rings is shown in Figure 4.32. Indeed, the size distribution of six- and, seven-membered rings collapse by about - 2.2% when compared to a non-irradiated vitreous silica [281]. Furthermore, populations of smaller rings, such as

3- and 4-membered rings, and larger rings (larger than 8-membered rings) increase significantly.

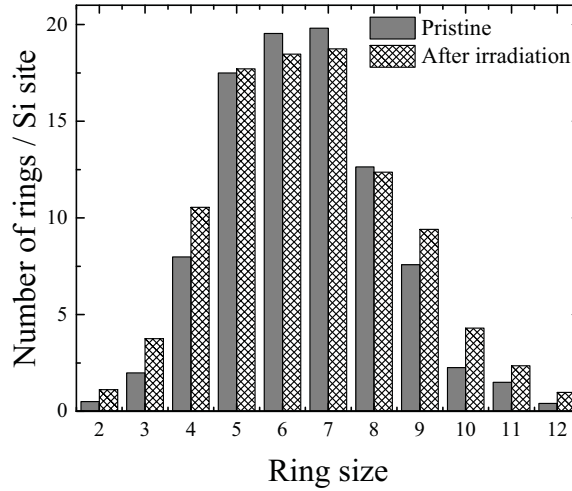


Figure 4.32: Evolution in the distribution of rings in vitreous silica before and after fs-laser irradiation. Adapted from Ref. [281] with permission of the publisher under licence number RNP/19/NOV/020672. Rights managed by American Physical Society.

The influence of the small rings is expected to affect the intermediate-range properties in a severe way due to the small angles and planarity of such structural units [83–85]. As found by Uchino et al., the consequence of the smaller rings for larger rings is that the latter may be geometrically distorted, resulting in an irregular configuration depending on the clusters, allowing a great variety of configurations [76]. The larger rings permit full relaxation owing to a number of internal degrees of freedom and the strain energy of them will be almost completely relaxed by changing their configuration. This relaxation permits a more flexible network, corresponding to soft confinement, which such related modes are located at lower frequencies [216, 282, 283].

Based on the results, the fs-laser irradiation seems to preserve partially the topology of the silica glass at temperatures above the  $T_g$ , due to the high temperature and ultra-fast thermal quenching. The modifications induce to an increase in the topological heterogeneity and raise the contrast between soft- and strong- domains of the silica glass, either by modifying the intermediate-range order (ring statistics) or by introducing nanopores.

## 5 Summary

The general aim of this work was to investigate the intermediate-range order and the influence of topochemical heterogeneity on the structure of silicate glasses. In contrast, pure topological modifications of silica glass by femtosecond laser exposure were also considered.

Following the results of this work, the average length scale of the intermediate region for aluminosilicate and aluminoborosilicate glasses are in the order of few nanometers, between 3.3 and 4.7 nm. The methods employed to access such regions were accomplished by low-frequency Raman spectroscopy, low-temperature heat capacity followed by CPA to extract the vibrational density of states and THz – TDS. While the low-temperature heat capacity measures the fundamental vibrational modes, the low-frequency Raman spectroscopy and THz - TDS incite molecular vibrations by photons through a selected spectral range, the low-frequency.

Discussing about the limitations of each method, evidently, the low-temperature heat capacity provides a direct access to the VDOS by CPA, whereas both spectroscopic methods have a contribution of the coupling between the photons and atomic vibrations. However, the extraction of VDOS can be mathematically and computationally quite challenging and a qualified person is made necessary. For low-frequency Raman spectroscopy, a choice of an appropriated baseline and normalization is usually particular to each glass system and is not always trivial. Based on the choice, the baseline subtraction can remove some physical contribution, that may lead to wrong results. On the one hand, THz - TDS does not require any pre-treatment, such as baseline subtraction or normalization. On the other hand, systems that comprise infrared active molecules may contribute to the coupling coefficient, which may also compromise the results.

In general, all these methods have been shown as a competent way to access the topological heterogeneity of the glasses systems investigated. This is evident mainly by the Boson peak frequency position, which has been shown a similar trend in aluminosilicate and aluminoborosilicate glasses. Even though the low-temperature heat capacity is physically more accurate and is the only one that can provide a trustable average length scale, sometimes this facility is not appropriated, for example,

in the case of the modified regions of silica glass by femtosecond laser.

Furthermore, to have a complete overview of the intermediate-range order and topological heterogeneity, all glassy systems have been deeply investigated through conventional characterization methods, such as mechanical properties, vibrational spectroscopy and physical characterization. The aluminoborosilicate glass system has been particularly investigated in a deeper approach due to its complex glass structure. Methods such as activation energy of ionic conductivity, photoluminescence spectroscopy and optical basicity have been also considered. Even though the latter involves simple calculations, valuable information about the polarization conducted to the hypothesis of a possible ionic conductivity in this glass system that, even being very small, shed some light to the boron preferences in the vicinity of aluminum sites. Moreover, it is a simple way to depict how a little amount of  $\text{Al}_2\text{O}_3$  may increase the optical basicity of the system in order to improve the compatibility between  $\text{SiO}_2$ - and  $\text{B}_2\text{O}_3$ -networks.

Investigating systematically the addition of alumina in the pure silica network has shown that the topological heterogeneity decreases on a molecular scale by decreasing the average correlation length. Nevertheless, the mechanical properties (bulk modulus and elastic modulus) have shown an increasing trend in function of alumina content, which indicate a tendency of increasing stiffness and decreasing degrees of freedom. Interestingly, the UV-Vis spectroscopy shows an additional information about the glass structure. In the ultra-violet region, addition of few amount of alumina (up to 3.2 mol %  $\text{Al}_2\text{O}_3$ ) shows a decrease of the Rayleigh scattering related to silica glass, most probable by decreasing the average size of heterogeneity. On the other hand, this relation is not linear, instead, the Rayleigh scattering increases considerably for the glass containing 7 mol %  $\text{Al}_2\text{O}_3$ . Considering the Eq. (4.3), this indicates a characteristic – the stresses surrounding such heterogeneity regions may increase considerably. This is a significant information because it is desirable to optical fibers, i.e., controlling the Rayleigh scattering by engineering the structure. This is a kind of information that could not be understood if the heterogeneity of the glass was not considered. Moreover, the stresses also indicate an increase of the non-linear coefficients, which is desirable for short pulse fiber amplifiers, for example.

Addition of  $\text{B}_2\text{O}_3$  in aluminosilicate system emphasizes the importance of investi-



gating the topochemical heterogeneity of glasses. It is worth noting that all most common types of structural characterization of glasses, such as vibrational spectroscopy and absorption spectroscopy, physical properties and mechanical properties (except of strain-rate sensitivity), point to a linear behavior regarding the addition of  $B_2O_3$ . This could, in principle, mislead the interpretation to a homogeneous distribution of boron atoms in the glassy network. However, deeper investigations on vibrational density of states and activation energy of ionic conductivity reveal a different story. In the literature, two systems concerning aluminum borate glasses (sodium aluminum borate and yttrium aluminum borate glasses) have shown by NMR spectroscopy that aluminum will be bonded to as many  $[BO_3]$  units as possible. This information together with the evidences shown by Boson peak frequency, FTIR spectroscopy and activation energy of ionic conductivity lead to a non-linear scenario regarding the topochemical heterogeneity of aluminoborosilicate glasses (see Figure 4.15). The average size of the heterogeneity reaches its maximum for the sample containing 4.3 mol %  $B_2O_3$  and its minimum for the sample containing 6.85 mol %  $B_2O_3$ . This implies that the heterogeneity increases for samples up to 4.3 mol %  $B_2O_3$  and then decreases for samples with higher concentration than 6.85 mol % of  $B_2O_3$ . This is reasonable considering that the size of the correlation length strongly increases as soon as boron has saturated almost all available Al-sites at around 4.3 mol %, and above this concentration, boron has to start to disrupt the silica network to form a more open structure. The FTIR spectroscopy confirms the presence of B-O-B bonds indicated by a band at around  $700\text{ cm}^{-1}$ , only present at concentrations higher than 6.85 mol %  $B_2O_3$ . Interestingly, the sample containing 4.3 mol %  $B_2O_3$  has shown the lowest activation energy and one of the lowest conductivities. At this concentration, the activation energy is low due to the boron in the second shell of aluminum site, forming a “barrier” to the silica network, which is expected to facilitate the mobility. At the same time, the conductivity is also low due to decrease of the polarizability of the oxide ion. Information about preferences and connections of boron atoms inside aluminosilicate glasses are meaningful because i) it leads to a more broadened understanding of the glass and geo-chemistry nature and ii) it allows designing materials according to the topochemical heterogeneity.

Investigations of pure topological modifications after femtosecond laser exposure

have shown that the topology heterogeneity increases by increasing the average correlation length. Modifications at short-range order are mainly composed of broken Si-O bonds and diminishing intertetrahedral bond angle, whereas at intermediate-range order, a different statistical distribution of the rings and presence of nanopores is considered. The fictive temperature and mass density were estimated by Raman spectroscopy by means of the main band and  $D2$  band, respectively. The fictive temperature of the structured lines is higher than the  $T_g$  ( $\sim 1390$  K) and increases according to the pulse energy. For the highest pulse energy,  $11 \mu\text{J}$ , a  $T_f$  of  $\sim 1850$  K was estimated. The mass density of the structured lines also increases around 3%. Compared to densification derived from high-pressure methods (no temperature applied), fs-laser irradiation induces a compression equivalent to few tens of GPa. However, birefringence microscopy indicates that only few hundred MPa is induced. This discrepancy is related to differences in the topology, that is disclosed by the shape of the Boson peak. A compressed sample of the same order of pressure (100 MPa) has been used to compare the topology. While for compressed silica glass the intensity tends to decrease and the Boson peak frequency shifts toward higher frequencies, for the structured lines the intensity also tends to decrease, however, the Boson peak frequency shifts towards lower frequencies. This shape is only seen for the normal liquid state of vitreous silica and indicates that the fs-laser irradiation might preserve the topology of the silica glass above the  $T_g$ . Since the average length scale of heterogeneity for the structured lines is slightly larger and the sound velocity is lower than pristine, this indicates that the contrast between soft- and strong domains raises.

In conclusion, this study has revealed the importance of investigating the topology of the glass at the intermediate-range order and the topochemical heterogeneity of binary and ternary silicate glasses. Moreover, basic characteristics of fundamental relations between network formers and network intermediate have been explained as the result of investigation on intermediate-range order. This study is valid not only for materials applied to optical fibers but also to a more extended view of geo-science and glass chemistry. However, it is important to emphasize that the glass functionality is intrinsically related to the topology and intermediate-range order. Due to the difficulties on understanding the glass topology, a lot of empirical data has been derived from trial-and-error work made in the past. Even though it brought all the

knowledge of materials for optical applications that we have nowadays, the high costs (both in economic and environmental terms) regarding the precursor materials, fused quartz preforms, technological processes and high temperature required to prepare such glasses makes trial-and-error unenforceable. On the other hand, the understanding of the glass topology needs to be in its totality (short- and intermediate-range order), in order to achieve specific applications. This would allow a next level of designing glasses, from bottom-up.

Finally, as a continuity of this work, I would suggest the same kind of investigations employed in this study but concomitantly, in bulk and fiber, to validate if a correlation between intermediate-range order and topochemical heterogeneity is preserved. Furthermore, if a relation between optical losses, topochemical heterogeneity and intermediate-range order could be defined.

## 6 Zusammenfassung

Das generelle Ziel dieser Arbeit war die Untersuchung der mittelreichweitigen Ordnung und der Einfluss topochemischer Heterogenität auf die Struktur von Quarzgläsern.

Im Gegensatz dazu wurden außerdem rein topologische Veränderungen des Quarzglas durch Femtosekunden-Laser-Strahlung berücksichtigt. Gemäß den in dieser Arbeit gefunden Ergebnissen liegt der Bereich der mittelreichweitigen Ordnung für Aluminosilikat- und Aluminoborosilikat-Gläser in der Größenordnung von einigen Nanometern, d.h. zwischen 3.3 und 4.7 nm. Zur Untersuchung dieses Bereichs wurden Niederfrequenz-Ramanspektroskopie und Niedertemperatur-Wärmekapazitätsmessungen verwendet. Weiterhin wurde CPA zur Ermittlung der Dichte der Schwingungszustände (VDOS) und THz-Zeitbereichsspektroskopie verwendet. Während die Niedertemperatur-Wärmekapazität ein Maß für die fundamentalen Schwingungsmoden ist, so regt die Niederfrequenz-Ramanspektroskopie und THz-Zeitbereichsspektroskopie molekulare Schwingungen mittels Photonen in einem ausgewählten, niederfrequenten Spektralbereich an.

Diskutiert man die Grenzen jede dieser Methoden, so liefert die Niedertemperatur-Wärmekapazitätsmessung mittels CPA einen direkten Zugang zur VDOS, wohingegen beide spektroskopische Methoden einen Beitrag aus der Kopplung zwischen Photonen und atomaren Schwingungen besitzen. Dennoch kann die Datengewinnung der VDOS mathematisch und rechentechnisch ziemlich aufwändig sein und einer qualifizierten Person bedürfen. Bei der Niederfrequenz-Ramanspektroskopie ist die Wahl einer geeigneten Grundlinie und Normierung nicht immer trivial und speziell angepasst auf das jeweilige Glassystem. Ausgehend von der Wahl der Grundlinie kann deren Subtraktion einige physikalische Beiträge entfernen und zu verfälschten Ergebnissen führen. Einerseits bedarf THz-Zeitbereichsspektroskopie keiner Datenbearbeitung, wie zum Beispiel Grundlinien-Subtraktion oder Normierung. Andererseits können Systeme welche Infrarot-aktive Moleküle beinhalten zum Koppelkoeffizienten beitragen, was die Ergebnisse ebenfalls verfälschen kann.

Im Allgemeinen haben sich all diese Methoden als ein gutes Mittel für den Zugang zur topologischen Heterogenität von den hier untersuchten Glassystemen herausgestellt. Dies ist im Wesentlichen ersichtlich durch die Frequenz des Boson-Peaks,

welche einen ähnlichen Trend in Aluminosilikat- und Aluminoborosilikat-Gläasern aufzeigte. Auch wenn die Niedertemperatur-Wärmekapazität physikalisch genauer bestimmt werden kann und als einzige Methode einen verlässlichen mittleren Korrelationslänge liefert, so ist sie nicht immer anwendbar, zum Beispiel im Fall der durch einen Femtosekunden-Laser modifizierten Bereiche in Quarzglas.

Weiterhin wurden alle Glassysteme mittels konventioneller Charakterisierungsmethoden tiefgehend untersucht (mechanische Eigenschaften, Schwingungsspektroskopie und physikalische Eigenschaften) um einen kompletten Überblick der mittelreichweiten Ordnung und topologischen Heterogenität zu erhalten. Im Speziellen wurde das Aluminoborosilikat-Glassystem aufgrund seiner komplexen Glasstruktur tiefgehend untersucht. Methoden wie Aktivierungsenergie der Ionenleitfähigkeit, Photolumineszenz-Spektroskopie und optische Basizität wurden auch berücksichtigt. Obwohl Letztere einfache Berechnungen beinhaltet, konnten wertvolle Informationen über Polarisierung abgeleitet und eine Hypothese über eine mögliche Ionenleitung in diesem Glassystem erstellt werden. Wenngleich diese sehr gering ist, so konnte sie doch einige Aufschlüsse über die Bevorzugung von Bor in der Umgebung von Aluminium geben. Darüber hinaus ist es eine einfache Methode um zu beschreiben wie eine kleine Menge  $\text{Al}_2\text{O}_3$  die optische Basizität des Systems erhöhen und die Kompatibilität zwischen  $\text{SiO}_2$ - und  $\text{B}_2\text{O}_3$ -Netzwerken verbessern kann.

Eine systematische Untersuchung der Zugabe von  $\text{Al}_2\text{O}_3$  in das reine Quarzglas-Netzwerk zeigte, dass die topologische Heterogenität auf molekularer Ebene zunimmt, da die durchschnittliche Korrelationslänge abnimmt. Trotzdem zeigten die mechanischen Eigenschaften (Kompressionsmodul und Elastizitätsmodul) einen zunehmenden Trend mit dem  $\text{Al}_2\text{O}_3$ -Gehalt und deutet auf eine zunehmende Steifigkeit und abnehmende Freiheitsgrade hin. Interessanterweise zeigte die UV-Vis-Spektroskopie eine zusätzliche Information hinsichtlich der Glasstruktur. Im ultravioletten Spektralbereich zeigte eine geringe Zugabe von  $\text{Al}_2\text{O}_3$  (bis zu 3.2 mol %) eine Abnahme der Rayleigh-Streuung im Quarzglas, was höchstwahrscheinlich an der Verkleinerung der durchschnittlichen Heterogenität begründet ist. Andererseits ist dieser Zusammenhang nicht linear und die Rayleigh-Streuung nimmt mit  $\text{Al}_2\text{O}_3$ -Gehalt bis 7 mol % merklich zu. Ausgehend von Gleichung 4.3 deutet dies auf eine Eigenschaft hin – die Spannungen, welche solche heterogene Zonen umgeben, können merklich zunehmen.

Dies ist eine bemerkenswerte Information, da diese Eigenschaft wünschenswert für optische Fasern ist, d.h. Beeinflussung der Rayleigh-Streuung durch gezielte Modifikation der Glasstruktur. Es ist eine Art Information welche nicht verstanden werden könnte, wenn die Heterogenität des Glases nicht berücksichtigt werden würde. Weiterhin deuten die Spannung auf eine Zunahme der nicht-linearen Koeffizienten hin, was beispielsweise wünschenswert für Kurzpuls-Faserverstärker ist.

Eine Zugabe von  $B_2O_3$  in Aluminosilikat-Systeme unterschreitet die Wichtigkeit der Untersuchung der topochemischen Heterogenität von Gläsern. Es ist bemerkenswert, dass alle üblichen Verfahren zur strukturellen Charakterisierung von Gläsern, wie Schwingungsspektroskopie und Absorptionsspektroskopie, physikalische Eigenschaften, mechanische Eigenschaften (außer Strain-Rate-Sensitivity), auf ein lineares Verhalten hinsichtlich der Zugabe von  $B_2O_3$  deuten. Dies könnte prinzipiell zu der Fehlinterpretation führen, dass die Bor-Atome homogen im Glas-Netzwerk verteilt sind. Jedoch zeigen tiefere Untersuchungen der VDOS und Aktivierungsenergien der Ionenleitfähigkeit ein anderes Bild.

In der Literatur wurde bereits anhand von NMR-Spektroskopie gezeigt, dass in zwei Aluminoboratglassystemen (Natrium- und Yttriumalumonoboratgläser) Aluminiumionen an so viele  $[BO_3]$ -Einheiten wie möglich anbindet. Zusammen mit den Ergebnissen der Bosonpeak-Frequenzmessung, der FTIR-spektroskopie und der Aktivierungsenergie der ionischen Leitfähigkeit zeigen diese Informationen, dass die topochemische Heterogenität der Alumoborosilikatgläser nichtlineares Verhalten aufweisen (siehe Abbildung 4.15). Die durchschnittliche Größe der Heterogenität erreicht ihr Maximum in der Probe mit 4.30 mol %  $B_2O_3$  und ihr Minimum in der Probe mit 6.85 mol %  $B_2O_3$ . Dies deutet auf einen Anstieg der Heterogenität für Proben mit bis zu 4.30 mol %  $B_2O_3$ , und einen Anstieg der Homogenität für Proben mit einer Konzentration über 6.85 mol %  $B_2O_3$  hin. Dies ist verständlich wenn man bedenkt, dass die Korrelationslänge stark zunimmt sobald Bor bei 4.3 mol % alle verfügbaren Aluminiumplätze besetzt hat. Oberhalb dieser Konzentration muss Bor beginnen das Quarzglasnetzwerk zu zerreißen um eine offenere Struktur zu schaffen. Die FTIR-Spektroskopie bestätigt das Vorhandensein von B-O-B-Bindungen, welche durch ein Band um  $700\text{ cm}^{-1}$  angedeutet werden und nur für Konzentration oberhalb von 6.85 mol %  $B_2O_3$  vorhanden sind. Interessanterweise zeigte die Probe mit 4.3 mol %  $B_2O_3$  die geringste Ak-

tivierungsenergie und eine der geringsten Leitfähigkeiten. Bei dieser Konzentration ist die Aktivierungsenergie aufgrund der Bor-Atome in der zweiten Schale des Aluminium-Atoms, welche eine „Barriere“ zum das Quarzglas-Netzwerk bilden, die Bewegung erleichtert. Gleichzeitig ist die Leitfähigkeit gering aufgrund der Verringerung der Polarisierbarkeit der Sauerstoff-Ionen. Informationen über die Bevorzugung und Bindungen der Bor-Atome in Aluminosilikat-Gläsern sind von großer Bedeutung, da sie i) zu einem verbesserten Verständnis des Glases und dessen geo-chemischer Natur führen und es ii) erlaubt Materialien hinsichtlich ihrer topochemischen Heterogenität zu designen.

Untersuchungen der topologischen Modifikationen nach Femtosekunden-Laser-Belichtung haben gezeigt, dass die topologische Heterogenität durch Vergrößerung der mittleren Korrelationslänge zunimmt. Modifikationen in der Nahordnung bestehen hauptsächlich aus aufgebrochenen Si-O-Bindungen und verringern die Bindungswinkel innerhalb des Tetraeders, wohingegen in der mittelreichweitigen Ordnung eine andere statistische Verteilung der Ringe und das Vorhandensein von Nanoporen berücksichtigt wird. Die fiktive Temperatur und Massendichte wurden durch Raman-Spektroskopie mit Hilfe des Haupt- und  $D_2$ -Bandes abgeschätzt. Die fiktive Temperatur der strukturierten Linien ist höher als  $T_g$  ( $\sim 1390$  K) und wird nimmt mit der Pulsenergie zu. Für die höchste Pulsenergie von  $11 \mu\text{J}$  wurde  $T_f$  mit  $\sim 1850$  K abgeschätzt. Die Massendichte der strukturierten Linien nimmt auch um 3% zu. Im Vergleich zur Verdichtung welche aus den Hochdruck-Methoden abgeleitet wurde (keine Temperatur angewendet), induziert die Femtosekunden-Laserstrahlung eine Kompression, welche äquivalent zu einigen 10 GPa ist. Dennoch deuten die Ergebnisse aus der Polarisationsmikroskopie auf nur einige hundert MPa hin. Diese Diskrepanz beruht auf den Unterschieden in der Topologie, welche durch die Form des Boson-Peaks offenbart wird. Eine komprimierte Probe derselben Größenordnung des Drucks (100 MPa) wurde zum Vergleich der Topologie herangezogen. Während die Intensität in komprimiertem Quarzglas abnimmt und sich die Boson-Peak-Frequenz zu höheren Werten verschiebt, so nimmt die Intensität in den strukturierten Linien ebenfalls ab, jedoch verschiebt sich die Boson-Peak-Frequenz hin zu kleineren Werten. Diese Form kann nur für den normalen flüssigen Zustand von Quarzglas beobachtet werden und deutet darauf hin, dass die Femtosekunden-Laserstrahlung die Topologie des Quarzglases oberhalb des

Unterkühlungsbereiches erhalten könnte. Da die mittlere Korrelationslänge der Heterogenität der strukturierten Linien geringfügig größer und die Schallgeschwindigkeit niedriger als im ursprünglichen Zustand ist, deutet dies darauf hin, dass der Kontrast zwischen weichen und festen Bereichen zunimmt.

Zusammenfassend zeigt diese Studie die Bedeutung der Untersuchung der Topologie von Glasstrukturen im Bereich der mittelreichweitigen Ordnung und der topochemischen Heterogenität von binären und ternären Silicatgläsern. Weiterhin konnten grundlegende Zusammenhänge zwischen Glasformern und Zwischenoxiden ohne Netzwerk-wandler als Ergebnis der Untersuchung der mittleren Ordnung erklärt werden. Diese Studie ist daher nicht nur für Materialien mit Anwendung im Bereich optischer Fasern, sondern auch für einen erweiterten Blickwinkel auf Geowissenschaften und Glaschemie von Bedeutung. Allerdings ist es wichtig zu betonen, dass die Glasfunktionalität intrinsisch von dessen Topologie und mittelreichweitiger Ordnung abhängt.

Abschließend möchte ich, als Fortsetzung dieser Arbeit, eine vergleichbare Untersuchung an Festkörpern und optischen Fasern vorschlagen, um die Erhaltung der Korrelation zwischen mittelreichweitiger Ordnung und der topochemischer Heterogenität zu validieren. Weiterhin könnte ein Zusammenhang zwischen optischen Verlusten und topochemischer Heterogenität und mittelreichweitiger Ordnung definiert werden.



## 7 Bibliography

### References

- [1] W. Shakespeare, “Chapter 1 - The World of Inorganic Glasses,” in *Structural Chemistry of Glasses* (K. J. Rao, ed.), pp. 1–12, Oxford: Elsevier Science Ltd, 2002.
- [2] H. Bach and N. Neuroth, *The Properties of Optical Glass*. Springer-Verlag, 1995.
- [3] P. Hartmann, R. Jedamzik, S. Reichel, and B. Schreder, “Optical glass and glass ceramic historical aspects and recent developments: a Schott view,” *Applied Optics*, vol. 49, no. 16, pp. D157–D176, 2010.
- [4] K. Schuster, S. Unger, C. Aichele, F. Lindner, S. Grimm, D. Litzkendorf, J. Kobelke, J. Bierlich, K. Wondraczek, and H. Bartelt, “Material and technology trends in fiber optics,” *Advanced optical technologies*, vol. 3, no. 4, 2014.
- [5] J. Ballato and P. Dragic, “Materials Development for Next Generation Optical Fiber,” *Materials*, vol. 7, no. 6, pp. 4411–4430, 2014.
- [6] B. Brecht, D. V. Reddy, C. Silberhorn, and M. G. Raymer, “Photon Temporal Modes: A Complete Framework for Quantum Information Science,” *Physical Review X*, vol. 5, no. 4, p. 41017, 2015.
- [7] J. W. Goodman, *International Trends in Optics*. Elsevier Science, 2012.
- [8] Y. Shen, N. C. Harris, S. Skirlo, M. Prabhu, T. Baehr-Jones, M. Hochberg, X. Sun, S. Zhao, H. Larochelle, D. Englund, and M. Soljačić, “Deep learning with coherent nanophotonic circuits,” *Nature Photonics*, vol. 11, p. 441, 2017.
- [9] T. Miya, Y. Terunuma, T. Hosaka, and T. Miyashita, “Ultimate low-loss single-mode fibre at 1.55  $\mu\text{m}$ ,” *Electronics Letters*, vol. 15, no. 4, pp. 106–108, 1979.
- [10] P. Russell, “Photonic Crystal Fibers,” *Science*, vol. 299, no. 5605, p. 358, 2003.

- [11] J. C. Knight, “Photonic crystal fibres,” *Nature*, vol. 424, no. 6950, pp. 847–851, 2003.
- [12] J. Ballato and P. Dragic, “Rethinking Optical Fiber: New Demands, Old Glasses,” *Journal of the American Ceramic Society*, vol. 96, no. 9, pp. 2675–2692, 2013.
- [13] F. P. Kapron, D. B. Keck, and R. D. Maurer, “Radiation Losses in Glass Optical Waveguides,” *Applied Physics Letters*, vol. 17, no. 10, pp. 423–425, 1970.
- [14] W. G. French, J. B. MacChesney, P. B. O’Connor, and G. W. Tasker, “Optical Waveguides With Very Low Losses,” *Bell System Technical Journal*, vol. 53, no. 5, pp. 951–954, 1974.
- [15] J. C. Mauro, C. S. Philip, D. J. Vaughn, and M. S. Pambianchi, “Glass Science in the United States: Current Status and Future Directions,” *International Journal of Applied Glass Science*, vol. 5, no. 1, pp. 2–15, 2014.
- [16] B. Champagnon, L. Wondraczek, and T. Deschamps, “Boson peak, structural inhomogeneity, light scattering and transparency of silicate glasses,” *Journal of Non-Crystalline Solids*, vol. 355, no. 10, pp. 712–714, 2009.
- [17] C. A. Angell, “Formation of Glasses from Liquids and Biopolymers,” *Science*, vol. 267, no. 5206, pp. 1924–1935, 1995.
- [18] J. C. Dyre, “Colloquium: The glass transition and elastic models of glass-forming liquids,” *Reviews of Modern Physics*, vol. 78, no. 3, pp. 953–972, 2006.
- [19] E. J. Donth, *The Glass Transition: Relaxation Dynamics in Liquids and Disordered Materials*. Springer, 2001.
- [20] E. D. Zanotto and J. C. Mauro, “The glassy state of matter: Its definition and ultimate fate,” *Journal of Non-Crystalline Solids*, vol. 471, pp. 490–495, 2017.
- [21] L. M. C. Janssen, “Mode-Coupling Theory of the Glass Transition: A Primer,” *Frontiers in Physics*, vol. 6, no. 97, 2018.
- [22] N. Toyota, M. Lang, and J. Müller, *Low-Dimensional Molecular Metals*. Springer Berlin Heidelberg, 2007.

- [23] C. A. Angell, “Perspective on the glass transition,” *Journal of Physics and Chemistry of Solids*, vol. 49, no. 8, pp. 863–871, 1988.
- [24] J. C. Maxwell and W. D. Niven, *The Scientific Papers of James Clerk Maxwell, Vol. II*. Dover Publications, 2003.
- [25] T. V. Tropin, J. W. Schmelzer, and V. L. Aksenov, “Modern aspects of the kinetic theory of glass transition,” *Physics-Uspekhi*, vol. 59, no. 1, pp. 42–66, 2016.
- [26] P. G. Debenedetti, *Metastable Liquids: Concepts and Principles*. Princeton University Press, 1996.
- [27] W. Shakespeare, “Chapter 3 - The Glass Transition Phenomenon,” in *Structural Chemistry of Glasses* (K. J. Rao, ed.), pp. 77–135, Oxford: Elsevier Science Ltd, 2002.
- [28] C. Donati, J. F. Douglas, W. Kob, S. J. Plimpton, P. H. Poole, and S. C. Glotzer, “Stringlike Cooperative Motion in a Supercooled Liquid,” *Physical Review Letters*, vol. 80, no. 11, pp. 2338–2341, 1998.
- [29] R. H. Colby, “Dynamic scaling approach to glass formation,” *Physical Review E*, vol. 61, no. 2, pp. 1783–1792, 2000.
- [30] U. Bengtzelius, W. Gotze, and A. Sjolander, “Dynamics of supercooled liquids and the glass transition,” *Journal of Physics C: Solid State Physics*, vol. 17, no. 33, pp. 5915–5934, 1984.
- [31] W. Götze, *Complex Dynamics of Glass-Forming Liquids: A Mode-Coupling Theory*. Oxford University Press, 2009.
- [32] S. Karmakar, C. Dasgupta, and S. Sastry, “Length scales in glass-forming liquids and related systems: a review,” *Reports on Progress in Physics*, vol. 79, no. 1, p. 16601, 2015.
- [33] A. Widmer-Cooper, H. Perry, P. Harrowell, and D. R. Reichman, “Irreversible reorganization in a supercooled liquid originates from localized soft modes,” *Nature Physics*, vol. 4, p. 711, 2008.

- [34] H. Hinrichsen and D. E. Wolf, *The Physics of Granular Media*. Wiley, 2006.
- [35] F. H. Stillinger, “A Topographic View of Supercooled Liquids and Glass Formation,” *Science*, vol. 267, no. 5206, pp. 1935–1939, 1995.
- [36] T. B. Schroder, S. Sastry, J. C. Dyre, and S. C. Glotzer, “Crossover to potential energy landscape dominated dynamics in a model glass-forming liquid,” *The Journal of Chemical Physics*, vol. 112, no. 22, pp. 9834–9840, 2000.
- [37] M. Goldstein, “Viscous Liquids and the Glass Transition: A Potential Energy Barrier Picture,” *The Journal of Chemical Physics*, vol. 51, no. 9, pp. 3728–3739, 1969.
- [38] F. H. Stillinger and T. A. Weber, “Packing Structures and Transitions in Liquids and Solids,” *Science*, vol. 225, no. 4666, pp. 983–989, 1984.
- [39] G. Ruocco, F. Sette, R. Di Leonardo, G. Monaco, M. Sampoli, T. Scopigno, and G. Viliani, “Relaxation Processes in Harmonic Glasses?,” *Physical Review Letters*, vol. 84, no. 25, pp. 5788–5791, 2000.
- [40] A. Das and B. K. Chakrabarti, *Quantum Annealing and Related Optimization Methods*. Springer Berlin Heidelberg, 2005.
- [41] D. J. Wales, “A Microscopic Basis for the Global Appearance of Energy Landscapes,” *Science*, vol. 293, no. 5537, pp. 2067–2070, 2001.
- [42] D. J. Wales, “Decoding the energy landscape: extracting structure, dynamics and thermodynamics,” *Philosophical Transactions of the Royal Society A: Mathematical, Physical and Engineering Sciences*, vol. 370, no. 1969, pp. 2877–2899, 2012.
- [43] P. G. Debenedetti, F. H. Stillinger, T. M. Truskett, and C. J. Roberts, “The Equation of State of an Energy Landscape,” *The Journal of Physical Chemistry B*, vol. 103, no. 35, pp. 7390–7397, 1999.
- [44] G. P. Srivastava, *The Physics of Phonons*. Taylor & Francis, 1990.
- [45] L. Mihály and M. C. Martin, *Solid State Physics: Problems and Solutions*. Wiley, 2009.

- [46] E. Kaxiras, *Atomic and Electronic Structure of Solids*. Cambridge University Press, 2003.
- [47] L. Lou, *Introduction to Phonons and Electrons*. World Scientific, 2003.
- [48] M. T. Dove, M. T. Dove, C. U. Press, M. F. Hochella, R. C. Liebermann, and A. Putnis, *Introduction to Lattice Dynamics*. Cambridge University Press, 1993.
- [49] J. Simmons, K. S. P. Joseph Simmons, K. S. Potter, E. I. Inc, and ProQuest, *Optical Materials*. Elsevier Science, 2000.
- [50] L. Pauling, *General Chemistry*. Dover Publications, 2014.
- [51] M. de Podesta, *Understanding the Properties of Matter*. Taylor & Francis, 2002.
- [52] B. Ruta, *Les propriétés vibrationnelles des verres : un étude expérimental dans la region de transition entre le régime microscopique et macroscopique*. PhD thesis, Universite de Grenoble, 2010.
- [53] B. Huang, H. Y. Bai, and W. H. Wang, “Relationship between boson heat capacity peaks and evolution of heterogeneous structure in metallic glasses,” *Journal of Applied Physics*, vol. 115, no. 15, p. 153505, 2014.
- [54] A. Navrotsky, R. C. Liebermann, and A. Putnis, *Physics and Chemistry of Earth Materials*. Cambridge University Press, 1994.
- [55] R. C. Zeller and R. O. Pohl, “Thermal Conductivity and Specific Heat of Non-crystalline Solids,” *Physical Review B*, vol. 4, no. 6, pp. 2029–2041, 1971.
- [56] G. J. Grabovskij, *Investigation of coherent microscopic defects inside the tunneling barrier of a Josephson junction*. KIT Scientific Publishing, 2014.
- [57] V. L. Gurevich, D. A. Parshin, and H. R. Schober, “Pressure dependence of the boson peak in glasses,” *Physical Review B*, vol. 71, no. 1, p. 14209, 2005.
- [58] M. Baggioli and A. Zaccone, “Universal Origin of Boson Peak Vibrational Anomalies in Ordered Crystals and in Amorphous Materials,” *Physical Review Letters*, vol. 122, no. 14, p. 145501, 2019.

- [59] L. Zhang, J. Zheng, Y. Wang, L. Zhang, Z. Jin, L. Hong, Y. Wang, and J. Zhang, “Experimental studies of vibrational modes in a two-dimensional amorphous solid,” *Nature Communications*, vol. 8, no. 1, p. 67, 2017.
- [60] R. Vacher, B. Rufflé, B. Hehlen, G. Guimbrètiere, G. Simon, and E. Courtens, “The vibrational excitations of glasses in the boson-peak region: application to borates,” *Physics and Chemistry of Glasses - European Journal of Glass Science and Technology Part B*, vol. 49, no. 1, pp. 19–25, 2008.
- [61] M. A. Ramos, “Are the calorimetric and elastic Debye temperatures of glasses really different?,” *Philosophical Magazine*, vol. 84, no. 13-16, pp. 1313–1321, 2004.
- [62] U. Buchenau, M. Prager, N. Nücker, A. J. Dianoux, N. Ahmad, and W. A. Phillips, “Low-frequency modes in vitreous silica,” *Physical Review B*, vol. 34, no. 8, pp. 5665–5673, 1986.
- [63] M. F. Thorpe and L. Tichý, *Properties and applications of amorphous materials*, vol. 9. Springer Science & Business Media, 2012.
- [64] S. Corezzi, S. Caponi, F. Rossi, and D. Fioretto, “Stress-Induced Modification of the Boson Peak Scaling Behavior,” *The Journal of Physical Chemistry B*, vol. 117, no. 46, pp. 14477–14485, 2013.
- [65] S. Caponi, S. Corezzi, D. Fioretto, A. Fontana, G. Monaco, and F. Rossi, “Raman-Scattering Measurements of the Vibrational Density of States of a Reactive Mixture During Polymerization: Effect on the Boson Peak,” *Physical Review Letters*, vol. 102, no. 2, p. 27402, 2009.
- [66] A. Marruzzo, W. Schirmacher, A. Fratallocchi, and G. Ruocco, “Heterogeneous shear elasticity of glasses: the origin of the boson peak,” *Scientific Reports*, vol. 3, p. 1407, 2013.
- [67] W. Vogel, *Glass chemistry*. Springer Science & Business Media, 2012.
- [68] D. Hülsenberg, A. Harnisch, and A. Bismarck, *Microstructuring of glasses*, vol. 87. Springer, 2008.

- [69] L. Pauling, *The Nature of the Chemical Bond*, vol. 260. Cornell University Press Ithaca, 1960.
- [70] B. Silvi and P. D'Arco, *Modelling of Minerals and Silicated Materials*. Springer Netherlands, 2006.
- [71] K. Binder and W. Kob, *Glassy Materials and Disordered Solids: An Introduction to Their Statistical Mechanics*. World Scientific, 2011.
- [72] W. Bragg, "Chapter 2 - The Glassy State," in *Structural Chemistry of Glasses* (K. J. Rao, ed.), pp. 13–76, Oxford: Elsevier Science Ltd, 2002.
- [73] D. L. Price, "Intermediate-range order in glasses," *Current Opinion in Solid State and Materials Science*, vol. 1, no. 4, pp. 572–577, 1996.
- [74] R. J. Bell and P. Dean, "Properties of Vitreous Silica: Analysis of Random Network Models," *Nature*, vol. 212, no. 5068, pp. 1354–1356, 1966.
- [75] F. L. Galeener, "Planar rings in vitreous silica," *Journal of Non-Crystalline Solids*, vol. 49, no. 1, pp. 53–62, 1982.
- [76] T. Uchino, Y. Kitagawa, and T. Yoko, "Structure, energies, and vibrational properties of silica rings in SiO<sub>2</sub> glass," *Physical Review B*, vol. 61, no. 1, pp. 234–240, 2000.
- [77] A. Kubota, M. J. Caturla, J. S. Stölken, and M. D. Feit, "Densification of fused silica due to shock waves and its implications for 351 nm laser induced damage," *Optics Express*, vol. 8, no. 11, pp. 611–616, 2001.
- [78] J. E. Shelby and R. S. of Chemistry, *Introduction to Glass Science and Technology*. Royal Society of Chemistry, 2005.
- [79] N. Tsuneyoshi, "Boson peak and terahertz frequency dynamics of vitreous silica," *Reports on Progress in Physics*, vol. 65, no. 8, p. 1195, 2002.
- [80] M. J. Lakin and H. Scholze, *Glass: Nature, Structure, and Properties*. Springer New York, 2012.

- [81] J. Zarzycki, W. D. Scott, and C. Massart, *Glasses and the Vitreous State*. Cambridge University Press, 1991.
- [82] B. Golding and P. A. Fleury, *Coherence and Energy Transfer in Glasses*. Springer US, 2013.
- [83] F. L. Galeener, R. A. Barrio, E. Martinez, and R. J. Elliott, “Vibrational Decoupling of Rings in Amorphous Solids,” *Physical Review Letters*, vol. 53, no. 25, pp. 2429–2432, 1984.
- [84] L. Giacomazzi, P. Umari, and A. Pasquarello, “Medium-range structure of vitreous SiO<sub>2</sub> obtained through first-principles investigation of vibrational spectra,” *Physical Review B*, vol. 79, no. 6, p. 64202, 2009.
- [85] N. M. Trease, T. M. Clark, P. J. Grandinetti, J. F. Stebbins, and S. Sen, “Bond length-bond angle correlation in densified silica—Results from <sup>17</sup>O NMR spectroscopy,” *The Journal of Chemical Physics*, vol. 146, no. 18, p. 184505, 2017.
- [86] R. Dronskowski, S. Kikkawa, and A. Stein, *Handbook of Solid State Chemistry, 6 Volume Set*. Wiley, 2017.
- [87] S. R. Elliott, “Amorphous Materials: Medium-range Order,” in *Encyclopedia of Materials: Science and Technology* (K. H. J. Buschow, R. W. Cahn, M. C. Flemings, B. Ilshner, E. J. Kramer, S. Mahajan, and P. Veysière, eds.), pp. 215–219, Oxford: Elsevier, 2001.
- [88] M. Eigen, “Chapter 12 - Oxide Glasses,” in *Structural Chemistry of Glasses* (K. J. Rao, ed.), pp. 463–511, Oxford: Elsevier Science Ltd, 2002.
- [89] C. Massobrio, J. Du, M. Bernasconi, and P. S. Salmon, *Molecular Dynamics Simulations of Disordered Materials: From Network Glasses to Phase-Change Memory Alloys*. Springer International Publishing, 2015.
- [90] R. A. Barrio, F. L. Castillo-Alvarado, and F. L. Galeener, “Structural and vibrational model for vitreous boron oxide,” *Physical Review B*, vol. 44, no. 14, pp. 7313–7320, 1991.



- [91] F. Angeli, O. Villain, S. Schuller, T. Charpentier, D. de Ligny, L. Bressel, and L. Wondraczek, "Effect of temperature and thermal history on borosilicate glass structure," *Physical Review B*, vol. 85, no. 5, p. 54110, 2012.
- [92] S. K. Lee, C. B. Musgrave, P. Zhao, and J. F. Stebbins, "Topological Disorder and Reactivity of Borosilicate Glasses: Quantum Chemical Calculations and  $^{17}\text{O}$  and  $^{11}\text{B}$  NMR Study," *The Journal of Physical Chemistry B*, vol. 105, no. 50, pp. 12583–12595, 2001.
- [93] J. A. Duffy, "The importance of pi-bonding in glass chemistry: borate glasses," *Physics and Chemistry of Glasses - European Journal of Glass Science and Technology Part B*, vol. 49, no. 6, pp. 317–325, 2008.
- [94] M. Okuno, N. Zotov, M. Schmücker, and H. Schneider, "Structure of  $\text{SiO}_2\text{-Al}_2\text{O}_3$  glasses: Combined X-ray diffraction, IR and Raman studies," *Journal of Non-Crystalline Solids*, vol. 351, no. 12–13, pp. 1032–1038, 2005.
- [95] S. K. Lee and J. F. Stebbins, "The degree of aluminum avoidance in aluminosilicate glasses," *American Mineralogist*, vol. 84, no. 5-6, pp. 937–945, 1999.
- [96] S. K. Lee and J. F. Stebbins, "The Structure of Aluminosilicate Glasses: High-Resolution  $^{17}\text{O}$  and  $^{27}\text{Al}$  MAS and  $^3\text{QMAS}$  NMR Study," *The Journal of Physical Chemistry B*, vol. 104, no. 17, pp. 4091–4100, 2000.
- [97] J. Lægsgaard, "Dissolution of rare-earth clusters in  $\text{SiO}_2$  by Al codoping: A microscopic model," *Physical Review B (Condensed Matter and Materials Physics)*, vol. 65, no. 17, p. 174114, 2002.
- [98] P. Pfeleiderer, J. Horbach, and K. Binder, "Structure and transport properties of amorphous aluminium silicates: Computer simulation studies," *Chemical Geology*, vol. 229, no. 1–3, pp. 186–197, 2006.
- [99] M. Schmücker and H. Schneider, "New evidence for tetrahedral triclusters in aluminosilicate glasses," *Journal of Non-Crystalline Solids*, vol. 311, no. 2, pp. 211–215, 2002.

- [100] J. F. Stebbins, J. V. Oglesby, and S. Kroeker, "Oxygen triclusters in crystalline  $\text{CaAl}_4\text{O}_7$  (grossite) and in calcium aluminosilicate glasses:  $^{17}\text{O}$  NMR," *American Mineralogist*, vol. 86, no. 10, pp. 1307–1311, 2001.
- [101] A. Winkler, J. Horbach, W. Kob, and K. Binder, "Structure and diffusion in amorphous aluminum silicate: A molecular dynamics computer simulation," *The Journal of Chemical Physics*, vol. 120, no. 1, pp. 384–393, 2004.
- [102] M. Benoit, M. Profeta, F. Mauri, C. J. Pickard, and M. E. Tuckerman, "First-Principles Calculation of the  $^{17}\text{O}$  NMR Parameters of a Calcium Aluminosilicate Glass," *The Journal of Physical Chemistry B*, vol. 109, no. 13, pp. 6052–6060, 2005.
- [103] M. Schmücker, K. J. D. MacKenzie, H. Schneider, and R. Meinhold, "NMR studies on rapidly solidified  $\text{SiO}_2\text{-Al}_2\text{O}_3$  and  $\text{SiO}_2\text{-Al}_2\text{O}_3\text{-Na}_2\text{O}$ -glasses," *Journal of Non-Crystalline Solids*, vol. 217, no. 1, pp. 99–105, 1997.
- [104] J. F. Macdowell and G. H. Beall, "Immiscibility and Crystallization in  $\text{Al}_2\text{O}_3\text{-SiO}_2$  Glasses," *Journal of the American Ceramic Society*, vol. 52, no. 1, pp. 17–25, 1969.
- [105] W. Loewenstein, "The Distribution of Aluminum in the Tetrahedra of Silicates and Aluminates," *American Mineralogist*, vol. 39, p. 92, 1954.
- [106] M. A. Wilson and S. A. McCarthy, "Long range effects of the aluminum avoidance principle," *Analytical Chemistry*, vol. 57, no. 13, pp. 2733–2735, 1985.
- [107] J. A. Tossell and J. Horbach, "O Triclusters Revisited: Classical MD and Quantum Cluster Results for Glasses of Composition  $(\text{Al}_2\text{O}_3)_2(\text{SiO}_2)$ ," *The Journal of Physical Chemistry B*, vol. 109, no. 5, pp. 1794–1797, 2005.
- [108] S. H. Wemple, D. A. Pinnow, T. C. Rich, R. E. Jaeger, and L. G. V. Uitert, "Binary  $\text{SiO}_2\text{-B}_2\text{O}_3$  glass system: Refractive index behavior and energy gap considerations," *Journal of Applied Physics*, vol. 44, no. 12, pp. 5432–5437, 1973.

- [109] L. G. Van Uitert, D. A. Pinnow, J. C. Williams, T. C. Rich, R. E. Jaeger, and W. H. Grodkiewicz, “Borosilicate glasses for fiber optical waveguides,” *Materials Research Bulletin*, vol. 8, no. 4, pp. 469–476, 1973.
- [110] A. S. Tenney and J. Wong, “Vibrational Spectra of Vapor-Deposited Binary Borosilicate Glasses,” *The Journal of Chemical Physics*, vol. 56, no. 11, pp. 5516–5523, 1972.
- [111] S. Wang and J. F. Stebbins, “Multiple-Quantum Magic-Angle Spinning 17O NMR Studies of Borate, Borosilicate, and Boroaluminate Glasses,” *Journal of the American Ceramic Society*, vol. 82, no. 6, pp. 1519–1528, 1999.
- [112] R. Martens and W. Müller-Warmuth, “Structural groups and their mixing in borosilicate glasses of various compositions – an NMR study,” *Journal of Non-Crystalline Solids*, vol. 265, no. 1, pp. 167–175, 2000.
- [113] A. Soleilhavoup, J.-M. Delaye, F. Angeli, D. Caurant, and T. Charpentier, “Contribution of first-principles calculations to multinuclear NMR analysis of borosilicate glasses,” *Magnetic Resonance in Chemistry*, vol. 48, no. S1, pp. S159–S170, 2010.
- [114] H. Doweidar, “Consideration of the boron oxide anomaly,” *Journal of Materials Science*, vol. 25, no. 1, pp. 253–258, 1990.
- [115] M. M. Smedskjaer, R. E. Youngman, and J. C. Mauro, “Principles of Pyrex® glass chemistry: structure–property relationships,” *Applied Physics A*, vol. 116, no. 2, pp. 491–504, 2014.
- [116] G. Kaur, *Bioactive Glasses: Potential Biomaterials for Future Therapy*. Springer International Publishing, 2017.
- [117] K. Schuster, S. Grimm, A. Kalide, J. Dellith, M. Leich, A. Schwuchow, A. Langner, G. Schötz, and H. Bartelt, “Evolution of fluorine doping following the REPUSIL process for the adjustment of optical properties of silica materials,” *Optical Materials Express*, vol. 5, no. 4, pp. 887–897, 2015.
- [118] A. Langner, G. Schötz, M. Such, T. Kayser, V. Reichel, S. Grimm, J. Kirchhof, V. Krause, and G. Rehmann, “A new material for high-power laser fibers,”

- in *Lasers and Applications in Science and Engineering*, vol. 6873, pp. 687311–687319, 2008.
- [119] T. H. K. Barron and G. K. White, *Heat Capacity and Thermal Expansion at Low Temperatures*. Springer US, 2012.
- [120] N. V. Surovtsev, “Evaluation of terahertz density of vibrational states from specific-heat data: Application to silica glass,” *Physical Review E*, vol. 64, no. 6, p. 61102, 2001.
- [121] S. Köhler, G. Ruocco, and W. Schirmacher, “Coherent potential approximation for diffusion and wave propagation in topologically disordered systems,” *Physical Review B*, vol. 88, no. 6, p. 64203, 2013.
- [122] W. Schirmacher, G. Diezemann, and C. Ganter, “Harmonic Vibrational Excitations in Disordered Solids and the “Boson Peak”,” *Physical Review Letters*, vol. 81, no. 1, pp. 136–139, 1998.
- [123] W. Schirmacher, T. Scopigno, and G. Ruocco, “Theory of vibrational anomalies in glasses,” *Journal of Non-Crystalline Solids*, vol. 407, pp. 133–140, 2015.
- [124] W. Schirmacher, T. Scopigno, and G. Ruocco, “Theory of vibrational anomalies in glasses,” *Journal of Non-Crystalline Solids*, vol. 407, pp. 133–140, 2015.
- [125] P. Larkin, *Infrared and Raman Spectroscopy: Principles and Spectral Interpretation*. Elsevier Science, 2011.
- [126] C. James, “Chapter 4 - Structural Techniques,” in *Structural Chemistry of Glasses* (K. J. Rao, ed.), pp. 137–183, Oxford: Elsevier Science Ltd, 2002.
- [127] R. Shuker and R. W. Gammon, “Raman-Scattering Selection-Rule Breaking and the Density of States in Amorphous Materials,” *Physical Review Letters*, vol. 25, no. 4, pp. 222–225, 1970.
- [128] F. L. Galeener and A. E. Geissberger, “Vibrational dynamics in 30Si-substituted vitreous SiO<sub>2</sub>,” *Physical Review B*, vol. 27, no. 10, pp. 6199–6204, 1983.
- [129] E. P. J. Parrott, J. A. Zeitler, T. Friščić, M. Pepper, W. Jones, G. M. Day, and L. F. Gladden, “Testing the Sensitivity of Terahertz Spectroscopy to Changes

- in Molecular and Supramolecular Structure: A Study of Structurally Similar Cocrystals,” *Crystal Growth & Design*, vol. 9, no. 3, pp. 1452–1460, 2009.
- [130] M. E. Fermann, A. Galvanauskas, and G. Sucha, *Ultrafast Lasers: Technology and Applications*. Taylor & Francis, 2002.
- [131] E. P. J. Parrott, J. A. Zeitler, G. Simon, B. Hehlen, L. F. Gladden, S. N. Taraskin, and S. R. Elliott, “Atomic charge distribution in sodosilicate glasses from terahertz time-domain spectroscopy,” *Physical Review B*, vol. 82, no. 14, p. 140203, 2010.
- [132] S. N. Taraskin, S. I. Simdyankin, S. R. Elliott, J. R. Neilson, and T. Lo, “Universal Features of Terahertz Absorption in Disordered Materials,” *Physical Review Letters*, vol. 97, no. 5, p. 55504, 2006.
- [133] D. Campbell, R. A. Pethrick, and J. R. White, *Polymer Characterization: Physical Techniques, 2nd Edition*. CRC Press, 2017.
- [134] G. P. Holmes-Hampton, W.-H. Tong, and T. A. Rouault, “Chapter 15 - Biochemical and Biophysical Methods for Studying Mitochondrial Iron Metabolism,” in *Methods in Enzymology* (A. N. Murphy and D. C. Chan, eds.), vol. 547, pp. 275–307, Academic Press, 2014.
- [135] M. Anpo and M. Che, “Applications of Photoluminescence Techniques to the Characterization of Solid Surfaces in Relation to Adsorption, Catalysis, and Photocatalysis,” in *Advances in Catalysis* (W. O. Haag, B. C. Gates, and H. Knözinger, eds.), vol. 44, pp. 119–257, Academic Press, 1999.
- [136] I. D. Aggarwal and G. Lu, *Fluoride Glass Fiber Optics*. Elsevier Science, 2013.
- [137] W. Lu and Y. Fu, *Spectroscopy of Semiconductors: Numerical Analysis Bridging Quantum Mechanics and Experiments*. Springer International Publishing, 2018.
- [138] K. C. Honeychurch, “13 - Printed thick-film biosensors,” in *Printed Films* (M. Prudenziati and J. Hormadaly, eds.), pp. 366–409, Woodhead Publishing, 2012.

- [139] C. B. Bragatto, *Abordagem termodinâmica do transporte iônico e da relaxação estrutural em vidros fosfatos de prata*. PhD thesis, Universidade Federal de São Carlos, 2016.
- [140] L. K. Sudha, R. Sukumar, and K. Uma Rao, “Evaluation of activation energy ( $E_a$ ) profiles of nanostructured alumina polycarbonate composite insulation materials,” *International Journal of Materials, Mechanics and Manufacturing*, vol. 2, no. 1, pp. 96–100, 2014.
- [141] L. Föppl and E. Mönch, *Grundlagen*. Berlin, Heidelberg: Springer Berlin Heidelberg, 1972.
- [142] Heraeus, “Quartz Glass for Optics Data and Properties.”
- [143] R. Kashyap, *Fiber Bragg Gratings*. Elsevier Science, 2009.
- [144] W. R. Calhoun, H. Maeta, A. Combs, L. M. Bali, and S. Bali, “Measurement of the refractive index of highly turbid media,” *Optics Letters*, vol. 35, no. 8, pp. 1224–1226, 2010.
- [145] M. J. Damzen, V. Vlad, A. Mocofanescu, and V. Babin, *Stimulated Brillouin Scattering: Fundamentals and Applications*. CRC Press, 2003.
- [146] S. Caponi, P. Benassi, R. Eramo, A. Giugni, M. Nardone, A. Fontana, M. Sampoli, F. Terki, and T. Woignier, “Phonon attenuation in vitreous silica and silica porous systems,” *Philosophical Magazine*, vol. 84, no. 13-16, pp. 1423–1431, 2004.
- [147] P. Sellappan, T. Rouxel, F. Celarie, E. Becker, P. Houizot, and R. Conradt, “Composition dependence of indentation deformation and indentation cracking in glass,” *Acta Materialia*, vol. 61, no. 16, pp. 5949–5965, 2013.
- [148] G. N. B. M. de Macedo, S. Sawamura, and L. Wondraczek, “Lateral hardness and the scratch resistance of glasses in the  $\text{Na}_2\text{O-CaO-SiO}_2$  system,” *Journal of Non-Crystalline Solids*, vol. 492, pp. 94–101, 2018.
- [149] M. F. Ando, O. Benzine, Z. Pan, J.-L. Garden, K. Wondraczek, S. Grimm, K. Schuster, and L. Wondraczek, “Boson peak, heterogeneity and intermediate-

- range order in binary SiO<sub>2</sub>-Al<sub>2</sub>O<sub>3</sub> glasses,” *Scientific Reports*, vol. 8, no. 1, p. 5394, 2018.
- [150] P. Dragic, M. Cavillon, and J. Ballato, “The linear and nonlinear refractive index of amorphous Al<sub>2</sub>O<sub>3</sub> deduced from aluminosilicate optical fibers,” *International Journal of Applied Glass Science*, vol. 9, no. 3, pp. 421–427, 2018.
- [151] P. Dragic, J. Ballato, A. Ballato, S. Morris, T. Hawkins, P. C. Law, S. Ghosh, and M. C. Paul, “Mass density and the Brillouin spectroscopy of aluminosilicate optical fibers,” *Optical Materials Express*, vol. 2, no. 11, pp. 1641–1654, 2012.
- [152] P. D. Dragic, J. Ballato, S. Morris, and T. Hawkins, “Pockels’ coefficients of alumina in aluminosilicate optical fiber,” *Journal of the Optical Society of America B*, vol. 30, no. 2, pp. 244–250, 2013.
- [153] N. Zotov, I. Ebbsjö, D. Timpel, and H. Keppler, “Calculation of Raman spectra and vibrational properties of silicate glasses: Comparison between Na<sub>2</sub>Si<sub>4</sub>O<sub>9</sub> and SiO<sub>2</sub> glasses,” *Physical Review B*, vol. 60, no. 9, pp. 6383–6397, 1999.
- [154] P. McMillan, “Structural studies of silicate glasses and melts; applications and limitations of Raman spectroscopy?,” *American Mineralogist*, vol. 69, no. 7-8, pp. 622–644, 1984.
- [155] A. Winterstein-Beckmann, D. Möncke, D. Palles, E. I. Kamitsos, and L. Wondraczek, “A Raman-spectroscopic study of indentation-induced structural changes in technical alkali-borosilicate glasses with varying silicate network connectivity,” *Journal of Non-Crystalline Solids*, vol. 405, no. Supplement C, pp. 196–206, 2014.
- [156] S. K. Sharma, D. W. Matson, J. A. Philpotts, and T. L. Roush, “Raman study of the structure of glasses along the join SiO<sub>2</sub>-GeO<sub>2</sub>,” *Journal of Non-Crystalline Solids*, vol. 68, no. 1, pp. 99–114, 1984.
- [157] C. T. Kirk, “Quantitative analysis of the effect of disorder-induced mode coupling on infrared absorption in silica,” *Physical Review B*, vol. 38, no. 2, pp. 1255–1273, 1988.

- [158] I. Šimon and H. O. McMahon, “Study of the Structure of Quartz, Cristobalite, and Vitreous Silica by Reflection in Infrared,” *The Journal of Chemical Physics*, vol. 21, no. 1, pp. 23–30, 1953.
- [159] S. Sen, “Atomic environment of high-field strength Nd and Al cations as dopants and major components in silicate glasses: a Nd LIII-edge and Al K-edge X-ray absorption spectroscopic study,” *Journal of Non-Crystalline Solids*, vol. 261, no. 1, pp. 226–236, 2000.
- [160] S. Sen and R. E. Youngman, “High-Resolution Multinuclear NMR Structural Study of Binary Aluminosilicate and Other Related Glasses,” *The Journal of Physical Chemistry B*, vol. 108, no. 23, pp. 7557–7564, 2004.
- [161] T. Hanada, Y. Bessyo, and N. Soga, “Elastic constants of amorphous thin films in the systems SiO<sub>2</sub>-Al<sub>2</sub>O<sub>3</sub> and AlPO<sub>4</sub>-Al<sub>2</sub>O<sub>3</sub>,” *Journal of Non-Crystalline Solids*, vol. 113, no. 2, pp. 213–220, 1989.
- [162] E. D. Lacy, “Aluminum in glasses and melts,” *Phys. Chem. Glasses*, vol. 4, no. 6, pp. 234–238, 1963.
- [163] J. Lægsgaard, “Theory of Al<sub>2</sub>O<sub>3</sub> incorporation in SiO<sub>2</sub>,” *Physical Review B*, vol. 65, no. 17, p. 174104, 2002.
- [164] B. Hehlen and G. Simon, “The vibrations of vitreous silica observed in hyper-Raman scattering,” *Journal of Raman Spectroscopy*, vol. 43, no. 12, pp. 1941–1950, 2012.
- [165] Y. Inamura, M. Arai, T. Otomo, N. Kitamura, and U. Buchenau, “Density dependence of the boson peak of vitreous silica,” *Physica B: Condensed Matter*, vol. 284-288, no. Part 2, pp. 1157–1158, 2000.
- [166] B. Mantisi, S. Adichtchev, S. Sirotkin, L. Rafaelly, L. Wondraczek, H. Behrens, C. Marcenat, N. V. Surovtsev, A. Pillonnet, E. Duval, B. Champagnon, and A. Mermet, “Non-Debye normalization of the glass vibrational density of states in mildly densified silicate glasses,” *Journal of Physics: Condensed Matter*, vol. 22, no. 2, p. 25402, 2010.



- [167] P. Chen, C. Holbrook, P. Boolchand, D. G. Georgiev, K. A. Jackson, and M. Micoulaut, “Intermediate phase, network demixing, boson and floppy modes, and compositional trends in glass transition temperatures of binary  $\text{As}(x)\text{S}(1-x)$  system,” *Physical Review B*, vol. 78, no. 22, p. 224208, 2008.
- [168] B. T. Poe, P. F. McMillan, C. A. Angell, and R. K. Sato, “Al and Si coordination in  $\text{SiO}_2\text{-Al}_2\text{O}_3$  glasses and liquids: A study by NMR and IR spectroscopy and MD simulations,” *Chemical Geology*, vol. 96, no. 3, pp. 333–349, 1992.
- [169] S. R. Elliott, “A Unified Model for the Low-Energy Vibrational Behaviour of Amorphous Solids,” *EPL (Europhysics Letters)*, vol. 19, no. 3, p. 201, 1992.
- [170] E. Duval, A. Boukenter, and T. Achibat, “Vibrational dynamics and the structure of glasses,” *Journal of Physics: Condensed Matter*, vol. 2, no. 51, p. 10227, 1990.
- [171] E. Duval, A. Mermet, and L. Saviot, “Boson peak and hybridization of acoustic modes with vibrations of nanometric heterogeneities in glasses,” *Physical Review B*, vol. 75, no. 2, p. 24201, 2007.
- [172] L. Hong, V. N. Novikov, and A. P. Sokolov, “Dynamic heterogeneities, boson peak, and activation volume in glass-forming liquids,” *Physical Review E*, vol. 83, no. 6, p. 61508, 2011.
- [173] G. Carini, G. Carini, D. Cosio, G. D’Angelo, and F. Rossi, “Low temperature heat capacity of permanently densified  $\text{SiO}_2$  glasses,” *Philosophical Magazine*, vol. 96, no. 7-9, pp. 761–773, 2016.
- [174] W. Schirmacher, G. Ruocco, and T. Scopigno, “Acoustic Attenuation in Glasses and its Relation with the Boson Peak,” *Physical Review Letters*, vol. 98, no. 2, p. 25501, 2007.
- [175] A. J. Cox, A. J. DeWeerd, and J. Linden, “An experiment to measure Mie and Rayleigh total scattering cross sections,” *American Journal of Physics*, vol. 70, no. 6, pp. 620–625, 2002.
- [176] M. Potuzak and M. M. Smedskjaer, “Physical properties of boroaluminosilicate glasses: effect of modifier cation field strength,” *Physics and Chemistry*

- of Glasses - European Journal of Glass Science and Technology Part B*, vol. 55, no. 1, pp. 18–24, 2014.
- [177] L.-S. Du and J. F. Stebbins, “Network connectivity in aluminoborosilicate glasses: A high-resolution  $^{11}\text{B}$ ,  $^{27}\text{Al}$  and  $^{17}\text{O}$  NMR study,” *Journal of Non-Crystalline Solids*, vol. 351, no. 43, pp. 3508–3520, 2005.
- [178] J. Wu and J. F. Stebbins, “Quench rate and temperature effects on boron coordination in aluminoborosilicate melts,” *Journal of Non-Crystalline Solids*, vol. 356, no. 41, pp. 2097–2108, 2010.
- [179] J. Wu, M. Potuzak, and J. F. Stebbins, “High-temperature in situ  $^{11}\text{B}$  NMR study of network dynamics in boron-containing glass-forming liquids,” *Journal of Non-Crystalline Solids*, vol. 357, no. 24, pp. 3944–3951, 2011.
- [180] J. F. Stebbins, J. Wu, and L. M. Thompson, “Interactions between network cation coordination and non-bridging oxygen abundance in oxide glasses and melts: Insights from NMR spectroscopy,” *Chemical Geology*, vol. 346, pp. 34–46, 2013.
- [181] W.-F. Du, K. Kuraoka, T. Akai, and T. Yazawa, “Study of  $\text{Al}_2\text{O}_3$  effect on structural change and phase separation in  $\text{Na}_2\text{O}-\text{B}_2\text{O}_3-\text{SiO}_2$  glass by NMR,” *Journal of Materials Science*, vol. 35, no. 19, pp. 4865–4871, 2000.
- [182] L.-S. Du and J. F. Stebbins, “Site connectivities in sodium aluminoborate glasses: multinuclear and multiple quantum NMR results,” *Solid State Nuclear Magnetic Resonance*, vol. 27, no. 1, pp. 37–49, 2005.
- [183] Q. Zheng, M. Potuzak, J. C. Mauro, M. M. Smedskjaer, R. E. Youngman, and Y. Yue, “Composition–structure–property relationships in boroaluminosilicate glasses,” *Journal of Non-Crystalline Solids*, vol. 358, no. 6, pp. 993–1002, 2012.
- [184] J. Wu and J. F. Stebbins, “Effects of cation field strength on the structure of aluminoborosilicate glasses: High-resolution  $^{11}\text{B}$ ,  $^{27}\text{Al}$  and  $^{23}\text{Na}$  MAS NMR,” *Journal of Non-Crystalline Solids*, vol. 355, no. 9, pp. 556–562, 2009.

- [185] M. Engholm and L. Norin, “Preventing photodarkening in ytterbium-doped high power fiber lasers; correlation to the UV-transparency of the core glass,” *Optics Express*, vol. 16, no. 2, pp. 1260–1268, 2008.
- [186] J. Wang, “Alumina as a dopant in optical fiber by OVD,” *Applied Physics A*, vol. 116, no. 2, pp. 505–518, 2014.
- [187] S. Rydberg and M. Engholm, “Experimental evidence for the formation of divalent ytterbium in the photodarkening process of Yb-doped fiber lasers,” *Optics Express*, vol. 21, no. 6, pp. 6681–6688, 2013.
- [188] S. Unger, J. Dellith, A. Scheffel, and J. Kirchhof, “Diffusion in Yb<sub>2</sub>O<sub>3</sub>–Al<sub>2</sub>O<sub>3</sub>–SiO<sub>2</sub> glass,” *Physics and Chemistry of Glasses-European Journal of Glass Science and Technology Part B*, vol. 52, no. 2, pp. 41–46, 2011.
- [189] T. Arai, K. Ichii, K. Okada, T. Kitabayashi, S. Tanigawa, and M. Fujimaki, “Photodarkening phenomenon in Yb-doped fibers,” *Fujikura Giho*, pp. 6–11, 2008.
- [190] K. C. Mills, “The Influence of Structure on the Physico-chemical Properties of Slags,” *ISIJ International*, vol. 33, no. 1, pp. 148–155, 1993.
- [191] B. Glorieux, T. Salminen, J. Massera, M. Lastusaari, and L. Petit, “Better understanding of the role of SiO<sub>2</sub>, P<sub>2</sub>O<sub>5</sub> and Al<sub>2</sub>O<sub>3</sub> on the spectroscopic properties of Yb<sup>3+</sup> doped silica sol-gel glasses,” *Journal of Non-Crystalline Solids*, vol. 482, pp. 46–51, 2018.
- [192] H. Doweidar, “The density of sodium borosilicate glasses in relation to the microstructure,” *Journal of Physics and Chemistry of Solids*, vol. 53, no. 6, pp. 807–814, 1992.
- [193] I. Kashif, E. M. Sakr, A. A. Soliman, and A. Ratep, “Influence of SiO<sub>2</sub> substitution for B<sub>2</sub>O<sub>3</sub> on the properties of borosilicate glasses,” *Physics and Chemistry of Glasses - European Journal of Glass Science and Technology Part B*, vol. 54, no. 1, pp. 35–41, 2013.
- [194] J. A. Duffy, “A review of optical basicity and its applications to oxidic systems,” *Geochimica et Cosmochimica Acta*, vol. 57, no. 16, pp. 3961–3970, 1993.

- [195] X. Zhao, X. Wang, H. Lin, and Z. Wang, “Electronic polarizability and optical basicity of lanthanide oxides,” *Physica B: Condensed Matter*, vol. 392, no. 1–2, pp. 132–136, 2007.
- [196] Y. B. Saddeek, K. A. Aly, and S. A. Bashier, “Optical study of lead borosilicate glasses,” *Physica B: Condensed Matter*, vol. 405, no. 10, pp. 2407–2412, 2010.
- [197] M. K. Halimah, M. F. Faznny, M. N. Azlan, and H. A. A. Sidek, “Optical basicity and electronic polarizability of zinc borotellurite glass doped  $\text{La}^{3+}$  ions,” *Results in Physics*, vol. 7, pp. 581–589, 2017.
- [198] V. Dimitrov and T. Komatsu, “Classification of oxide glasses: A polarizability approach,” *Journal of Solid State Chemistry*, vol. 178, no. 3, pp. 831–846, 2005.
- [199] V. Dimitrov and T. Komatsu, “Interionic Interactions, Electronic Polarizability and Optical Basicity of Oxide Glasses,” *Journal of the Ceramic Society of Japan*, vol. 108, no. 1256, pp. 330–338, 2000.
- [200] V. Dimitrov and T. Komatsu, “Classification of Simple Oxides: A Polarizability Approach,” *Journal of Solid State Chemistry*, vol. 163, no. 1, pp. 100–112, 2002.
- [201] I. Kashif, A. Ratep, and G. Adel, “Polarizability, optical basicity and optical properties of  $\text{SiO}_2\text{-B}_2\text{O}_3\text{-Bi}_2\text{O}_3\text{-TeO}_2$  glass system,” *Applied Physics A*, vol. 124, no. 7, p. 486, 2018.
- [202] J. Yamashita and T. Kurosawa, “The Theory of the Dielectric Constant of Ionic Crystals III,” *Journal of the Physical Society of Japan*, vol. 10, no. 8, pp. 610–633, 1955.
- [203] G. V. Gibbs, “Molecules as models for bonding in silicates,” *American Mineralogist*, vol. 67, no. 5-6, pp. 421–450, 1982.
- [204] N. Ollier, G. Concas, G. Panczer, B. Champagnon, and T. Charpentier, “Structural features of a  $\text{Eu}^{3+}$  doped nuclear glass and gels obtained from glass leaching,” *Journal of Non-Crystalline Solids*, vol. 328, no. 1, pp. 207–214, 2003.

- [205] N. Shibata, M. Horigudhi, and T. Edahiro, "Raman spectra of binary high-silica glasses and fibers containing GeO<sub>2</sub>, P<sub>2</sub>O<sub>5</sub> and B<sub>2</sub>O<sub>3</sub>," *Journal of Non-Crystalline Solids*, vol. 45, no. 1, pp. 115–126, 1981.
- [206] D. Möncke, D. Ehrt, and E. I. Kamitsos, "Spectroscopic study of manganese-containing borate and borosilicate glasses: cluster formation and phase separation," *Physics and Chemistry of Glasses - European Journal of Glass Science and Technology Part B*, vol. 54, no. 1, pp. 42–51, 2013.
- [207] K. Shilpa and V. M. Jali, "Structural investigation and optical properties of xMnO<sub>2</sub>-25Li<sub>2</sub>O-5Na<sub>2</sub>O-15Bi<sub>2</sub>O<sub>3</sub>-(55-x)B<sub>2</sub>O<sub>3</sub> glasses," *IOP Conference Series: Materials Science and Engineering*, vol. 310, no. 1, p. 12057, 2018.
- [208] W. Kern and R. Heim, "Chemical Vapor Deposition of Silicate Glasses for Use with Silicon Devices: II . Film Properties," *Journal of The Electrochemical Society*, vol. 117, no. 4, pp. 568–573, 1970.
- [209] M. H. Manghnani, A. Hushur, T. Sekine, J. Wu, J. F. Stebbins, and Q. Williams, "Raman, Brillouin, and nuclear magnetic resonance spectroscopic studies on shocked borosilicate glass," *Journal of Applied Physics*, vol. 109, no. 11, p. 113509, 2011.
- [210] C. McIntosh, J. Toulouse, and P. Tick, "The Boson peak in alkali silicate glasses," *Journal of Non-Crystalline Solids*, vol. 222, no. Supplement C, pp. 335–341, 1997.
- [211] H. Deters, J. F. de Lima, C. J. Magon, A. S. S. de Camargo, and H. Eckert, "Structural models for yttrium aluminium borate laser glasses: NMR and EPR studies of the system (Y<sub>2</sub>O<sub>3</sub>)<sub>0.2</sub> - (Al<sub>2</sub>O<sub>3</sub>)<sub>x</sub> - (B<sub>2</sub>O<sub>3</sub>)<sub>0.8-x</sub>," *Physical Chemistry Chemical Physics*, vol. 13, no. 35, pp. 16071–16083, 2011.
- [212] N. Ollier, R. Planchais, and B. Boizot, "EPR study of Yb-doped irradiated glasses," *Nuclear Instruments and Methods in Physics Research Section B: Beam Interactions with Materials and Atoms*, vol. 266, no. 12, pp. 2854–2858, 2008.

- [213] M. Bertmer, L. Züchner, J. C. C. Chan, and H. Eckert, “Short and Medium Range Order in Sodium Aluminoborate Glasses. 2. Site Connectivities and Cation Distributions Studied by Rotational Echo Double Resonance NMR Spectroscopy,” *The Journal of Physical Chemistry B*, vol. 104, no. 28, pp. 6541–6553, 2000.
- [214] Y. Cheng, H. Xiao, and B. Tang, “Non-isothermal crystallization kinetics of MgO–BaO–B<sub>2</sub>O<sub>3</sub>–Al<sub>2</sub>O<sub>3</sub>–SiO<sub>2</sub> glass,” *Ceramics International*, vol. 35, no. 8, pp. 3503–3506, 2009.
- [215] H. Deters, A. S. S. de Camargo, C. N. Santos, C. R. Ferrari, A. C. Hernandez, A. Ibanez, M. T. Rinke, and H. Eckert, “Structural Characterization of Rare-Earth Doped Yttrium Aluminoborate Laser Glasses Using Solid State NMR,” *The Journal of Physical Chemistry C*, vol. 113, no. 36, pp. 16216–16225, 2009.
- [216] R. Zorn, “Boson peak in confined disordered systems,” *Physical Review B*, vol. 81, no. 5, p. 54208, 2010.
- [217] Y. M. Beltukov, C. Fusco, D. A. Parshin, and A. Tanguy, “Boson peak and Ioffe-Regel criterion in amorphous siliconlike materials: The effect of bond directionality,” *Physical Review E*, vol. 93, no. 2, p. 23006, 2016.
- [218] H. Jain and A. S. Nowick, “Electrical conductivity of synthetic and natural quartz crystals,” *Journal of Applied Physics*, vol. 53, no. 1, pp. 477–484, 1982.
- [219] H. Jain and A. S. Nowick, “Radiation-induced conductivity in quartz crystals,” *Journal of Applied Physics*, vol. 53, no. 1, pp. 485–489, 1982.
- [220] D. Del Frate, S. Quilici, G. Spinolo, and A. Vedda, “High-temperature ac conductivity of amorphous SiO<sub>2</sub>: Fused silica and thin thermal films,” *Physical Review B*, vol. 59, no. 15, pp. 9741–9744, 1999.
- [221] P. Campone, M. Magliocco, G. Spinolo, and A. Vedda, “Ionic transport in crystalline SiO<sub>2</sub>: The role of alkali-metal ions and hydrogen impurities,” *Physical Review B*, vol. 52, no. 22, pp. 15903–15908, 1995.

- [222] J. Kincs and S. W. Martin, “Non-Arrhenius Conductivity in Glass: Mobility and Conductivity Saturation Effects,” *Physical Review Letters*, vol. 76, no. 1, pp. 70–73, 1996.
- [223] O. L. Anderson and D. A. Stuart, “Calculation of Activation Energy of Ionic Conductivity in Silica Glasses by Classical Methods,” *Journal of the American Ceramic Society*, vol. 37, no. 12, pp. 573–580, 1954.
- [224] J. Swenson and L. Börjesson, “Intermediate-range structure and conductivity of fast ion-conducting borate glasses,” *Journal of Non-Crystalline Solids*, vol. 232–234, pp. 658–664, 1998.
- [225] N. J. Dudney, W. C. West, and J. Nanda, *Handbook of solid state batteries*. World Scientific, 2nd ed., 2015.
- [226] A. Pradel and M. Ribes, “Ionic conductive glasses,” *Materials Science and Engineering: B*, vol. 3, no. 1, pp. 45–56, 1989.
- [227] S. W. Martin, “Ionic Conduction in Phosphate Glasses,” *Journal of the American Ceramic Society*, vol. 74, no. 8, pp. 1767–1784, 1991.
- [228] W. Wang, R. Christensen, B. Curtis, S. W. Martin, and J. Kieffer, “A new model linking elastic properties and ionic conductivity of mixed network former glasses,” *Physical Chemistry Chemical Physics*, vol. 20, no. 3, pp. 1629–1641, 2018.
- [229] M. D. Ingram, “Ionic conductivity and glass structure,” *Philosophical Magazine B*, vol. 60, no. 6, pp. 729–740, 1989.
- [230] G. N. Greaves and K. L. Ngai, “Reconciling ionic-transport properties with atomic structure in oxide glasses,” *Physical Review B*, vol. 52, no. 9, pp. 6358–6380, 1995.
- [231] M. Arai, H. Iwase, M. Nakamura, T. Otomo, E. Kartini, K. Itoh, S. J. Levett, and S. M. Bennington, “Relation between High Ionic Conductivity and Boson Peak in Superionic Glass,” *AIP Conference Proceedings*, vol. 832, no. 1, pp. 299–302, 2006.

- [232] E. Kartini, M. Arai, F. Mezei, M. Nakamura, and M. Russina, “Structure and dynamics on superionic conducting phosphate glasses by neutron scattering,” *Physica B: Condensed Matter*, vol. 385-386, pp. 236–239, 2006.
- [233] A. Zoubir, M. Richardson, L. Canioni, A. Brocas, and L. Sarger, “Optical properties of infrared femtosecond laser-modified fused silica and application to waveguide fabrication,” *Journal of the Optical Society of America B*, vol. 22, no. 10, pp. 2138–2143, 2005.
- [234] J. W. Chan, T. R. Huser, S. H. Risbud, and D. M. Krol, “Modification of the fused silica glass network associated with waveguide fabrication using femtosecond laser pulses,” *Applied Physics A*, vol. 76, no. 3, pp. 367–372, 2003.
- [235] M. Okuno, B. Reynard, Y. Shimada, Y. Syono, and C. Willaime, “A Raman spectroscopic study of shock-wave densification of vitreous silica,” *Physics and Chemistry of Minerals*, vol. 26, no. 4, pp. 304–311, 1999.
- [236] A. Zoubir, C. Rivero, R. Grodsky, K. Richardson, M. Richardson, T. Cardinal, and M. Couzi, “Laser-induced defects in fused silica by femtosecond IR irradiation,” *Physical Review B*, vol. 73, no. 22, p. 224117, 2006.
- [237] M. Sakakura, M. Terazima, Y. Shimotsuma, K. Miura, and K. Hirao, “Observation of pressure wave generated by focusing a femtosecond laser pulse inside a glass,” *Optics Express*, vol. 15, no. 9, pp. 5674–5686, 2007.
- [238] S. Sawamura, R. Limbach, H. Behrens, and L. Wondraczek, “Lateral deformation and defect resistance of compacted silica glass: Quantification of the scratching hardness of brittle glasses,” *Journal of Non-Crystalline Solids*, vol. 481, pp. 503–511, 2018.
- [239] D. L. Griscom, “Nature Of Defects And Defect Generation In Optical Glasses,” in *1985 Albuquerque Conferences on Optics*, vol. 0541, p. 22, SPIE, 1985.
- [240] J. Götze, M. Plötze, and D. Habermann, “Origin, spectral characteristics and practical applications of the cathodoluminescence (CL) of quartz – a review,” *Mineralogy and Petrology*, vol. 71, no. 3, pp. 225–250, 2001.



- [241] M. K. Abd-Rahman, S. N. M. Halim, R. M. Nor, N. I. Razaki, M. F. M. Taib, A. b. M. A. Ibrahim, and P. Poopalan, “Effects of intrinsic defects on the electronic and optical properties of amorphous silica: First principle study,” in *2017 2nd International Conference on Automation, Cognitive Science, Optics, Micro Electro-Mechanical System, and Information Technology (ICACOMIT)*, pp. 128–132, 2017.
- [242] H. Nishikawa, T. Shiroyama, R. Nakamura, Y. Ohki, K. Nagasawa, and Y. Hama, “Photoluminescence from defect centers in high-purity silica glasses observed under 7.9-eV excitation,” *Physical Review B*, vol. 45, no. 2, pp. 586–591, 1992.
- [243] W. J. Reichman, D. M. Krol, L. Shah, F. Yoshino, A. Arai, S. M. Eaton, and P. R. Herman, “A spectroscopic comparison of femtosecond-laser-modified fused silica using kilohertz and megahertz laser systems,” *Journal of Applied Physics*, vol. 99, no. 12, p. 123112, 2006.
- [244] S. G. Demos, M. Staggs, K. Minoshima, and J. Fujimoto, “Characterization of laser induced damage sites in optical components,” *Optics Express*, vol. 10, no. 25, pp. 1444–1450, 2002.
- [245] S.-I. Tsutomu, F. Katsunori, N. Setsuo, S. Kazuo, F. Tetsuo, and I. Noriaki, “Visible photoluminescence in Si<sup>+</sup>-implanted silica glass,” *Journal of Applied Physics*, vol. 75, no. 12, pp. 7779–7783, 1994.
- [246] H. Imai and H. Hirashima, “Intrinsic- and extrinsic-defect formation in silica glasses by radiation,” *Journal of Non-Crystalline Solids*, vol. 179, pp. 202–213, 1994.
- [247] J. Zhou and B. Li, “Origins of a damage-induced green photoluminescence band in fused silica revealed by time-resolved photoluminescence spectroscopy,” *Optical Materials Express*, vol. 7, no. 8, pp. 2888–2898, 2017.
- [248] A. B. K. von Haeftena, “In situ passivation and blue luminescence of silicon clusters using a cluster beam/H<sub>2</sub>O codeposition production method,” *Applied Physics Letters*, vol. 94, no. 26, p. 261102, 2009.

- [249] C. Itoh, T. Suzuki, and N. Itoh, “Luminescence and defect formation in undensified and densified amorphous SiO<sub>2</sub>,” *Physical Review B*, vol. 41, no. 6, pp. 3794–3799, 1990.
- [250] M. Guzzi, M. Martini, M. Mattaini, F. Pio, and G. Spinolo, “Luminescence of fused silica: Observation of the O<sub>2</sub>- emission band,” *Physical Review B*, vol. 35, no. 17, pp. 9407–9409, 1987.
- [251] H. Koyama, “Cathodoluminescence study of SiO<sub>2</sub>,” *Journal of Applied Physics*, vol. 51, no. 4, pp. 2228–2235, 1980.
- [252] H. Martens and E. Stark, “Extended multiplicative signal correction and spectral interference subtraction: New preprocessing methods for near infrared spectroscopy,” *Journal of Pharmaceutical and Biomedical Analysis*, vol. 9, no. 8, pp. 625–635, 1991.
- [253] L. Bressel, D. de Ligny, C. Sonnevile, V. Martinez, V. Mizeikis, R. Buividas, and S. Juodkazis, “Femtosecond laser induced density changes in GeO<sub>2</sub> and SiO<sub>2</sub> glasses: fictive temperature effect,” *Optical Materials Express*, vol. 1, no. 4, pp. 605–613, 2011.
- [254] J. W. Chan, T. Huser, S. Risbud, and D. M. Krol, “Structural changes in fused silica after exposure to focused femtosecond laser pulses,” *Optics Letters*, vol. 26, no. 21, pp. 1726–1728, 2001.
- [255] C. Martinet, V. Martinez, C. Coussa, B. Champagnon, and M. Tomozawa, “Radial distribution of the fictive temperature in pure silica optical fibers by micro-Raman spectroscopy,” *Journal of Applied Physics*, vol. 103, no. 8, p. 83506, 2008.
- [256] R. A. Murray and W. Y. Ching, “Electronic- and vibrational-structure calculations in models of the compressed SiO<sub>2</sub> glass system,” *Physical Review B*, vol. 39, no. 2, pp. 1320–1331, 1989.
- [257] P. Jund and R. Jullien, “Densification effects on the Boson peak in vitreous silica: A molecular-dynamics study,” *The Journal of Chemical Physics*, vol. 113, no. 7, pp. 2768–2771, 2000.

- [258] A. Perriot, D. Vandembroucq, E. Barthel, V. Martinez, L. Grosvalet, C. Martinet, and B. Champagnon, “Raman Microspectroscopic Characterization of Amorphous Silica Plastic Behavior,” *Journal of the American Ceramic Society*, vol. 89, no. 2, pp. 596–601, 2006.
- [259] O. Benzine, S. Bruns, Z. Pan, K. Durst, and L. Wondraczek, “Local Deformation of Glasses is Mediated by Rigidity Fluctuation on Nanometer Scale,” *Advanced Science*, vol. 5, no. 10, p. 1800916, 2018.
- [260] A. Marcinkevičius, S. Juodkazis, M. Watanabe, M. Miwa, S. Matsuo, H. Misawa, and J. Nishii, “Femtosecond laser-assisted three-dimensional microfabrication in silica,” *Optics Letters*, vol. 26, no. 5, pp. 277–279, 2001.
- [261] E. N. Glezer and E. Mazur, “Ultrafast-laser driven micro-explosions in transparent materials,” *Applied Physics Letters*, vol. 71, no. 7, pp. 882–884, 1997.
- [262] M. Lancry, B. Poumellec, J. Canning, K. Cook, J.-C. Poulin, and F. Brisset, “Ultrafast nanoporous silica formation driven by femtosecond laser irradiation,” *Laser & Photonics Reviews*, vol. 7, no. 6, pp. 953–962, 2013.
- [263] M. Sakakura, M. Terazima, Y. Shimotsuma, K. Miura, and K. Hirao, “Thermal and shock induced modification inside a silica glass by focused femtosecond laser pulse,” *Journal of Applied Physics*, vol. 109, no. 2, p. 23503, 2011.
- [264] H. Sugiura, R. Ikeda, K. Kondo, and T. Yamadaya, “Densified silica glass after shock compression,” *Journal of Applied Physics*, vol. 81, no. 4, pp. 1651–1655, 1997.
- [265] P. Koziatek, J. L. Barrat, and D. Rodney, “Short- and medium-range orders in as-quenched and deformed SiO<sub>2</sub> glasses: An atomistic study,” *Journal of Non-Crystalline Solids*, vol. 414, pp. 7–15, 2015.
- [266] T. Deschamps, J. Margueritat, C. Martinet, A. Mermet, and B. Champagnon, “Elastic Moduli of Permanently Densified Silica Glasses,” *Scientific Reports*, vol. 4, p. 7193, 2014.

- [267] T. Rouxel, H. Ji, T. Hammouda, and A. Moréac, “Poisson’s Ratio and the Densification of Glass under High Pressure,” *Physical Review Letters*, vol. 100, no. 22, p. 225501, 2008.
- [268] C. B. Schaffer, A. Brodeur, J. F. García, and E. Mazur, “Micromachining bulk glass by use of femtosecond laser pulses with nanojoule energy,” *Optics Letters*, vol. 26, no. 2, pp. 93–95, 2001.
- [269] H. Kakiuchida, K. Saito, and A. J. Ikushima, “Refractive Index, Density and Polarizability of Silica Glass with Various Fictive Temperatures,” *Japanese Journal of Applied Physics*, vol. 43, no. No. 6A, pp. L743–L745, 2004.
- [270] W. H. Wang, “The elastic properties, elastic models and elastic perspectives of metallic glasses,” *Progress in Materials Science*, vol. 57, no. 3, pp. 487–656, 2012.
- [271] D. Fioretto, S. Corezzi, S. Caponi, F. Scarponi, G. Monaco, A. Fontana, and L. Palmieri, “Cauchy relation in relaxing liquids,” *The Journal of Chemical Physics*, vol. 128, no. 21, p. 214502, 2008.
- [272] M. Zanatta, G. Baldi, S. Caponi, A. Fontana, E. Gilioli, M. Krish, C. Masciovecchio, G. Monaco, L. Orsingher, F. Rossi, G. Ruocco, and R. Verbeni, “Elastic properties of permanently densified silica: A Raman, Brillouin light, and x-ray scattering study,” *Physical Review B*, vol. 81, no. 21, p. 212201, 2010.
- [273] S. Richter, A. Plech, M. Steinert, M. Heinrich, S. Döring, F. Zimmermann, U. Peschel, E. Kley, A. Tünnermann, and S. Nolte, “On the fundamental structure of femtosecond laser-induced nanogratings,” *Laser & Photonics Reviews*, vol. 6, no. 6, pp. 787–792, 2012.
- [274] A. J. Martin and W. Brenig, “Model for Brillouin Scattering in Amorphous Solids,” *physica status solidi (b)*, vol. 64, no. 1, pp. 163–172, 1974.
- [275] L. Orsingher, A. Fontana, E. Gilioli, G. C. Jr., G. Carini, G. Tripodo, T. Unruh, and U. Buchenau, “Vibrational dynamics of permanently densified GeO<sub>2</sub> glasses: Densification-induced changes in the boson peak,” *The Journal of Chemical Physics*, vol. 132, no. 12, p. 124508, 2010.

- [276] T. Deschamps, C. Martinet, D. de Ligny, J. L. Bruneel, and B. Champagnon, “Low-frequency Raman scattering under high pressure in diamond anvil cell: Experimental protocol and application to GeO<sub>2</sub> and SiO<sub>2</sub> boson peaks,” *Journal of Non-Crystalline Solids*, vol. 358, no. 23, pp. 3156–3160, 2012.
- [277] A. G. Kalampounias, S. N. Yannopoulos, and G. N. Papatheodorou, “A low-frequency Raman study of glassy, supercooled and molten silica and the preservation of the Boson peak in the equilibrium liquid state,” *Journal of Non-Crystalline Solids*, vol. 352, no. 42, pp. 4619–4624, 2006.
- [278] S. Reibstein, L. Wondraczek, D. de Ligny, S. Krolikowski, S. Sirotkin, J.-P. Simon, V. Martinez, and B. Champagnon, “Structural heterogeneity and pressure-relaxation in compressed borosilicate glasses by in situ small angle X-ray scattering,” *The Journal of Chemical Physics*, vol. 134, no. 20, p. 204502, 2011.
- [279] Q. Zhao, M. Guerette, and L. Huang, “Nanoindentation and Brillouin light scattering studies of elastic moduli of sodium silicate glasses,” *Journal of Non-Crystalline Solids*, vol. 358, no. 3, pp. 652–657, 2012.
- [280] L. Bin, W. Jing-Yang, Z. Yan-Chun, and L. Fang-Zhi, “Temperature Dependence of Elastic Properties for Amorphous SiO<sub>2</sub> by Molecular Dynamics Simulation,” *Chinese Physics Letters*, vol. 25, no. 8, pp. 2747–2750, 2008.
- [281] N. S. Shcheblanov, M. E. Povarnitsyn, K. N. Mishchik, and A. Tanguy, “Raman spectroscopy of femtosecond multipulse irradiation of vitreous silica: Experiment and simulation,” *Physical Review B*, vol. 97, no. 5, p. 54106, 2018.
- [282] H. M. Flores-Ruiz, G. G. Naumis, and J. C. Phillips, “Heating through the glass transition: A rigidity approach to the boson peak,” *Physical Review B*, vol. 82, no. 21, p. 214201, 2010.
- [283] H. M. Flores-Ruiz and G. G. Naumis, “Boson peak as a consequence of rigidity: A perturbation theory approach,” *Physical Review B*, vol. 83, no. 18, p. 184204, 2011.

# Selbstständigkeitserklärung

Ich erkläre, dass ich die vorliegende Arbeit selbstständig und unter Verwendung der angegebenen Hilfsmittel, persönlichen Mitteilungen und Quellen angefertigt habe.

Jena, 02. Dezember 2019

---

Mariana Fatobene Ando

# Curriculum Vitae

## Personal Information:

Name: Mariana Fatobene Ando

Date of Birth: 09.08.1984 in Santo André, São Paulo, Brazil

Nationality: Brazilian

## Professional Experience:

03.2018 – 10.2019 Research associate at Otto Schott Institute for Materials Research, Friedrich-Schiller-Universität, Jena, Germany.

07.2013 – 12.2013 Research and Development Intern at Fotonica - Tecnologia Óptica, Campinas, São Paulo, Brazil.

## Education:

09.2011 - 12.2013 **M. Sc. in Nanoscience and Advanced Materials.** Universidade Federal do ABC (UFABC), Santo André, São Paulo, Brazil in collaboration with Universidade Estadual de Campinas (UNICAMP), Campinas, São Paulo, Brazil.

10.2012 - 01.2014 **B. Sc. in Materials Engineering** (emphasis on ceramic materials). Universidade Federal do ABC (UFABC), Santo André, São Paulo, Brazil.

01.2007 – 09.2012 **B. Sc. in Science and Technology.** Universidade Federal do ABC (UFABC), Santo André, São Paulo, Brazil.

01.2002 – 12.2005 **B. Sc. in Biological Science.** Centro Universitário Fundação Santo André (FSA), Santo André, São Paulo, Brazil.

Jena, 02. Dezember 2019

---

Mariana Fatobene Ando